2015

Complexity in Overmarsh Circulation

Jessica Chassereau Sullivan
University of South Carolina - Columbia

Recommended Citation

Sullivan, J. C.(2015). *Complexity in Overmarsh Circulation.* (Doctoral dissertation). Retrieved from https://scholarcommons.sc.edu/etd/3161

COMPLEXITY IN OVERMARSH CIRCULATION

by

Jessica Chassereau Sullivan

Bachelor of Science
University of South Carolina, 2005

Submitted in Partial Fulfillment of the Requirements

For the Degree of Doctor of Philosophy in

Geological Sciences

College of Arts and Sciences

University of South Carolina

2015

Accepted by:

Raymond Torres, Major Professor

Subrahmanyam Bulusu, Committee Member

Alfred Garrett, Committee Member

Lewis Lapine, Committee Member

Alexander Yankovsky, Committee Member

Lacy Ford, Vice Provost and Dean of Graduate Studies

DEDICATION

To my dearest Hannah, you are my inspiration and the motivation for all that I do. I love you with all of my heart. I hope that you always remember that if you dream it, you can do it. So dream big baby girl!

ACKNOWLEDGEMENTS

This work is funded by DOE grant # DE-AC09-96SR18500.

I open by thanking my Lord and Savior, Jesus Christ, for we go forward in life by His grace alone. I especially want to thank my loving husband, Robert Sullivan Jr. This journey set us both on a long and winding path of change, challenge, and at times, adversity. Thank you for always offering your unconditional love and support, but especially for your patience when this work required my full attention. From the very beginning you were convinced that I had the potential to earn this degree. I am only now seeing things in myself that you saw all along. I will always love you for that. I am very lucky to have such a wonderful husband and father for our daughter. You are my best friend and I couldn't ask for a better companion to share this journey with, and many more to come.

A very special thank you goes to my parents, James and Margaret Chassereau. Thank you for raising me to always believe that I could accomplish anything. This work would not have been possible without your love and encouragement. Daddy, thank you for teaching me all that I know, especially the value of hard work and staying the course. Your love, guidance and wisdom made me the person that I am today. I will forever be thankful for that. Your advice over the years had a profound impact on my attitude during this journey, and I hope that one day I can do the same for my children. Also, thanks for helping me set up the day of my defense. You helped make the day a big success! Momma, thank you for your encouragement and for helping me to find the humor in life,

even during the dark times. The times that we laughed together were the cure for despair and doubt on many occasions. You always showed a genuine interest in my work. I enjoyed our discussions and your questions always inspired me to dig deeper. But I especially thank you for going above and beyond to help with my baby girl, Hannah during my long work hours! It was always nice to come home to your delicious home-cooking! To my sister, Erin Chassereau, I am so grateful for your unconditional love and support, and especially for being an invaluable link to my past. The times that we laughed and reminisced about the good times were often the ultimate stress relief when I needed it the most! You also offered a great deal of encouragement over the years, and you never doubted me. Thank you for always being there. I also owe a great deal of my success to the precious children in my life. To my daughter, Hannah, and my nieces, Lauren and Bailey, thank you for reminding me of the importance of childlike curiosity and the power of an open mind. I hope that you keep both for all of your lives, and that they lead you down fruitful paths of discovery and happiness. Lauren, you could always tell when I was down and overwhelmed, even without me saying so. You always found a way to lift my spirits! To my in-laws, Linda, Robert and Jason Sullivan, I am deeply moved by your generosity. We owe much of what we have to you. Thank you for always giving so selflessly to help us over the years, and also for offering kind words of encouragement along the way.

To my advisor, Raymond Torres, thank you for setting me on this project and for the opportunity to earn this degree. When we met six years ago you saw potential in me that I could not see. At many times during my work at USC you offered encouragement when I felt like I wasn't good or smart enough to keep going. Thank you for the numerous opportunities to travel and explore more of the world. I also thank you forteaching me how to think and write scientifically. But above all else, thank you for giving me the most valuable asset of all: a thick skin.

A warm thanks goes to my committee members, Alfred Garrett, Alexander Yankovsky, Subra Bulusu and Lew Lapine. Thank you for sharing your thoughts and ideas during our discussions. Your insights greatly enhanced the quality of this dissertation. I also thank you for offering words of encouragement over the years, and especially near the end of the program. I feel very lucky to have had such a great committee.

Finally, I would like to thank my friends and colleagues at USC. In particular, Legna Torres, Si Chen, Nirnimesh Kumar, Jason Walker, Kyungho Jeon, Matthew Balint, and Joe Bell. Thank you all for offering the kind of support, compassion and encouragement that only fellow graduate students can offer.

ABSTRACT

Overmarsh circulation is highly complex with variations in current direction over very short timescales and flowpaths that differ substantially between flood and ebb cycles. Understanding such flow complexities in salt marshes is important because they inherently impact the distribution of sediment, larvae and nutrients throughout the marsh, and hence, the ecogeomorphic feedbacks that control landscape evolution. The purpose this Ph.D. research is to quantitatively evaluate the effects of salt marsh topography on overmarsh circulation in a Georgia salt marsh.

This dissertation is comprised of three parts. First, digital elevation models (DEMs) were compared to characterize how well airborne lidar (light detection and ranging) data depict the microtopography of a salt marsh. 72,000 GPS points and 700,000 lidar points from a 1km^2 salt marsh island were linearly interpolated using identical DEM configurations. 1D comparison between the two surfaces indicates that lidar is a robust tool for mapping intertidal landscapes. However, in a 2D or 3D sense, lidar DEMs do not adequately resolve the microtopographic variations of a salt marsh, and for research questions that require accurate depiction of small scale tidal creek networks and subtle terrain features lidar data should be augmented with other information. Therefore, in the second part of this work we apply a high resolution, high precision GPS DEM to numerical simulations in Delft3D to characterize complexity in overmarsh circulation over a 1.4km^2 salt marsh basin. The model results provide a robust representation of field conditions and reveal that at times not necessarily linked to the transition between flood and ebb, the current magnitude and direction were highly dynamic, with variations occurring on the order of tens of minutes. Model results show simultaneous flow divergence and convergence, concentrated flow, as well as large-scale rotational flow. Also, all spatial scales show strong differences between flood and ebb pathways, which gives rise to 53% transport of the dye export via overmarsh and intertidal creek flows, and 32% exiting through the central subtidal channel system; 15% remained in the system after five days. The complexity in overmarsh circulation arises from the submergence and emergence of salt marsh topography. In the final part of this work I systematically smooth the high resolution GPS DEM to answer the question: How much topographic detail is needed to accurately simulate overmarsh circulation? Topographic smoothing progressively reduced the basin drainage density by 97%, and in the course of averaging removed small scale intertidal creeks and creek networks. Nevertheless, simulation results show nominal effects up to a 50m x 50m grid smoothing whereupon a system-wide change from ebb to flood dominance occurs. Moreover, assessments of dye circulation reveal that tracer residence time appears to be set by the geomorphic structure of the basin. Overall, smoothing out small scale intertidal creeks and creek networks reveals their minor role in overmarsh circulation, while excessive smoothing caused the system to change from ebb to flood dominance.

Table of Contents

LIST OF TABLES

LIST OF FIGURES

CHAPTER 1

FOREWORD

Salt marshes remain the focus of intensive study due to their ecosystem functions and more recently in response to the unknown effects of sea level rise on their overall stability. In a sense, salt marshes act as coastal floodplains that store water and serve as depositional zones for marine and terrestrial sediments. Salt marshes are also highly productive with a net primary production that ranges from 650 to 3700g dry biomass m^{-2} yr^{-1} (Teal, 1962; Williams and Murdock, 1966; Odum and de la Cruz, 1967) and are, therefore, an important nursery habitat for economically important fisheries (Cain and Dean, 1976; Weinstein, 1979; Wenner and Beatty, 1993; Lipcius et al., 2005). Furthermore, salt marshes help protect terrestrial lowlands from erosive tide and wave energy (Moller et al., 1999; Allen, 2000). All of the benefits of intertidal ecosystems are sustained by the interactions between physical and biological processes which operate within the context of an evolving salt marsh landscape.

When conducting field work in an inundated salt marsh one can observe suspended and floating material in transit, and this material can change speed and direction several times in a matter of minutes, and without the aid of wind. Here, I refer to the high temporal and spatial variability in overmarsh currents as “complexity”. Understanding the controls and scales of current complexity in salt marshes or tide influenced wetlands is important because in many cases it may strongly influence the distribution of suspended and dissolved nutrients (Valiela et al., 1978), larva distribution (Knieb, 1984), and contaminant dispersal (Nixon, 1980; Blanton et al., 2010).

Field and numerical studies indicate that the primary controls on salt marsh circulation and associated material redistribution include vegetation drag (Leonard and Luther, 1995; Christansen et al., 2000; Leonard and Reed, 2002; Temmerman et al., 2005) and topography (French and Stoddart, 1992; Lawrence et al., 2004; Torres and Styles, 2007; Chen and Torres, 2012). However, the detailed bathymetry or high resolution DEMs necessary for assessing the role of very subtle relief of salt marshes on overmarsh circulation typically are not present, and consequently the role of topography could not be fully evaluated. For example, Temmerman et al. (2005) used numerical simulations on a 0.05km^2 salt marsh catchment to assess the interactions of topography, vegetation, and water level fluctuations on spatial variations in flow and sedimentation. Their flow domain was derived from a lidar DEM with 3m point spacing and a vertical accuracy of 0.13m. Hence, effects of depressions and creeks less than 3m wide were precluded. On the other hand, their model validation showed that the 3m DEM point spacing did not noticeably influence simulation results. In a related study of flow sensitivity to DEMs McKean et al. (2014) introduced random errors to a lidar DEM to assess the effects on 2D hydrodynamic simulations in a gravel bed stream, and they also found nominal effects.

Cea and French (2012) investigated the sensitivity of hydrodynamic simulations to uncertainties in bathymetry and bed friction in subtidal, low intertidal, and high intertidal sub-regions of an estuary. In contrast to the studies above, they found a strong response in current velocity to bathymetry, whereas water level fluctuations were more influenced by bed friction. Also, numerical simulations by Blanton et al. (2010) successfully replicated tidal driven flows through a salt marsh but their tracer results were not as robust due to tracer retention in the marsh interior. These results led the authors to speculate that salt marsh circulation is highly sensitive to small scale variations in topography, and in particular to the effect of smaller "capillary" creeks less than 1m in width and depth. Taken together, these studies highlight the important point that researchers have yet to characterize, the role of small scale topographic structure on salt marsh circulation.

The goal of this dissertation is to investigate the interactions of topography and currents for a flooding and ebbing salt marsh. Here, I use field observation, remote sensing and numerical simulations in Delft3D to quantitatively answer the research question: How much topographic detail is needed to accurately simulate overmarsh circulation and dye transport? This work provides a deeper understanding of salt marsh morphodynamics and ecosystem stability.

SCOPE OF THIS DISSERTATION

There are three parts to this study; the first is related to developing a high resolution DEM (digital elevation model) of a salt marsh, and two are on simulations of overmarsh currents using the hydrodynamic model Delft3D. In the first part of this work, Chapter 2, a 1km2 salt marsh island near Georgetown, SC was surveyed with high precision RTK GPS and lidar (light detection and ranging). The DEMs were quantitatively compared to characterize well airborne lidar can depict the microtopography of the salt marsh. I discovered that 78% of lidar elevations were within +/- 0.25m of the high precision GPS elevations. However, spatial arrangement of elevation differences revealed that the lidar technology failed to resolve the overall structure of the salt marsh. Therefore, in a 1D sense lidar appears to be a robust tool for mapping intertidal landscapes because the majority of elevations were within the accepted range of accuracy. But in a 2D and 3D sense, the technology does not capture the subtle geomorphic structure of the landscape. Therefore, for research questions that require accurate depiction of small-scale tidal creek networks and subtle terrain features GPS surveys are optimal, and lidar surveys should be augmented with other elevation information.

In Chapter 3, I studied the complexity in salt marsh circulation using field observations, dye tracer and numerical simulations. The marsh bathymetry was created with RTK GPS surveys to map intertidal creeks greater than 1m wide. Model calibration and validation were quantified, and the model results provide a robust representation of field observations of pressure, velocity and dye concentration. Moreover, the spatial distribution of simulated dye mimics the distribution observed in aerial photographs following a dye tracer release. Next, I assessed flow at four spatial scales ranging from 1m - 1,000m and highlight the spatial and temporal variability of processes that give rise to overmarsh circulation. At times that were not necessarily linked to the transition between flood and ebb, the current magnitude and direction were highly dynamic occuring on the order of tens of minutes. Model results show simultaneous flow divergence and convergence, and focused flow, as well as large scale rotational flow. Also, assessments of dye circulation reveal that 53% transport of the dye export via overmarsh and intertidal creek flows, and 32% exiting through the central subtidal channel system; 15% remained in the system after five days. Hence, water parcels entering the system during flood do not necessarily exit by the same flowpath during ebb. Overall, I found that most of the modeled current complexity appears to be set by submergence and emergence of salt marsh topography.

In Chapter 4, I progressively smooth the high precision GPS DEM to reduce topographic resolution. The series of smoothed DEMs is used in hydrodynamic simulations to quantify the effect of bathymetric smoothing on dye transport, and overmarsh flow. The primary goal of this work is to address a fundamental question in numerical simulations of natural landscapes: How much topographic detail is needed to accurately simulate flow processes? In addressing this question I am able to develop deeper insight into the role of intertidal creeks in overmarsh circulation. In this part of the study I use iterative comparisons between simulations resulting from initial and smoothed DEMs and quantify changes in dye transport and residence time, free surface elevation, velocity, flux and local currents.

CHAPTER 2

A COMPARISON OF GPS AND LIDAR[1] SALT MARSH DEMS[1]

---

[1] Jessica Chassereau, Joseph Bell and Raymond Torres, 2011, A Comparison of GPS and Lidar Salt Marsh DEMs. Earth Surface Processes and Landforms, 13(36), 1300-1400.

Reprinted here with permission of publisher.

2.1 ABSTRACT

Digital elevation models (DEMs) were compared to characterize how well airborne lidar (light detection and ranging) data depict the microtopography of a salt marsh. 72,000 GPS points and 700,000 lidar points from a 1km^2 salt marsh island were linearly interpolated using identical DEM configurations. Overall, 78% of lidar elevations were within ±0.15m of the high precision GPS elevations. Spatial arrangement of difference values reveal that lidar performed best on the marsh platform, and poorly along tidal creeks and creek heads. Also, the overall shape of the salt marsh was poorly defined, even where lidar data were within the reported range of accuracy. These observations indicate that lidar appears to be a robust tool for mapping intertidal landscapes. However, lidar DEMs may not adequately resolve the microtopographic variations of a salt marsh, and for research questions that require accurate depiction of small scale tidal creek networks and subtle terrain features lidar data should be augmented with other information.

2.2 INTRODUCTION

The horizontal and vertical accuracy of airborne lidar data are variable, principally dependent on the technical specifications of the sensor and peripherals, on mission specifics and terrain attributes (Kraus and Pfiefer, 1998; Baltsavias, 1999; Hodgson and Bresnahan, 2004). Nevertheless, most lidar service providers deliver data with vertical accuracies of about ±0.15m when compared to surveyed ground points (Baltsavias, 1999), and with a comparable root mean square error (rms) for bare earth returns (Hodgson and Bresnahan, 2004). Filtering can potentially improve the overall accuracy where surface and terrain features are considered less optimal due to dense vegetation canopy and steep slopes. For example, Kraus and Pfiefer (1998) used an iterative algorithm based on linear prediction of ground returns to remove vegetation effects in woodlands. The raw lidar dataset had an accuracy of ±0.25m but their filter yielded a bare-earth model with an accuracy of ±0.10m. Vosselman (2000) implemented a slope-based filter, and Sithole and Vosselman (2004) concluded that filtering algorithms work best in gently sloping terrain with small buildings and sparse vegetation. Photogrammetric processing techniques are also used to improve the accuracy of lidar by supplementing the detection of break lines and stream edges (Lane, 2000; Carter et al., 2001; Hicks et al., 2002; James et al., 2006).

These studies indicate that lidar may be appropriate for applications in low lying coastal marshes and wetlands. For example, Montane and Torres (2006) directly compared a random sampling of lidar points to high precision GPS points and determined a vertical lidar over estimation of 0.07m for the vegetated marsh platform, with taller vegetation along creek banks giving rise to greater error. Moreover, several studies report <0.05m vertical accuracy for the salt marsh platform based on results from moving-window smoothing (Yang, 2005; Wang et al., 2009). However, such filtering diminishes the microtopographic structure of salt marshes (Lohani and Mason, 2001) that has been shown to exert strong local control on over marsh currents (Torres and Styles, 2007; Blanton et al., 2010). Nevertheless, lidar DEMs have been an important component to studies in salt marsh circulation and morphodynamics (Temmerman et al., 2005; Fagherazzi et al., 2006).

The purpose of this study is to evaluate how well a salt marsh lidar DEM can replicate a high accuracy, high precision GPS surface. In this sense, we propose to conduct a 3D assessment of lidar technology for the microtopography of a salt marsh island based on a 72,000 GPS point DEM. Here we adopt a holistic approach by comparing DEMs from an entire salt marsh island. The island is taken as a geomorphic unit of landscape defined by subtidal channels and with a range of landscape attributes including intertidal creeks, depressions, platforms, levees and variable vegetation cover (Novakowski et al., 2004). Effects of the nominal 0.15m accuracy often quoted by lidar service providers, and the validation approaches taken to improve vertical lidar "accuracy" need further scrutiny, especially with salt marsh applications. This is especially important given the effects of microtopography on overmarsh circulation (Blanton et al., 2010) where the total platform relief may be a few decimeters and the elevation uncertainty may or may not adequately depict the 3D structure.

2.3 STUDY SITE

The study was conducted on Maddieanna Island, a small salt marsh island in the North Inlet-Winyah Bay estuary, near Georgetown, SC (Figure 2.1a). The estuary is a relatively pristine mesotidal, ebb dominated lagoonal estuary that drains $32km^2$ of intricately networked salt marsh tidal creeks and channels. Tides are semi-diurnal with a mean range of 1.50m (NOAA tide gauge #8662299). The island is located at the western edge of the estuary; approximately 1.5km from the terrestrial boundary. The island is $1.05km^2$ of uninhabited salt marsh dissected by 24 tidal creeks varying in size and cross-sectional geometry (Bell, 2009). The island is bound to the north by a major subtidal channel and to the south by channels fed by Winyah Bay (Figure 2a).

The island is predominantly flat with most relief associated with channel networks. Unvegetated channels range from $^{-}1.36$-0.00m (all elevations referenced to

NAVD88); the marsh platform occurs between 0.00-0.32m, with levees and upland marsh from 0.32-0.78m giving 63% platform, 29% levee, 6% creek and 2% for surface depressions (Bell, 2009). The 0.0m elevation approximately corresponds to the transition between vegetated and unvegetated salt marsh. The vegetated marsh surface forms a monoculture of *S. alterniflora* from mid tide or higher (Morris et al., 2005). Short S. alterniflora grows on the platform and levees with stem heights of 0.15- 0.55m; tall spartina occupies the lower marsh and creek banks with stem heights up to 1.70m (Bell, 2009).

2.4 METHODOLOGY

The 72,000 GPS points were collected on foot from 2000-2002 using real time kinematic total stations with Trimble 5700 dual frequency receivers. The data have ~5m spacing on the marsh platform, 0.5-2.0m spacing along levees, and 0.25-0.50m spacing along creek banks; this higher density was needed to characterize the channel edge (Figure 2.1b). Horizontal and vertical measurements were referenced to the NAD1983 (2001) and NAVD88, respectively. GPS observations and difficult field conditions provided a practical accuracy of 0.04m vertical and 0.04m horizontal, and were used in calibrating the lidar mission and validating lidar elevations (Tamura et al., 2002; Hodgson and Bresnahan, 2004).

The lidar mission was flown by the National Oceanic and Atmospheric Administration (NOAA) on August 25, 2003. The mission began at 12:35 pm during a falling tide. An Optech 1233 ALTM lidar system was onboard a Cessna Citation at an altitude of 1,219m at 160 knots, yielding a post spacing of 1.40m. Following Sheng (2008) we estimated an at nadir laser footprint of 0.24m. There were six flight strips flown in a north-south direction with the three inner strips covering the island. Approximately 700,000 lidar points from the inner flight strips were used for this study. The lidar elevations were delivered as ellipsoid heights, and orthometric heights were calculated. First and last returns were not labeled as ground or vegetation. To reduce vegetation effects while avoiding smoothing of the data the lidar points were filtered such that all last returns having a separation of 0.15m or more from the first return were kept for the study. The lidar data were imported into ArcGIS and combined into a single point shapefile.

Since the 72,000 GPS points were collected at variable point densities, the dataset is spatially biased with 57% of observations falling below 0.0m, or on 6% of the island area. To facilitate an unbiased comparison, the GPS and lidar data were linearly interpolated using a 0.25x0.25m grid with $8.1\text{x}10^6$ nodes. The grid spacing corresponds to the finest spacing in the GPS data along creek edges. The GPS elevations were taken to be "true ground", and the signed error was computed for each location (Equation 2.1 after Hodgson and Bresnahan, 2004; Wang et al., 2009).

$$\mathrm{SE} = (\mathrm{lidar}_z - \mathrm{GPS}_z) = \begin{bmatrix} \geq 0.15 = \mathit{overprediction} \\ \pm 0.15 = \mathit{accepted\ accuracy} \\ \leq {}^{-}0.15 = \mathit{underprediction} \end{bmatrix} \quad (2.1)$$

DEMs based on the gridded elevations were created using geoprocessing tools. In order to minimize interpolation artifacts at the island perimeter we removed the outer most 5 pixels of both DEMs resulting in a net omission of 3.4% of gridded points. A surface map showing the spatial arrangement of SE was then generated using spatial analyst tools.

2.5 RESULTS

The histogram of interpolated GPS elevations is unimodal and ranges from $^{-}$1.36m-0.78m (Figure 2.2a). The mean elevation is 0.21m and the mode is 0.25m, indicating a negative skew. The curve centers on the mode with the majority of elevations falling between 0.0m-0.60m. The median elevation is 0.21m. The standard deviation of the distribution is 0.18m. Figure 2a also shows the distribution of interpolated lidar elevations which range from $^{-}$1.21m- 2.06m. The mean elevation is 0.24m and the mode is 0.26m. The mean value is less than the mode indicating that the curve has a negative skew. The curve centers on the mode with the majority of elevations falling between 0.0m-0.70m. The median elevation is 0.21m. The standard deviation of the distribution is 0.27m.

Overall, the distributions and shapes of the two histograms are similar (Figure 2.2a). Both curves have negative skews. Each has a single peak, and similar modes; differing only by 0.01m. The median of both datasets are identical, but the comparison also shows some differences. For example, the GPS data extends 0.15m lower than the minimum lidar elevation. Also, the maximum lidar value is 1.28m higher than maximum GPS value. The mean of the lidar dataset is 0.04m greater than the mean GPS elevation. The standard deviation of the lidar dataset is 0.09m greater than that of the GPS distribution. Furthermore, a parametric test for equality between GPS and lidar means reveals a significant difference at a very high confidence interval (alpha = 0.005); indicating that the two datasets are statistically significantly different.

Taking the difference between interpolated elevations resulted in SE values ranging from $^{-}$1.38-2.40m (Figure 2.2b). Although the range in SE is quite large, the mean SE value is only 0.05m with a standard deviation of ±0.28m. The median value is $^{-}$

0.03m with a mode of $^{-}$0.13m. Furthermore, the majority of SE values (78%) are within the accepted accuracy range of ± 0.15m. 11% of error values fall between 0.15m-0.55m. Error values ranging from 0.55m-2.40m comprise 4.9% of the dataset. Values falling between $^{-}$0.15m-$^{-}$0.55m represent 6%. A small percentage of error (0.1%) is associated with elevation differences that yield negative values ranging from $^{-}$1.20m-$^{-}$0.55m. These results indicate that in a 1D sense lidar may be appropriate for measuring salt marsh topography.

Figure 2.3a shows the salt marsh DEM constructed using the interpolated GPS points. The DEM uses a classified color ramp with a 0.2m interval to show the elevation break points that are associated with salt marsh features. The GPS DEM reveals a well-defined trough structure in the center of the island which indicates hydraulic connectivity between the creek networks. Also, there is a distinct slope in the marsh platform between the large continuous levee along the eastern border of the island to the low marsh in the west; the “source area” of tidal creek networks. Also, the intertidal creeks and channel networks are well-defined. For example, the one creek to the east shows a clear network structure, connection to the lower marsh, and a possible connection to the creeks along the western portion of the island. Small scale features are also noticeable; such as surface depressions at creek heads and smaller discontinuous levees along most intertidal creeks.

Figure 2.3b shows the salt marsh DEM created with the interpolated lidar points. The lidar DEM has a subtle east to west transition in elevation but a strong south to north transition from higher to lower elevations. The overall shape and general pattern of creek networks are detected along the central and northern portions of the island. Creek structures become less resolved with distance from the mouth, and they show apparently spurious rises in the creek beds. The DEM indicates that creek structures become less frequent to the south and the southern creeks are surrounded by unusually high levees. Several marsh depressions appear near creek heads, while others are not as clear and do show an apparent association to creek structures.

Comparing figures 2.3a and 2.3b indicates that lidar data does not have a comparably defined GPS surface. For instance, the slopes and general bowl structure in the GPS data are poorly replicated in the lidar data. Also, the elevations along the eastern side of the island are slightly lower than the platform and there is no clear pattern in topographic relief. In the GPS DEM lower elevations relate to surface depressions and creeks while higher elevations relate to the marsh platform and levees. In the lidar DEM, low and high elevations do not seem to relate to the intuitively correspondent morphology. Moreover, the basin or trough structure of the island interior is not clearly detected with lidar. The lidar DEM has 4% more surface depression, 10% less marsh platform and 6% more levee area relative to the GPS data. Also, the lidar DEM does not adequately replicate 1st order tributaries ≤1m in width and ≤ 0.15m deep, indicating that lidar data may not provide adequate representation of existing hydraulic connectivity for overmarsh circulation. Furthermore, the lidar DEM shows the branching of the main creeks being distorted by levees and high marsh. For example, it shows the tributary to the east being cut off at its bend by levees. This is also the case for most of the creeks to the west, where the meanders are blocked by levees, thus creating discontinuities in the creek structures. The surface depressions seen in figure 2.3a are replaced by exaggerated levees in figure 2.3b.

Figure 2.3c shows the spatial arrangement of SE. Areas of the study site where lidar accuracy is within the accepted range are typically associated with the marsh platform. Overall, SE values between 0.15-0.55m are found along the creek banks and in shallow depressions at the heads of first order creeks. SE values greater than 0.55m are limited to the southern part of the island, near creek mouths and in the marsh interior of the southwest. Most negative SE values occur near the outer edge of the northern part of the island, with the largest values along creek banks.

In summary, the structures shown in the salt marsh DEMs markedly differ. In fact, the southern one third of the island looks like a completely different landscape in the lidar DEM. The GPS DEM more clearly highlights the intertidal creeks, features which are most obvious in the field. Additionally, the GPS DEM displays the subtle spatial structure shown as sloping terrain, depressions at channel heads, and extension of tidal creek networks; topographic features that are likely to go unnoticed in the field. The lidar DEM does not replicate this fine scale topographic structure. In fact, the marsh topography is unclear, even in areas where lidar data were within the range of accepted accuracy. The findings are summarized in Table 2.1.

2.6 DISCUSSION

Overall, 78% of lidar elevations were within the accepted range of accuracy. In this sense, lidar is a robust and powerful tool for mapping elevations of intertidal landscapes. However, our observations indicate that the lidar DEM poorly resolves the topographic structure of the salt marsh. Hence, in a 1D sense, the lidar technology seems to perform well, but in a 3D sense, the technology appears incapable of resolving the fine scale topographic structure.

Poor lidar performance was most apparent along creeks and in low marsh areas (below 0.0m). As might be expected, these zones coincide with tall *S. alterniflora*, which forms a high canopy. Laser energy often fails to penetrate a dense vegetation canopy resulting in last returns that are well above the marsh surface (Jenson et al., 1998). Peak growing season at Maddieanna Island occurs during late summer and early fall and these lidar data were acquired in August of 2003. Thus, it is likely that mission timing, in part, contributed to many instances of last returns from the vegetation canopy rather than the ground surface.

Researchers have demonstrated that a range of filtering algorithms and photogrammetric techniques can be used to remove the effects of vegetation from the data (e.g., Lane, 2000; James et al., 2006). For example, Wang et al. (2009) applied a moving window technique that quantified the optimum radius for identifying ground lidar returns over the salt marsh platform. The resulting DEM had a calibrated accuracy of 0.06m, consistent with the error of Montane and Torres (2006). However, the Wang et al. (2009) filter was limited to the marsh platform since the smoothing effects would likely lead to the complete loss of narrow channel structures (Lohani and Mason, 2001). We used a simple filter which reduced the influence of vegetation without smoothing but did not eliminate all vegetation effects; thus contributing to the mean positive error value of our lidar dataset. The SE surface map (figure 3c) also showed negative error values which can be explained by the absorption of laser energy by water standing on the marsh surface and in creeks. It is likely that some water may have been in part of the creek networks and perhaps standing on the platform, even at low tide.

Lidar performance was optimal along the marsh platform and at higher elevations. The marsh platform (0.0m–0.32m) is vegetated, but the canopy is less dense and is occupied by the short form of *S. alterniflora* typically less than 0.50m high (Morris and Haskin, 1990). These conditions increase the likelihood that more laser energy will return elevations from the marsh surface. It is likely that the filtering techniques outlined by Wang et al. (2009) can be applied here to increase "accuracy" and help to resolve the subtle slope in the marsh platform, but at the expense of resolving 1st order creeks. Photogrammetric techniques implemented by James et al., (2006) and Carter et al. (2001) had success in correcting DEMs and the techniques could be applied here to improve lidar representation of creek structures. Also, increasing the point density of lidar data could increase the likelihood of detecting small scale topographic features which are often missed when sampling at a coarser resolution (MacEcheran and Davidson, 1987; Carter et al., 2001).

Overall, it seems that lidar DEMs without advanced processing do not adequately represent the fine scale structure of salt marsh landscapes. On the other hand, most of the lidar returns fall within the acceptable range of error for the technology, and therefore the viability of lidar for salt marsh research will depend primarily on the nature of the research question. Our results suggest that studies using a lidar DEM for spatial modeling of surface currents, sediment transport, or material cycling may yield different results relative to a higher precision flow domain or bathymetry. Thus, in cases where the research questions hinge on accurate representation of tidal creek structure and mircotopography we recommend augmenting lidar DEMs with data from other sources.

2.7 CONCLUSIONS

Comparing the interpolated GPS and lidar elevations we show that 78% of lidar data are within ±0.15m of the high precision GPS elevations. 15.9% and 6.1% of lidar elevations are higher and lower than the GPS elevations, respectively. Arranging the elevation differences spatially shows that lidar performs best on the marsh platform, and poorly along creeks, at creek heads and in low marsh. Although these1D results suggest that lidar is a powerful tool for mapping salt marsh elevations, our analyses reveal that the data sets are statistically significantly different. Moreover, in comparing lidar and GPS DEMs we show that lidar provides poor definition of the overall structure of the salt marsh island, even where elevations are within the accepted range of error. For example, the shape and extent of the marsh platforms are significantly different. Hence, for research questions that require the precise detection of small scale microtopographic features, typical of salt marsh landscapes, lidar DEMs should be supplemented with additional information. New remote sensing technologies that use microlasers, photon-level detection, and precise timing capabilities for 2D and 3D imaging; such as RULLI and L-SNR lidar (Roggemann et al., 2008; Cossio et al., 2010) will help overcome apparent technological limitations with complex intertidal landscapes.

Table 2.1 Summary of results from the GPS and Lidar DEM comparison. The table includes main findings related to lidar performance and associated terrain features.

SE Range	**% of Total SE Dataset**	**Terrain Features Associated with SE**	**Effect of SE on Surface Representation**
± 0.15m	78 %	Marsh Platform, levees	Overall structure is undefined; no apparent topographic slope; no connection between creeks
0.15m – 0.55m	11 %	Creek banks, creeks	Tributaries are unresolved and/or cut off by levees; exaggerated levees replace surface depressions
>0.55m	4.9 %	Creek heads, low marsh	Complete misrepresentation of the southwestern portion of the island
< $^{-}$0.15m	6.1 %	Outer edges of island, marsh platform, creek banks	Marsh platform is lower on average than seen in the GPS DEM.

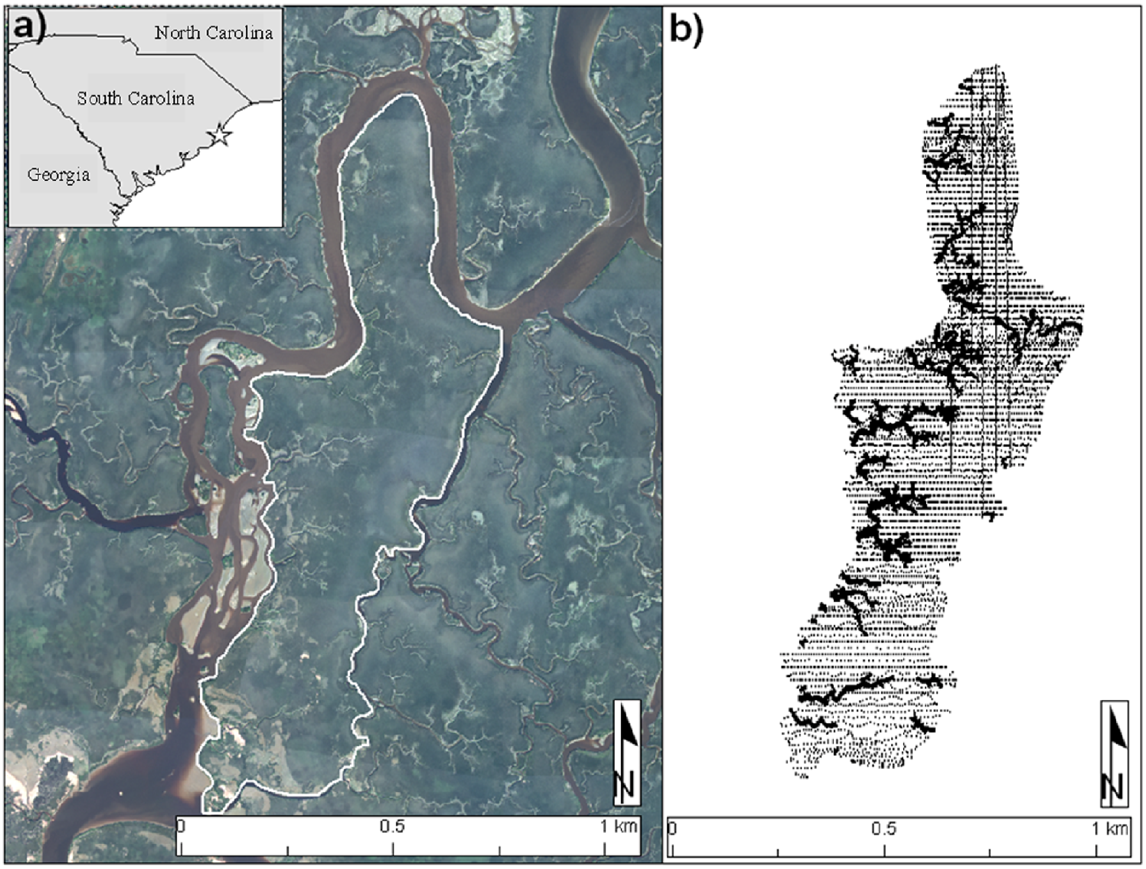

Figure 2.1 The study site: Maddieanna Island, SC (a). The figure illustrates the distribution of RTK GPS points used as reference data for the lidar assessment (b). Points were collected at a higher density near and within the creek structures.

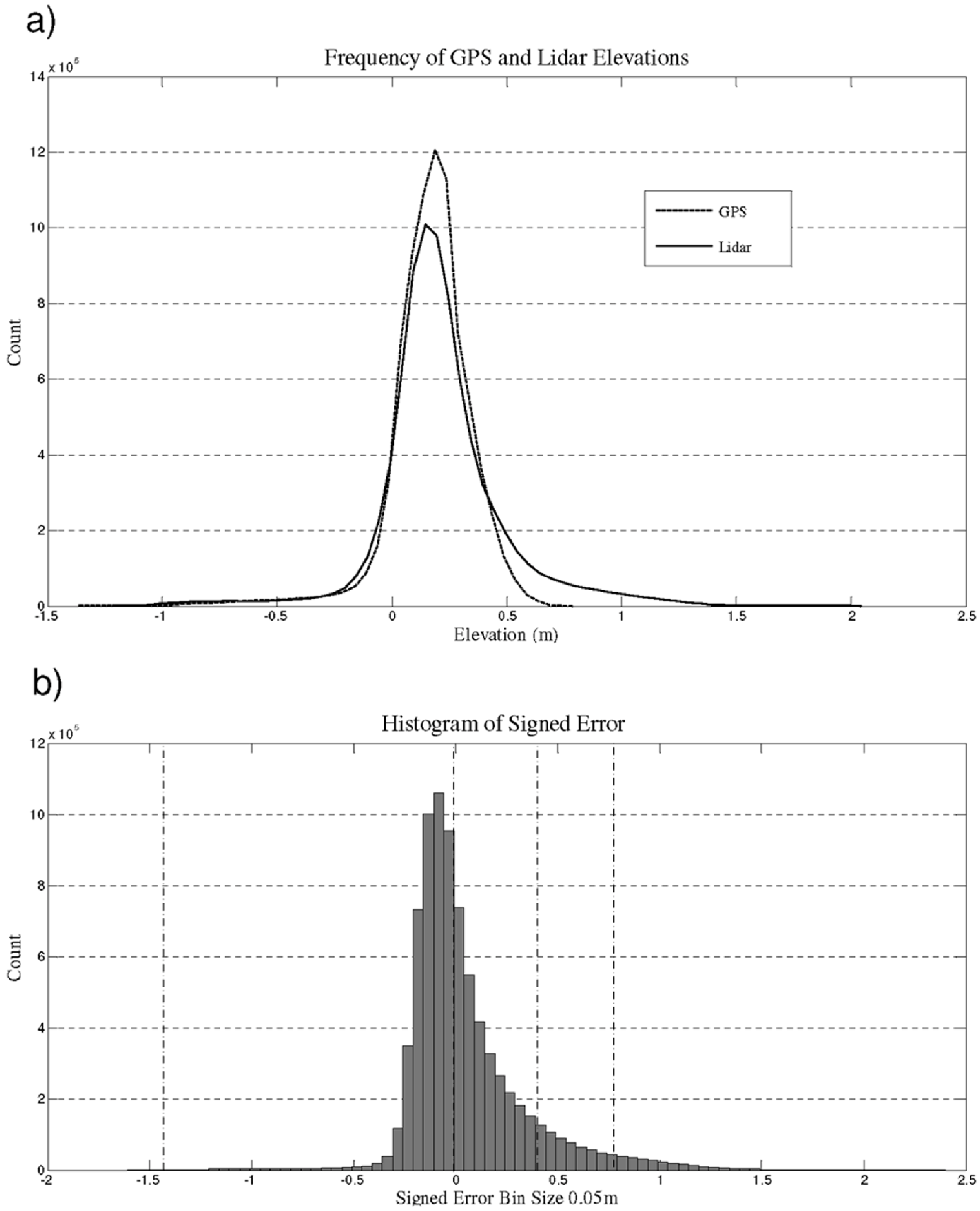

Figure 2.2 Histograms of GPS and lidar elevations (a). Values are based on regularly spaced grids created using triangulation with lenear interpolation. The figure represents the differences in interpolated elevations. Vertical dashed lines indicate breaks in slope associated with geomorphic classifications (b). There is a peak occurrence of SE between ± 0.15m.

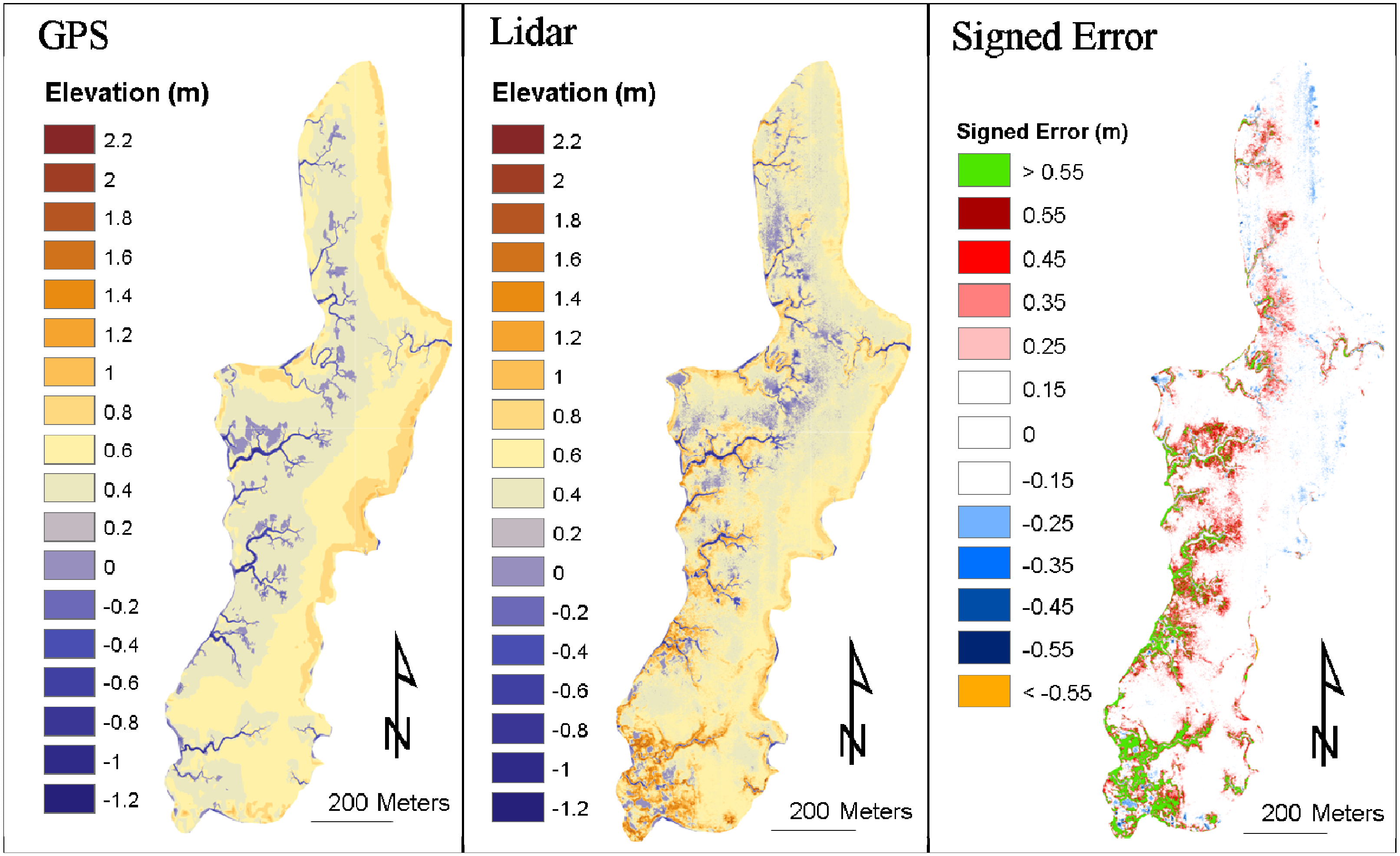

Figure 2.3 DEMs of interpolated GPS and lidar elevations (a and b, respectively). Warm colors represent high elevations. Cool colors represent low elevations. The figure also shows a surface map of SE (c); where white represents the accepted accuracy range (± 0.15m), shades of red represent SE values between 0.15m-0.55m, and shades of blue represent SE values between -0.15m - -0.55m. SE values greater than 0.55m and less than -0.55m are shaded green and orange, respectively.

CHAPTER 3

COMPLEXITY IN OVERMARSH CIRCULATION FOR A SEMI-ENCLOSED BASIN

3.1 ABSTRACT

We characterize complexity in salt marsh circulation over a 2km^2 basin using field observations, dye tracer and numerical simulations. The marsh bathymetry was created with high precision Global Positioning System surveys to map intertidal creeks greater than 1m wide. Model calibration and validation were quantified, and the model results provide a robust representation of field conditions in that model efficiency varied from 0.82 – 0.99 for pressure and velocity, and 0.36 – 0.83 for dye concentration. Moreover, the overall spatial distribution of simulated dye mimics the distribution observed in aerial photographs. We assessed flow at four spatial scales ranging from 1m – 1,000m, and highlight the temporal and spatial variability of processes that give rise to overmarsh circulation. At times not necessarily linked to the transition between flood and ebb, the current magnitude and direction were highly dynamic, with variations occurring on the order of tens of minutes. Model results show simultaneous flow divergence and convergence, concentrated flow, as well as large-scale rotational flow. Also, all spatial scales show strong differences between flood and ebb pathways, which gives rise to 53% transport of the dye export via overmarsh and intertidal creek flows, and 32% exiting through the central subtidal channel system; 15% remained in the system after five days.

Most of the modeled current complexity appears to be set by submergence and emergence of salt marsh topography and geomorphic structure.

3.2 INTRODUCTION

While conducting fieldwork in a salt marsh one can observe suspended and floating material in transit, and that this material can change speed and direction several times in the course of a tidal inundation. Of course, shifting wind conditions can account for surface water flow complexity, but overmarsh currents can vary substantially without wind effects (Kjerve et al., 1991; French and Stoddart, 1992; Leonard, 1997; Allen, 2000; Lawrence et al., 2004). Understanding the controls and scales of current complexity in salt marshes or tide influenced wetlands is important because in many cases it strongly influences the distribution of suspended and dissolved nutrients (Valiela et al., 1978), larva distribution (Kneib, 1984), and contaminant dispersal (Nixon, 1980; Blanton et al., 2010).

Field and numerical studies indicate that the primary controls on salt marsh circulation and associated material redistribution include vegetation drag (Leonard and Luther, 1995; Christansen et al., 2000; Leonard and Reed, 2002; Temmerman et al., 2005) and topography (French and Stoddart, 1992; Lawrence et al., 2004; Torres and Styles, 2007; Chen and Torres, 2012). However, the detailed bathymetry or high resolution DEMs necessary for assessing the role of very subtle relief of salt marshes on overmarsh circulation typically are not present, and consequently the role of topography could not be fully evaluated. For example, Temmerman et al. (2005) used numerical simulations on a 0.05km^2 salt marsh catchment to assess the interactions of topography, vegetation, and water level fluctuations on spatial variations in flow and sedimentation.

Their flow domain was derived from a lidar DEM with 3m point spacing and a vertical accuracy of 0.13m. Hence, effects of depressions and creeks less than 3m wide were precluded. On the other hand, their model validation showed that the 3m DEM point spacing did not noticeably influence simulation results. In a related study of flow sensitivity to DEMs McKean et al. (2014) introduced random errors to a lidar DEM to assess the effects on 2D hydrodynamic simulations in a gravel bed stream, and they also found nominal effects.

Cea and French (2012) investigated the sensitivity of hydrodynamic simulations to uncertainties in bathymetry and bed friction in subtidal, low intertidal, and high intertidal sub-regions of an estuary. In contrast to the studies above, they found a strong response in current velocity to bathymetry, whereas water level fluctuations were more influenced by bed friction. Also, numerical simulations by Blanton et al. (2010) successfully replicated tidal driven flows through a salt marsh but their tracer results were not as robust due to tracer retention in the marsh interior. These results led the authors to speculate that salt marsh circulation is highly sensitive to small scale variations in topography, and in particular to the effect of smaller "capillary" creeks or intertidal creeks less than about 1m in width and depth. Taken together, these studies highlight the important point that researchers have yet to characterize the role of small-scale topographic structure on salt marsh circulation.

Here we define overmarsh flow complexity as changes in current direction and magnitude that occur over short time intervals, and we use field observations of dye tracer dispersal and subtidal channel currents, and numerical simulations to understand the temporal evolution of and controls on overmarsh circulation. In particular we simulate salt marsh flood and ebb conditions over a high resolution and high precision salt marsh DEM to help unravel the role of topographic structure in spatial and temporal variations in salt marsh currents. Modeled pressure, velocity, and dye transport replicate field observations, and we use this information to evaluate complexity in overmarsh circulation at four spatial scales: the whole system or basin (1000m), macro (100m), meso (10m), and micro (1m) scales over a set of tidal cycles with the specific goal of providing a detailed account of basin inundation and drainage by assessing free surface elevation, tracer residence time, water balances and local currents. The assigned length increments of the four spatial scales are not necessarily meant to represent the length of individual flow assessments, but instead were taken to reflect the length scale of the underlying flow processes that we endeavored to highlight in this study.

3.3 STUDY SITE

The study site is a 2km^2 relatively isolated, section of a larger salt marsh system at 31.96°N, -81.02W°, ~20km south of Savannah, Georgia, USA (Figure 3.1). The local tidal regime is mixed, semi-diurnal and ebb dominant with a mean tidal range of 2.5m (Figure 3.2). The basin is semi-enclosed with forested land to the west and south where the forest-marsh edge is defined by a 1m - 3m bluff. The northern border of the study site is Groves Creek a sinuous, ~ 50m-wide subtidal channel that provides a connection between the salt marsh and the Wilmington River to the east (Figure 3.1).

The neap and spring tidal prisms are 8.11x10^{5}m^3 and 1.76x10^{6}m^3, respectively, based on the DEM volume between high water and low water elevations. The basin flushing-time, the hypothetical time for the exchange of one full basin volume (Equation 4 of Dyer, 1973) is 1.12 days and 0.52 days for neap and spring conditions, respectively.

These flushing-time estimates are similar to basins with comparable surface areas, volume, tidal range and tidal prism (e.g. Abdelrhman, 2005).

The vegetation is a monoculture of the smooth cordgrass *Spartina alterniflora* (*S. alterniflora*) with spatial variations in density and height dependent on surface elevation (Kostka, 2002; Blanton et al., 2010). For instance, tall form S. *alterniflora* with stem heights that exceed 2m and a density of about 112stems/m^2, grows on the high channel banks and levees. The short form, which typically occurs on the lower marsh platform, has an average stem height of 0.28m, and a stem density of about 446 stems/m^2. The vegetation heights and stem densities are based on clippings taken during a related study.

In order of higher to lower elevations the study area consists of 10% levee, 46% marsh platform, 13% low marsh, 19% intertidal creeks, and 12% subtidal channel. Levees may occur along the subtidal channel and intertidal creeks, and reach 0.75m - 1.30m (NAVD88). The marsh platform is a broad expanse of vegetated, low-relief landscape that forms between 0.45m - 0.74m and has a mean of 0.61m. The low marsh is sparsely vegetated and forms at the heads of intertidal creeks and in some areas form a large depression between 0.21m - 0.44m along an area of marsh east of the terrestrial boundary (Figure 3.1). Hereafter we refer to this area as the “marsh interior”.

Groves Creek is the main channel, and it is 3.8km along-channel from the furthest reach in the marsh interior to the mouth at the Wilmington River. From there it is 11km to the ocean. Groves Creek maximum depth is -4.50m at the mouth and declines to -0.80m inland; the corresponding bank-to-bank widths are 60m and 10m, respectively (Figure 3.3). At the site of our dye injection line, 2.2km from the mouth, the width is 35m and maximum depth is 4.0m (Figure 3.3). At 0.9km upstream of the injection line Groves

Creek splits into three main branches, for convenience called West, Middle, and East, with lengths of 1,100m, 700m, and 500m, respectively (Figure 3.1).

There are 88 intertidal creeks with mouth elevations ranging from -0.79m - +0.20m. The spacing between creek mouths is ~40m and maximum intertidal creek lengths vary from 10m - 500m. The creek widths range from <1m - 20m. Narrower creeks typically occur in the northern areas of the marsh, across levees. There is a complex network of creeks beginning after the fifth bend in Groves Creek that are connected at the heads by low marsh (Figure 3.3). This low-lying area provides a connection between the northern and southern marsh interior (Figure 3.3). A second complex network dissects an area of low marsh in the southeast, hereafter referred to as "dissected marsh" (Figure 3.1). The longest and deepest intertidal creeks in the basin are along the eastern marsh edge and they provide a direct connection between the marsh interior and the Wilmington River (Figure 3.1).

The tidal range at Groves Creek varies from 1.54m and 3.20m between neap and spring tides based on tidal oscillations observed at Station 1 (Figure 3.2). This study took place over a five-day interval from October 31 - November 5, 2010 when the tidal range was 2.1m - 3.2m (Figure 3.2). Hereafter, we refer to these minimum and maximum amplitudes as "neap" and "spring", respectively. The maximum water elevation during the neap and spring cycles was 0.78m and 1.45m, respectively. Therefore, at neap high tide the depth of water over the marsh platform was about 0.33m. During the spring high tide the water depth over the marsh platform was about 1.0m and the entire basin was submerged.

3.4 METHODS

3.4.1 FIELD DATA

Thirty-two kg of Rhodamine dye was released as a line source applied 80m south of, or “upstream” of Station 2 on November 1st, 2010 (Figure 3.3) at 15:55 GMT (all time reported hereafter are in GMT), approximately 1.5hrs after low tide. The duration of the dye application was 15 minutes over a single pass across the channel. The amount of dye used was computed to offset the effects of dilution from the tidal prism and preserve measureable dye concentrations in the marsh interior.

We also used a range of instruments that were installed in the subtidal system. The array includes Nortek Aquadopp acoustic Doppler current profilers (ADCP), SBE16 CTDs, ISCO automated dye samplers, and Wetlabs ECO FLRHSB Rhodamine fluorometers all deployed in various combinations at eight stations (Table 3.1). Automated dye information was augmented by manually collecting water samples from boats (grab samples). All submerged instruments sampled at 10-minute intervals, the ISCO sampling rate was hourly, and the grab-sampling rate varied from 1 – 5 minutes for 2 hours with finer temporal resolution over the 1hr passage time of the plume advance. All station locations are shown in Figure 3.3 and distances from the line source to the station are reported as along-channel distances. Station 1 was near the channel mouth 1,680m from the dye source. Station 2 had one bank on the forested bluff 80m north of the line source. Stations 3, 4, and 5 were in the East, Middle, and West subtidal branches, respectively. Station 6 was also in the West branch near the southern terrestrial boundary 1,760m from the line source (Figure 3.3). Station 7 was in the low marsh interior 1,490m east of the line source and 100m north of the southern terrestrial boundary. Station 8 was in the large intertidal creek along the eastern marsh edge 1,900m east of the dye source (Figure 3.3). Observed pressure and velocity from Stations 1-6 were used to calibrate the model described in the next section. The dye analyses and results described below include all available data (Table 3.1). In addition, a series of air photos taken during the experiment were used to qualitatively compare the simulated to observed dye distributions.

Trimble R6 GPS receivers were used to collect high-resolution topography three ways, by surveying points individually, with a SonarMite echo sounder for intertidal creeks, and with a Simrad multibeam system for Groves Creek. The higher elevations were surveyed at low water, and the soundings for intertidal creeks were made from a small motorized craft at high water. The survey consisted of 241 individual missions over 169 field days in 2010 and 2011 resulting in 1.6×10^5 points with spacing ranging from 0.25m – 5m. RTK corrections were received through a VRS (Virtual Reference Station) operated by eGPS Solutions, Inc. reporting 0.02m horizontal and 0.02m vertical accuracies when connected to the internet via cellular telephone. ArcGIS software was used to linearly interpolate the survey data onto a 1m DEM for use in hydrodynamic simulations with Delft3D (Figure 3.3).

3.4.2 MODEL DESCRIPTION, SETTINGS AND CALIBRATION

The Delft3D simulation package consists of integrated modules which interact to compute water currents, water quality, and particle transport for user specified bathymetry, roughness, horizontal eddy viscosity, and dispersion coefficients. The standard hydrodynamic module is Delft3D FLOW and it is essential for modeling flow phenomena where horizontal length scales are significantly larger than the vertical

(Lesser et al., 2000). Delft3D is well suited for this study and has been applied successfully to salt marsh research in several different locations (Temmerman et al., 2005, Marciano et al., 2005, Bouma et al., 2007 and Fagherazzi et al., 2014). Computation of unsteady shallow-water flow is determined through the horizontal momentum equation, the continuity equations, and transport equations. Bed roughness and horizontal eddy viscosity are both user defined and typically follow from calibration. Delft3D FLOW uses a finite-difference approach to compute water level and depth averaged velocity at each node. The FLOW output is subsequently coupled to the PART module to simulate the advection and diffusion of particles. Delft3D PART accounts for the random spreading of particles through the horizontal dispersion coefficient H_D defined by Equation 3.1 (Csanady, 1973)

$$H_D = at^b \quad (3.1)$$

where t is the age of the particle, and a and b are coefficients that emerge from the model calibration. For 2D flows the user must also specify a roughness length parameter, typically through calibration, which is used to calculate the logarithmic velocity profile.

The simulations were conducted on a grid with uniform 1m horizontal spacing giving $5\text{x}10^6$ computational nodes. The domain was closed to the west and south along the terrestrial border, and closed to the north along the outer bank of Groves Creek. The domain was open to flow along the eastern boundary defined by the water level time series from Station 1. The model assigns positive and negative values to flows in the direction of increasing or decreasing X or Y, respectively. In this study, the origin of the computational domain is to the left of the open flow boundary. Therefore, flood velocities are negative and ebb velocities are positive. The geographic orientation of the channel at

Station 5 introduces ambiguity into the direction of flood and ebb (Figure 3.3). Therefore, all velocities at Station 5 were multiplied by -1 to ensure that flood velocities in all cases were negative.

The model was calibrated with pressure and velocity data. The horizontal eddy viscosity was set to 0.0005m^2/s (Temmerman, et al., 2005) and bottom roughness was applied as a calibration variable by adjusting Manning's n values for vegetated (> 0.20m) and unvegetated (≤ 0.20m) marsh, constrained by the range of n values for salt marshes (Table 3.2), and by comparing results to observations. The model efficiency (ME, after Nash and Sutcliffe, 1970) was calculated with the entire time series record to guide model validation and to determine optimal values for Manning's n as described below.

$$ME = 1 - \frac{\sum_{t=1}^{T} (OBS(t) - SIM(t))^2}{\sum_{t=1}^{T} (OBS(t) - MEAN)^2} \quad (3.2)$$

OBS(t) is the observed value at time *t*, *SIM(t)* is the modeled value at time *t*, and *MEAN* is the mean of the full time series. ME values can range from -∞ to 1 with 0 indicating simulation results are no better than the mean, and 1 indicating perfect agreement between modeled and observed data. Negative values signify conditions where the mean is a better predictor than the model. The highest ME was obtained by applying a Manning's n of 0.017 and 0.10 for unvegetated and vegetated marsh, respectively (Table 3.2), similar to values determined by French (2003).

The modeled dye tracer was distributed over 7x10^6 particles, the maximum number of particles required to achieve the highest level of accuracy while maintaining computational stability. The accuracy of the tracer simulation was expressed as the smallest concentration that can be represented by a single particle in a computational cell.

In our case, the smallest detectable concentration was 4ppb. Horizontal dispersion parameters were set to a = $0.20m^2/s$ and b = 0.02, and a roughness length of 0.001m followed from model calibration. A computational time step of 0.025 minutes was used to establish numerically stable simulations, and results were output at 10-minute intervals. Dye concentrations are computed by dividing the total mass of particles in each computational cell by the cell volume.

3.4.3 MODEL VALIDATION

Visual inspection of observed vs. simulated pressure, velocity and dye concentration time series from the various stations shows that the model was largely successful in replicating the amplitude and timing for inundation and drainage. In particular, the model is highly efficient in simulating the time series at five of six stations (Figure 3.4). The simulated and observed data nearly overlie one another in five of the six stations and give a ME = 0.99. Station 2 has the least correspondence but maintains a robust ME = 0.92. However, the maximum and minimum water levels for each tidal cycle at Station 5 are offset by 0.10m – 0.20m, but this systematic offset appears to be a related to uncertainty in instrument position.

The ME assessment of velocity at a station was equally successful in most cases, with a range of 0.82 – 0.94 (Table 3.3), and the velocity asymmetry is well replicated (Figure 3.5). The peak flood and ebb velocities are also well represented for most stations, although Station 1 is underestimated by up to 0.20m/s at the higher stages (Figure 3.5). Moreover, peak flood velocities at Station 3 are consistently underestimated by 0.20m/s. Taken together the ME values indicate that the model is largely successful in its representation of stage and velocity at most stations.

Simulation results for the dye tracer at Stations 1, 2, 3, 3 grab, 5 grab, 6, 7 and 8 are overall successful in that the ME values are in the range of 0.30 – 0.83 (Table 3.3). Stations 1 and 2 have comparably large ME values of 0.83 – 0.82 but in both instances the peak concentrations are offset by 17ppb and 30ppb, respectively (Figure 3.6). The model is least efficient at Stations 3, 5 grab and 8 with ME of 0.36, 0.35 and 0.30, respectively. In these cases the overall shapes of the modeled dye responses are well-represented, but peak concentrations are offset by up to 140ppb and the timing of the modeled tracer is ~ 30 minutes earlier than observed. On the other hand, in all eight instances the offsets decrease with time (Figure 3.6), and more importantly all of the ME values are positive, indicating that the numerical simulations of dye movement are representative of field conditions, albeit at different levels.

3.4.4 GROVES CREEK CIRCULATION

We characterized overmarsh circulation with dye concentration data from measurements at eight stations throughout Groves Creek, and we investigated circulation over the entire Groves Creek basin by using the coupled FLOW-PART components of Delft3D to simulate the transport of a conservative tracer. The modeled dye distribution provided insight for determining the spatial scales of analysis needed to assess overmarsh circulation. We evaluated marsh circulation with maps of modeled free surface elevation, stage-velocity relationships, residence time, velocity, flux, and local currents at the fours scales of assessment.

In particular, the basin scale (1,000m) was assumed to represent spatial patterns in bulk average flows of water and dye that entered and exited the salt marsh system. Circulation at this scale was described using three approaches. First the elevation of the free surface during the spring tide was mapped over the entire marsh at 20-minute intervals beginning at 4hrs after low water and ending 4hrs after high water. Water elevation contour maps were generated in ArcGIS and the corresponding areas of inundation were calculated for each time interval.

The second approach made use of the proximity of Station 1 to the mouth of Groves Creek. Here we assumed that the "upstream" processes that affect flow at the mouth are encapsulated in the overall shape of the velocity – stage relationship for the spring tide. In this case we plotted the field data together with the simulated data to highlight the upstream geomorphic/topographic controls on a typical entry point for water in systems such as this, and the overall ability of the simulations to represent direct measurements.

The final measure relied on tracer residence time for the 5-day interval as calculated from concentrations at stations 1, 2, 3, 6, 7 and 8. Residence time helps characterize the time required for a parcel of water to hypothetically enter and exit the system, and it can help quantify spatial variations in transport processes (*Monsen et al.*, 2002). Assuming concentration of the tracer decreases exponentially with time and adopting equation 3.3 and 3.4 from Miller and McPherson (1991)

$$C(t) = C_o e^{-kt} \quad (3.3)$$

$$Rt = \frac{1}{k} \qquad (3.4)$$

where $C(t)$ is the concentration at time t, C_o is the initial concentration of the tracer, and k represents first order removal rate. Residence time (Rt) is simply the inverse of the removal rate.

Circulation was assessed at the macro scale to illustrate the spatial arrangement of velocity vectors computed over 60m x 60m grids. This grid size was selected through an iterative grid averaging process and we determined that it was the optimal grid size for the representation of macro scale flow processes. Thus, this grid size represents flows over and through the marsh interior that operate at scales on the order of about 100m. This scale was useful for shedding light on the internal circulation of the system during intermediate tidal stages as well as detecting and quantifying variations in flow paths between flood and ebb cycles. Vector maps of simulated depth averaged velocity were generated in Matlab to show circulation over a four-hour interval, two hours before and after the spring high tide.

Meso scale circulation refers to processes operating at a length scale of 10m corresponding to the flows between intertidal creeks. The meso scale approach included a flow assessment and water balance with a series of six transects across different parts of the marsh (Figure 3.3). Transect 1 encloses the marsh interior but was separated into two parts to account for flows between two different subtidal systems, 1a between the marsh interior and Groves Creek, and 1b between the marsh interior and the Wilmington River (Figures 3.1 and 3.3). Together transects 1a and 1b illustrate fluxes toward and away from the salt marsh interior. Therefore, net fluxes computed as the difference between inflows and outflows across these transects will reveal any overall water imbalance for the marsh interior. Transects 1a and 1b are 500m long and each consists of ten 50m long sections (Figure 3.3). This was advantageous for establishing transect flexibility with respect to geomorphic structure. Also, four 50m long transects (2a, 2b, 2c, and 2d) were positioned further into the basin (Figure 3.3) to determine flow characteristics within the marsh interior.

For all transects the magnitude and direction of net flux were computed at 10-minute intervals and total flood and ebb fluxes were summed over their respective 390-minute intervals. The convention for describing flux direction across transects 1 and 2 is expressed as positive (+) for outflow or ebb and negative (-) for inflow or flood (Figure 3.3). Thus, flood and ebb volumes that do not sum to zero indicate a preferential flow direction between flood and ebb cycles. Specifically, a + volume over transect 1 indicates net flow away from the marsh interior. Likewise, consistent + values for transect 2 collectively indicate net counterclockwise flow.

Finally, micro scale circulation represents flow at a 1m scale with particular attention to the spring tide because of the fuller salt marsh inundation. In this case flow was evaluated at two locations in two intertidal creeks with a series of ~90º bends or "dogleg" bends (Figure 3.3). The two locations were selected to show vectors associated with the east/west and north/south sections of the dogleg. Creek 1 is a first order creek with a bank elevation of about 0.47m (Figure 3.3). The creek bed elevations of the north/south and east/west reaches are -0.53m and -0.38m, respectively. Creek 2 is part of an intertidal system that dissects the southern marsh interior (Figure 3.3). The bed elevations of the north/south and east/west sections are -0.60m and -0.66m, respectively, and the bank elevation is about 0.40m. Information on the dynamics of in-channel current direction and magnitude at these sites is useful because it can shed light on when channel structure no longer controls depth averaged flows. For example, flows with a uniform direction over a dog-leg indicate that larger scale pressure gradients dictate current directions and magnitude, and not the creek banks. In this way, the micro scale analysis highlights local vs. basin scale controls on current complexity.

3.5 RESULTS

3.5.1 DYE TRACER AT A STATION

Figure 3.6 shows the time series of concentrations at Stations 1, 2, 3, 3 grab, 5 grab, 6, 7 and 8 for both observed data and simulations. The field data show that the dye appears at Station 1 8hrs after release. This is consistent with the dye release “upstream” of Station 1, and on the rising tide; hence dye could not reach the station until ebb. The first peak is 45ppb and it coincides with low tide (Figure 3.6a). The peak duration is 20 minutes and concentrations decline to zero at high tide. Subsequent peak concentrations also coincide with low tide and decay with time. For example, successive peaks are 28ppb, 17ppb, 11ppb, 7ppb, and 4ppb, respectively, decreasing by ~ 40% with each cycle (Table 3.4). Also, the duration of the peaks progressively increases to 2hrs with the final tidal cycle.

The dye reaches Station 2 at the end of the ebb cycle 7.5hrs after the release, and again, because the station is “downstream” of the dye release. Peak concentrations occur at low tide and the first is 103ppb (Figure 3.6b) and lasts for 1.5hrs before declining to about 0 ppb at high tide. Subsequent peak values decay with time going from 52ppb, 30ppb, 18ppb, 11ppb, and 6ppb, again decreasing by ~ 40% with each cycle (Table 3.4). As with Station 1 the duration of the peaks increases with time and reaches a maximum of 4hrs.

Station 3 is upstream of the dye release and in the direction of transport on the rising tide. The concentration time series is more complex relative to the response at stations 1 and 2, in that it exhibits a persistent double peak that gradually diminishes over several tidal cycles (Figure 3.6c). The first peak occurs just after high tide on November 2nd is 130ppb and a second lower peak occurs on the rising tide. There is a local minimum that occurs between peaks at low tide and concentrations go to 0ppb at high tide. Peak concentrations decay with time going from 65ppb, 40ppb, 21ppb, 14ppb, and 8ppb (Table 3.4).

The observed time series at Station 3 grab reflects the 2.5-hour time interval over which grab samples were collected (Figure 3.6d and Appendix a). This station is also upstream of the dye release and initial concentrations reach the site about 1hr after the release. A peak concentration of 588ppb occurs just after low tide (Appendix a). Concentrations decline on the rising tide and go to zero 1.5hrs after the initial peak.

Similarly, grab samples were collected at Station 5 grab and the time series reflects the 2.5hr-sampling interval (Figure 3.6e and Appendix b). Station 5 grab is located upstream of the dye release in the West branch of the subtidal system. The dye plume reaches the station about 1hr after release. The largest concentration of all stations occurs as a peak of 1038ppb just after low tide (Appendix b).

Station 6 is upstream of the dye release and the response is much more complex and variable relative to the responses of other stations. The largest concentration for the time series occurs as an initial peak coinciding with the rising tide 3hrs after the dye release (Figure 3.6f), giving an average dye velocity of 0.16m/s. This peak goes from 0ppb to 530ppb, with the return to 0ppb occurring just before peak tide. This is followed by a double peaked interval with successive peaks occurring at mid tide during one rise-fall interval. Concentrations decline rapidly with time and the peak duration increases from 4hrs to 8hrs (Figure 3.6f). Subsequent increases in concentration lack the double peak and give more of a plateau response, and successive plateau values decline at a rate of 35-40%. Another apparently consistent response in this dye time series is smaller and relatively short-lived peaks that occur just after high tide, or just before the concentrations reach the plateau values.

Station 7 is located further into the marsh interior between the subtidal system and the eastern marsh edge. The initial peak of 170ppb occurs during the first ebb tide, about six hours after the dye release (Figure 3.6g). Station 7 is dry at mid to low tide and this resulted in gaps of the time series. Peaks occurring during the subsequent ebb tides decrease exponentially from 89ppb, 54ppb, 38ppb, 21ppb, 16ppb, and 8ppb (Table 3.4).

The Station 8 data have a response similar to that of Station 1 and 2 in that they increase from zero to a consistently higher range over an interval of about four hours midway between the ebb and flood phase, and the peak values decline with each successive tidal cycle (Figure 3.6h). However, the data differ in that at the onset of the higher four-hour interval the concentrations attain an initial peak before declining to a quasi-steady, higher value (Figure 3.6h). The initial dye response occurs 7hrs after the release and peaks at 79ppb. Tracer concentrations decay exponentially with time decreasing by ~ 40% with each cycle and with 5ppb remaining after six tidal cycles (Figure 3.6h), and the duration of the peaks is consistently 5 hours.

In summary, peak concentrations range from 45ppb-1038ppb (Table 3.4), and at all sites the timing of peaks coincide with low tide. Also, concentrations go to zero at high tide and decay exponentially between tidal cycles. Moreover, there is an initial spike in concentration at Stations 3, 3 grab, 5 grab and 6, but both Stations 1 and 2 have a single peak per tidal cycle. Hence, the stations in the ebb direction of the injection line have single peaks whereas those in the flood direction have multiple peaks.

Table 3.4 highlights simulated and observed peak concentrations, and the mean time series concentration for Stations 1 - 8. Overall, the table shows that the initial modeled peak concentrations are typically underestimated by 10ppb – 400ppb with the largest offset occurring at Station 5, but in all cases the differences decline with each successive tidal cycle (Table 3.4). By the end of the simulation most of the peak differences are less than 10ppb. The model also captures an initial peak of 150ppb at Station 3, but is completely missed by the hourly observation data (Table 3.4). Also, in all eight instances the mean of simulated and observed concentrations are very similar. In fact, the means are identical at Stations 1 and 6, and are only different by 1ppb – 40ppb at the other six sites, and with the largest mean differences at Stations 3 grab and 5 grab where the time series of observation data is the shortest (Table 3.4).

In summary, the model results mimic the observed data but there are substantial differences. Typically, the early simulation results are least representative with initial peak offsets of up to 400ppb, but they improve with time because the actual and simulated dye concentration gradients decrease with time as the plume spreads out. In addition, plotting the model results with field observations illustrates that there is an initial 30 minute offset between observation and simulations, and more importantly that this offset declines with time. Moreover, taking the mean of the time series removes phasing issues and reveals strong agreement between observed and simulated data. The model also captures the initial peak at Station 3 that was completely missed by the observed data.

3.5.2 DYE TRACER OVER THE BASIN

Simulation results show that two hours after dye release (three hours before high tide) there is dye transport along Groves Creek with a faster moving core (Figure 3.7a). This results in a 0.40km - 0.70km long low concentration (< 50ppb) tail on either side of Groves Creek and higher concentration center plugs (> 500ppb) reaching the marsh interior through the subtidal branches (Figure 3.7a). For instance, high concentrations can be seen in the dissected marsh west of the Middle branch (Figure 3.7a, coordinates 4.976×10^5, 3.5368×10^6) and east of the middle branch (4.976, 3.5366). For brevity, we will no longer include the 10^5 and 10^6 factors when reporting coordinates. Lower concentrations are ~ 50ppb, located in Groves Creek to the south of the dye release and along the leading edges of the dye plume. Comparably high concentrations also occur in the much smaller intertidal creeks along the north side of Groves Creek, which facilitate dye transport toward the northeast and east (Figure 3.7a). In some cases the concentrations there exceed 500ppb and in all cases the dye is limited to the creek banks and downstream of the creek heads.

At three hours into the dye release or two hours before high tide the maximum concentrations remain about 500ppb but shifted eastward and southward (Figure 3.7b). This is apparent in the Middle and West branches where 500ppb concentration is located farther east relative to Figure 3.7a and they form a front along the marsh interior (Figure 3.7b). There is also a long tail of 500ppb to the west of the dissected marsh that is associated with westward transport along the southern terrestrial border (4.974, 3.5366). There are areas of high concentration in the dissected marsh west of the middle branch that surround a central area of relatively lower concentration, indicating convergence of flow from the north, west, and east (Figure 3.7b). At the same time, concentrations to the west and east of the middle branch are relatively higher than in the channel, indicating flow divergence. Lower concentrations < 50ppb occur along creek networks at higher elevations centered at 4.978, 3.5372, and in the subtidal channel branches, and along the dye plume fringes (Figure 3.7b).

The orthorectified and color enhanced image (Figure 3.8) represents the conditions at 19:32 GMT or 3.5 hours after the dye release. The photo shows areas of high concentration along the southern terrestrial boundary, the dissected marsh and in the low marsh east of the subtidal system. Also, the color enhancement highlights a faint arc of low concentration on the marsh platform north of and parallel to Groves Creek. The figure also shows the absence of dye. For instance, although we injected the dye into the subtidal system 80m south of Station 2, dye is essentially undetectable in Groves Creek and in most of the length of the three subtidal branches (Figure 3.8). Hence, the tidal circulation forced the dye from the subtidal to the intertidal zones.

The model results at 19:00 (Figure 3.7b) accurately mimic the presence of high concentration in the air photo (Figure 3.8), as well as the presence of otherwise visually undetectable concentrations of dye, indicating that the modeled dye reached this location 30 minutes ahead of the observations. Nevertheless, figure 3.7b shows that the distribution of dye between subtidal and intertidal zones is comparable. Moreover, the absence of dye and areas of lower concentration in figure 3.7b exactly match the spatial pattern of dye free areas recorded in the air photo. In fact, the model results enable the visualization of dye distribution of < 10ppb.

Figure 3.9a shows the dye simulations two hours after high tide. Concentrations are more dilute and range from 25ppb - 75ppb throughout the marsh interior and at the outer edge of the dye front. The front has a highly irregular shape with “points” that likely reflect overmarsh flow routing through intertidal creeks (Figure 3.9a). Also there are three areas of higher concentrations between 250ppb – 350ppb in the marsh interior (Figure 3.9a). One area is along the terrestrial border to the west (4.974, 3.5366). The second is to the east near the head of the major intertidal creek with Station 8, and the third occurs in the dissected marsh (4.976, 3.5368). Clearly, some dye leaves the system from the large intertidal creek along the eastern marsh edge (Figure 3.9a).

One hour later (three hours after high tide) the simulations show dye retention in the marsh but with limited extent, mainly confined to the south (Figure 3.9b). The ebb concentrations are much lower relative to Figure 3.9a, typically in the range of 25ppb – 60ppb with two areas of higher concentration of up to 150ppb in the southwest (4.972, 3.5367) and southeast (4.9808, 3.5369). The dye plume extends downstream of the injection point, and some trace amounts of dye leave the system through the mouth of Groves Creek while much more concentrated dye leaves through the major intertidal creek to the east (Figure 3.9b). The irregular-shaped and dilute dye front on the marsh platform to the north has an apparent uniform shape between figures, indicating that water at the heads of creeks does not flow through the intertidal creek system, but across them before entering Groves Creek (Figure 3.9b). The major intertidal system to the east is clearly an important part of salt marsh drainage as indicated by the higher concentrations feeding into it. In fact, we determined that 12% of the total dye mass exited the system from the eastern marsh edge, while 7% exited via the mouth of the main channel over the first full tidal cycle. Moreover, over the full five-day simulation interval we found that 53% of the total dye mass exited the system from the eastern marsh edge while 32% exited via the mouth of the Groves Creek. The remaining 15% was retained in the marsh interior.

In summary, the modeled dye transport results highlight the complexity in inundation timing and flow direction throughout the basin, and patterns of overmarsh circulation. The tracer reveals that the interior dissected marsh area first inundates from the east through the Middle branch, and subsequently from the west through the relatively longer West branch. Moreover, there is simultaneous flow divergence and convergence in the marsh interior. Also, the dye results show differences between flood and ebb circulation indicating that water parcels on the flood do not necessarily follow a similar but reversed path on ebb. Finally, after six tidal cycles most of the dye was transported out of the system via the eastern marsh edge.

3.5.3 Basin Scale Circulation

Figure 3.10 shows contours of the simulated free surface elevation during spring tide inundation. At 9:00 46% of the area is inundated and the water surface elevation is < 0.67m (Figure 3.10a). During this time water is confined to the subtidal system, some lower intertidal creek networks, and low marsh. Just 20 minutes later 72% is inundated including lower areas of the marsh platform; while the higher areas and levees are dry (Figure 3.10b). The free surface elevation is 0.76m along the eastern marsh edge, 0.71m in the subtidal channel and intertidal creeks, and <0.67m in the marsh interior. At 9:40 91% of the marsh is submerged, with mostly levees being subaerial (Figure 3.10c). The maximum water surface elevation is 0.87m along the eastern marsh edge and 0.79m in the marsh interior. At 10:00 98% of the marsh is inundated and only the highest levees along the main channel are dry (figure 3.10d). The water surface is 1.03m along the eastern marsh edge, 0.98m in the marsh interior, and 0.95m in the southwest. The distance between minimum and maximum elevations is 500m yielding a maximum slope of $1.6\text{x}10^{-4}$ toward the southwest and indicating inundation from the basin exterior and to a lesser extent intertidal creeks and Groves Creek. At 10:20 99% of the marsh is inundated and only the two highest levees along the first and third bend in Groves Creek are subaerial (Figure 3.10e). The elevation of the water surface is 1.15m along the eastern marsh edge and decreases to 1.11m in the west and the maximum slope toward the southwest decreases to $8\text{x}10^{-5}$. At this time the source of water inundating the marsh is from the basin exterior, rather than from subtidal and intertidal conduits. At 10:40 the entire marsh is inundated and the free surface elevation is > 1.25m. The two highest levees remain submerged over the final 20 minutes (Figure 3.10f).

Model results also show in-channel variations in surface water topography. At 9:20 there is a 0.03m higher water level along the outside bank of the second bend in the channel. More importantly, the same phenomenon occurs at bends along Groves Creek, far from the domain boundaries. This accumulation of water in channel bends has been reported by (*Georgas and Blumberg*, 2003, and others) and it corresponds to the effects of centrifugal acceleration.

System drainage is illustrated by Figure 3.11. At 12:00 the entire marsh is submerged starting with a bulge of water of 1.25m focused in the southwest part of the basin (Figure 3.11a). The elevation decreases outward to 1.19m indicating radial drainage toward the basin's eastern perimeter. At 12:20 (Figure 3.11b) the two highest levees along the first and third bends of Groves Creek reemerge. The water elevation decreased 0.15m in 20 minutes, and the free surface elevations range from 1.11m in the marsh interior to 1.02m in the north and along the eastern marsh edge. The distance between the minimum and maximum elevations is 500m yielding a slope of 1.8×10^{-4} toward the east capable of forcing a strong flow over the eastern marsh edge. At 12:40 all levees along Groves Creek become emergent (Figure 3.11c), and the maximum elevation is 0.99m in the marsh interior and 0.87m in the north and eastern marsh edges, yielding an increased maximum slope of 2.4×10^{-4} toward the east and increased flow over the marsh edge. At 13:00 the elevation decreases from 0.85m in the marsh interior to 0.67m in the subtidal channel and high intertidal creeks. The eastward slope between the marsh interior and the eastern marsh edge increases to 3.6×10^{-4}. At 13:20 24% of the marsh is subaerial, including levees, high areas of marsh platform, and intertidal creeks. The water surface elevation is 0.72m across the western low marsh and in the marsh interior (Figure 3.11e) and < 0.67m in the subtidal channel, intertidal creeks, and to the west and east of the marsh interior. At this time the basin drains toward the west and east of the marsh interior through intertidal creeks and Groves Creek. At 13:40 53% of the marsh is subaerial and the free surface is < 0.67m (Figure 3.11f).

In summary, the free surface slopes, and hence the direction of inundation changes as the percentage of inundated area increases. Inundation occurs from the interior by flow from the subtidal to intertidal creeks during the first four hours when 46% of the basin is inundated. Between 9:00 and 9:40 inundation increases, the relief of the water surface increases to 0.08m and the resulting slope increases to 1.6×10^{-4}; also the eastern marsh edge, intertidal creeks and the subtidal channels are submerged at this time.

Two hours before high tide the entire marsh is submerged, the maximum difference in water surface elevation is 0.04m, maximum slope decreases to $8x10^{-5}$, and there is a change in the source of inundation going from the subtidal system to overmarsh flow toward the southwest. Similarly, ebb circulation changes with decreasing area of submergence. At the onset of drainage water leaves the salt marsh as a type of sheetflow outward from the southwest toward the basin perimeter, and it persists for the first 3 hours of ebb. An hour later the marsh topography becomes subaerial, and there is a maximum slope of $1.8x10^{-4}$ to the east indicating strong flow over the eastern marsh edge, followed by flow divergence in the marsh interior.

Another insightful way to assess basin scale flow is to evaluate the stage-velocity association at a station, in this case near the mouth of Groves Creek, Station 1 (Figure 3.12). The observations show that the peak flood and ebb velocities are comparable and have the characteristic asymmetry with ebb dominance (Myrick and Leopold, 1963; Boon, 1975; Pethick, 1980; French and Stoddart, 1992; Fagherazzi et al., 2008). In particular, peak flood velocity occurs at a higher stage than peak ebb. For example, on the spring tide the peak occurs at 1.15m and peak ebb occurs at 0.40m (Figure 3.12). Meanwhile velocity reaches 0.51m/s between a low tide elevation range of -1.68m - 0.63m. Subsequently, there is a surge in velocity reaching a peak of 0.93m/s at 1.15m (Figure 3.12). Currents then reverse and peak ebb velocity of -0.95m/s occurs at 0.7m.

The modeled stage-velocity relationship is comparable. Overall it shows flood velocity increases to 0.52m/s between a low tide range of -1.67m - 0.62m (Figure 3.12). This is followed by a surge in velocity reaching a peak of 0.69m/s at 0.93m. Currents reverse and peak ebb of -0.95m/s occurs at 0.35m. Velocities then decrease between peak and low tide and much more rapidly than during flood. Comparing the observed and simulated data shows that the model accurately predicts the overall stage-velocity relationship for Station 1.

Both the simulated and observed datasets show ebb velocities decreasing at a faster rate than during the same stages of flood. Moreover, the model captures the surge in flood velocity at stages when the topography is submerged and overmarsh flow is initiated (Boon, 1975; French and Stoddart, 1992). Both curves also show comparable asymmetry between peak flood and ebb velocity during higher stages. Specifically, peak flood is tied to the marsh platform elevation, as expected. Together these observations and analyses show that the modeled and observed flows at the mouth of the main channel are comparable, and the “upstream” overmarsh flow processes that give rise to the velocity-stage shape and distributions are also comparable, as well.

A third metric for assessing basin scale flow makes use of residence time, an estimate of the duration of a water parcel in the basin system. The tracer residence time (Rt) expressed through equation 3 and calculated from the observation data at Stations 1, 2, 3, 6, 7 and 8 ranges from 1.09 – 1.12 days with an average of 1.07 days (Table 3.5). The modeled Rt values are comparable, ranging from 1.02-1.12 days (Table 3.5). Therefore, we can expect that the innermost water parcels will be flushed from the system within about 1 day.

3.5.4 MACRO SCALE CIRCULATION

At two hours before high tide the mean depth of water on the marsh platform is 0.58m. The mean velocity over the platform and eastern marsh edge is 0.02m/s and 0.08m/s, respectively (Figure 3.13a). The average flow vectors along the eastern marsh edge and in the north (Figure 3.13a coordinates 4.980, 3.5372) indicate inundation predominantly from the basin edges as opposed to the channel network. However, in the southern marsh interior centered at approximately (4.977, 3.5366) there is divergent flow toward the west and east along the southern boundary (Figure 3.13a). Also, there is clockwise flow centered at 4.981, 3.5368 over the marsh interior with an average speed of 0.05m/s; decreasing to 0.03m/s along the central marsh interior where east - west convergence occurs. Hence, during flood and over the relatively short distances associated with this basin we find that overmarsh circulation concomitantly includes convergence and divergence in the marsh interior, and primarily convergence from the basin perimeter.

Figure 3.13b sheds light on local flow two hours after high tide. The mean velocity over the marsh platform and eastern marsh edge is 0.04m/s and 0.11m/s, respectively, and both show three circulation patterns during ebb. First, there is counterclockwise flow (Figure 3.13b) centered at (4.981, 3.537) that extends from the southwest across the marsh interior at 0.08m/s (Figure 3.13b). Second, there is flow divergence from the marsh interior toward the west and east of the counterclockwise flow path. Third, there is flow toward the basin exterior north of the marsh platform (4.980, 3.5374), and over the eastern marsh edge. Hence, the flows during ebb show similar complexity as with flood, with a range of flow directions over a relatively short time interval.

In summary, during flood, three distinct circulation patterns occur simultaneously. First, there is inundation toward the southwest from the basin exterior. Second, there is clockwise flow over the marsh interior. Third, there is flow divergence toward the east and west along the southern extremities of the basin, and flow convergence in the marsh interior. Ebb circulation differs from flood in that ebb velocities are stronger relative to flood. Also, flow across the marsh interior is counterclockwise, and there is flow divergence to the east and west of the marsh interior.

3.5.5 MESO SCALE CIRCULATION

The meso scale results from transects 1a and 1b are presented as a water balance across each. These two transects were used because basin scale analyses revealed that there are two sources of water to the marsh interior; Groves Creek and the Wilmington River. The net volume of water that crosses transect 1a during flood is -3,452m^3 while for ebb it is +8,498m^3 (Table 3.6). Therefore, the difference between flood and ebb is +5,046m^3 over the full tidal cycle. Flood and ebb volumes across transect 1b are -3,700m^3 and +11,720m^3, respectively, with net volume of +8,020m^3. Both have positive net transport over the full tidal cycle indicating net flow away from the marsh interior.

Meanwhile, information gleaned from the net flows across transects 2a-2d are taken to represent flows within the marsh interior. Water volumes range from -2,459m^3 to -16,080m^3 for flood and +4,280m^3 to +28,428m^3 for ebb (Table 3.6). The differences between flood and ebb range from +1,741m^3 to +22,407m^3. All four transects have positive net transport over the full tidal cycle and collectively they indicate net counterclockwise or rotational flow within the marsh interior.

3.5.6 GROVES CREEK CIRCULATION – MICRO SCALE

At the micro scale we assess the current velocity time series for two intertidal creeks with a dogleg structure (Figure 3.3) to illustrate the local control of topography on overmarsh circulation. Creek 1 is inundated from the south at 3 hours into the flood cycle

(Figure 3.14a). Currents are confined to the channel and both locations reach a peak flood velocity of 0.09m/s. At approximately 0.67hrs later the water level is 0.53m and currents in both sections flow from the northwest, and velocity is 0.06m/s lower. The consistent southeastward flow through both sections of the dog-leg indicates the onset of overmarsh flow which continues at 0.02m/s until high tide (1.45m).

At the start of ebb the water level is 1.44m and the depth averaged currents in both the north/south and east/west sections are from the west at 0.04m/s (Figure 3.14a). One hour into ebb the water level declines to 1.28m and overmarsh currents reverse reaching a peak of 0.26m/s. Four hours after high tide the water level is at 0.45m and the creek banks become subaerial. At this time the in-channel currents reverse and flow from the north-northeast at 0.09m/s.

Creek 2 is inundated 2hrs into flood when the water level is -0.42m and currents are confined by the banks. At the same time there is convergence from the subtidal channel and eastern marsh interior (Figure 3.14b). At 0.33hrs later in-channel currents reverse and flow from the north occurs when the water level reaches -0.14m, and develops a peak velocity of 0.20m/s. Four hours into flood the topography is submerged and at that time overmarsh currents flow from the northeast at 0.03m/s until high tide (Figure 3.14b).

With the onset of ebb, overmarsh flow is from the southeast at 0.04m/s (Figure 3.14b). The topography becomes subaerial three hours into ebb at a water level of 0.69m. At this time in-channel currents reverse and reach a peak velocity of 0.23m/s. Four hours into ebb there is another current reversal at -0.27m, and flow is from the northwest at 0.07m/s.

In summary, Creek 1 activates three hours into the flood tide and creek banks are submerged less than an hour later. During ebb this creek is active for 2 hours. Creek 2 has a relatively lower bed elevation than Creek 1, activates at two hours into flood, and is submerged 2 hours longer, but it reactivates during the last 3 hours of the ebb tide. The velocity and direction of in-channel and overmarsh currents supports the reported observations for meso, macro, and basin scale results by collectively showing clockwise and counterclockwise patterns of overmarsh flow during flood and ebb, respectively.

3.6 DISCUSSION

We define complexity in overmarsh circulation as the variation in current direction and magnitude over relatively short time intervals of about 10 minutes. Flow complexity has been a common theme in salt marsh flow studies (Eiser and Kjerfve, 1986; Kjerfve, 1991; Christiansen et al., 2000; Temmerman et al., 2005; Torres and Styles, 2007; Mariotti and Fagherazzi, 2011); yet no studies have characterized this complexity for a comparably large section of salt marsh as conducted here, and none have addressed its origin. Here we found that the source for the onset of complex overmarsh circulation is the submergence and emergence of the very subtle salt marsh platform relief. For example, emergent topography can completely shut off some flow pathways while initiating new ones.

The spatial variability in dye concentration from the model largely replicates field observations as indicated by the strongly positive ME values. Results were somewhat less robust at Stations 3, 5 and 8. We propose that the Station 3 (ME = 0.36) discordance arose because the simulations produced a large initial spike in concentration that was not detected in the hourly observation data. Given equation 2 this translates directly to a poor model performance. The lower ME for Station 5 likely is a product of the phase offset between simulation and observation over the full two hour record for these grad samples. However, phase shifts are also apparent with all comparisons of simulated and observed but the shift declines over the 5-day interval. Therefore, given the short record of comparison and the exclusion of the latter data for comparison the Station 5 ME value reflects substantial discordance. At Station 8, the only station in the intertidal zone and the one most distant from the injection line has a weak performance that is also attributable to phasing. In this case the observed initial spike increase in concentration occurs earlier than the simulated. This may have arisen due to the longer and hydrodynamically rougher intertidal zone distance that water must traverse to reach the station. Despite these limited shortcomings, the dye response at all stations was well represented by the model, and provides reliable background flow information on system wide inundation and drainage.

Residence time, Rt gives an estimate of the duration of a water parcel in the basin system, and the simulation results show that Rt is about 1.11 days. This residence time is 28% greater than the basin flushing time, Tf, most likely because of the spatial and temporal variability of underlying physical processes controlling overmarsh circulation.. Additionally, Blanton et al., (2010) measured concentrations from a site proximal to Station 2, and they estimated Rt of 1.62 days. Therefore, our values are about 0.5 days shorter, and they further constrain plausible estimates of Rt in salt marsh systems.

Dye circulation patterns reveal that the sheet flow over the largely flat salt marsh landscape is not homogeneous, but has strong temporal and spatial variability that arise from simultaneous convergence, divergence and rotation in the marsh interior during flood. This type of complexity in overmarsh circulation is important in salt marshes because it strongly influences the distribution of suspended and dissolved nutrients, larvae distribution, and contaminant dispersal (Valiela et al., 1978; Kneib, 1984; Blanton et al., 2010). For instance, the flow fields in Figures 3.13a and 3.13b illustrate the source of the dye front that occurs 2hrs before high tide. The dye circulation also shows that there is considerable drainage directly over the eastern marsh edge during ebb. Hence, a parcel of inundation water does not necessarily follow the same track between flood and ebb (e.g., French and Stoddart, 1992). The dye response also highlights spatial variability in flow complexity throughout the Groves Creek system. For instance, stations located in the ebb direction of the injection have single peaks coincident with low tide, whereas all other stations have double peaks, one on the ebb and one on the flood limbs of tidal stage. A similar response in salinity was reported by Warner et al. (2006) who attributed the double peak to confluence effect at tributary channels (Warner et al., 2006). On the other hand Station 8 has a double peak as well, but for entirely different reasons. The difference resides with the fact that Station 8 is intertidal zone. Here the double peak is a result of the intermittent drying of the creek bed with low tide and the movement of the dye tracer back and forth over the site with each tidal cycle. Taken together, the dye response and underlying flow conditions highlight overmarsh flow complexity across relatively large distance and at a range of spatial scales.

Analyses at the four spatial scales of flow highlight patterns of overmarsh current direction, and two of the four highlight both direction and magnitude. At the basin scale we saw that the direction of inundation and drainage changes over short time intervals and this, in turn, is related to the degree that the marsh remains subaerial. At the macro scale, we show flow direction and magnitude for intermediate tidal stages. The data analyses clearly show that there is simultaneous convergence and divergence, as well as rotational flow and substantial flow over the marsh edge.

At the meso scale flows across transect 1 indicate that net transport is away from the marsh interior, and ebb dominant. The variability between 1a and 1b may be set by the average transect elevation with 1a at 0.62m ±0.09m, and 1b at 0.56m ±0.15m. Also, these transects essentially represent water exchange between the marsh interior and Groves Creek, and the marsh interior and the Wilmington River, 1a and 1b, respectively. Therefore, we contend that the net fluxes reflect a type of circulation where water inundates the marsh through the channel network but principally drains over the marsh edge. This is consistent with the tracer and macro scale flow results. We also show positive net flow for transects 2a-2d and this is taken with their respective spatial arrangement to indicate counterclockwise rotation during part of the tidal cycle (Figure 3.3, Table 3.6).

At the micro scale we show that intertidal creeks are active only during a small portion of the tidal cycle, and for about one hour longer during ebb tide than flood. The time that intertidal creeks convey flow is of course dependant on bed elevation, and these vary substantially. The intermittent control of topography on local in channel currents together with shifts in the larger scale barotropic pressure gradient give rise to additional current reversals during flood and ebb (e.g. Torres and Styles, 2007; Fagherazzi et al., 2008). Clearly, topography is an important control on overmarsh circulation. In a recent study, Blanton et al. (2010) conducted numerical simulations over the same study site, Groves Creek, but they used a bathymetric domain derived from a coarse lidar dataset.

This means that their study did not include the effects of relatively small scale variations in topography or geomorphic structure. Overall, their current simulation results were fairly robust but their simulated dye plume failed to match the field observations in that the dye did not reach the southern basin edge. Also, the dye was retained in the marsh interior for a prolonged interval. Here we improve on this effort by resolving the subtle geomorphic structure and evaluating its effects on flow. Overall, the dye reached deeper into the system but our estimates for tracer residence time were much shorter than *Blanton et al*. Our findings lead us to question the level of topographic detail needed to adequately replicate overmarsh flow processes. Finally, future work is needed to address the combined role of topography and vegetation drag on the temporal and spatial variability in overmarsh circulation and morphodynamics.

3.7 CONCLUSIONS

The simulation results from Delft3D are robust and in most cases produced a model efficiency greater than 0.90. This is primarily due to the extremely high quality salt marsh DEM and the range and quality of field data for calibration and validation. Numerical assessments of dye transport and circulation reveal strong complexity in overmarsh currents with the temporal evolution of inundation, and drainage at water levels within 0.2m of the mean platform elevation. Moreover, over the full five-day simulation interval we found that 53% of the dye mass exited the system at the eastern marsh edge, while 32% exited via the mouth of Groves Creek. At the basin scale (1,000m) the marsh platform is initially inundated from the marsh interior but as the tide continues to rise flooding occurs from the basin edges, and this gives rise to the onset of overmarsh flow. At the macro scale (100m) flow paths are highly variable with strong differences between ebb and flood circulation. At the meso scale (10m) we detected rotational flow over the marsh interior and across channels. At the micro scale (1m) local in-channel currents are intermittently controlled by the channel banks but at higher tide stages the larger scale barotropic pressure gradient causes the currents to flow across tidal creek networks.

Table 3.1 List of instruments at the eight observation stations

Station	Instrument Type
1	ADCP, SBE16 CTD, Wetlabs FLRHSB
2	ADCP, Wetlabs FLRHSB
3	ADCP, SBE16 CTD, Wetlabs FLRHSB, grab samples
4	ADCP
5	ADCP, grab samples
6	ADCP, Wetlabs FLRHSB
7	ISCO sampler, SBE16 CTD
8	SBE16 CTD, Wetlabs FLRHSB

Table 3.2 A list of literature sources for Manning's roughness coefficients for vegetated and unvegetated marsh. Citations with an asterisk were final selections for the study.

Author	**Study Site Type**	**Manning's n**
Shih and Rahi (1982)	Subtropical marsh	0.16 – 0.55
Kierfve et al., (1991)	Vegetated marsh	0.20 – 0.30
Leopold et al., (1993)	Marsh channel	0.28 – 0.063
Tsihrinitzis and Madiedo (2000)	Vegetated marsh	0.02 – 1.00
Wilson and Horritt (2002)	Submerged vegetation	0.05
	Unsubmerged vegetation	0.23
French (2003)	Subtidal channel	*0.017
	Intertidal channel	0.022
	Tidal flat	0.035
	Marsh platform	*0.10
Lawrence et al., (2004)	Marsh platform	0.07
	Moderately rough channel	0.03
Lesser et al., (2004)	Uniform marsh	0.028
Temmerman (2005)	Marsh bottom roughness	0.006
Loder et al., (2009)	Sea bed	0.02
	Marsh creek bed	0.02
	Platform with tall grass	0.035
Cea and French (2012)	Subtidal channel	0.02
	Low intertidal marsh	0.03
	High intertidal marsh	0.05

Table 3.3 Model efficiency values for water level, velocity and dye tracer concentration.

	Water Level ME	**Velocity ME**	**Dye Tracer ME**
Station 1	0.99	0.92	0.83
Station 2	0.99	0.92	0.82
Station 3	0.99	0.82	0.36
Station 3 grab	n/a	n/a	0.62
Station 4	0.99	0.86	n/a
Station 5	0.92	0.94	0.35
Station 6	0.99	0.85	0.58
Station 7	n/a	n/a	0.76
Station 8	n/a	n/a	0.30

Table 3.4 Observed and simulated peak concentrations in ppb, record mean and standard deviation for Stations 1-8. Asterisks denote values calculated for a single tidal cycle.

	Station 1	Station 2	Station 3	Station 3 grab	Station 5 grab	Station 6	Station 7	Station 8
Peak 1 OBS	45	103	13	588	1038	574	170	79
Peak 1 SIM	37	76	150	489	674	495	155	50
Peak 2 OBS	28	52	130	n/a	n/a	119	89	57
Peak 2 SIM	23	41	63	43	55	90	125	90
Peak 3 OBS	17	30	65	n/a	n/a	55	54	34
Peak 3 SIM	16	25	32	23	33	48	68	89
Peak 4 OBS	11	18	40	n/a	n/a	34	38	17
Peak 4 SIM	10	17	20	14	20	40	40	42
Peak 5 OBS	7	11	21	n/a	n/a	18	21	12
Peak 5 SIM	6	10	13	8	13	25	23	19
Peak 6 OBS	4	6	14	n/a	n/a	12	16	5
Peak 6 SIM	4	6	8	6	8	12	11	16
Peak 7 OBS	n/a	n/a	8	n/a	n/a	6	8	n/a
Peak 7 SIM	n/a	n/a	5	4	4	6	9	n/a
Record Mean OBS	5	15	22	85*	168*	27	41	13
Record Mean SIM	5	13	12	124*	183*	27	28	14
STDV OBS	10	25	28	165*	304*	45	37	21
STDV SIM	9	19	16	145*	196*	46	30	17

Table 3.5 Tracer residence time (Rt) in days for Stations 1, 2, 3, 3 grab, 5 grab, 6, 7 and 8.

	St. 1	**St. 2**	**St. 3**	**St. 3g**	**St. 5g**	**St. 6**	**St. 7**	**St. 8**
Observed	1.12	1.09	0.97	n/a	n/a	1.04	1.09	1.09
Simulated	1.18	1.2	1.07	1.14	1.14	1.08	1.02	1.12

Table 3.6 Net volume transport resulting from the meso scale analysis from transects 1a and 1b, and 2a, 2b, 2c and 2d.

Transect	**Net Flood m^3**	**Net Ebb m^3**	**Net Volume m^3**
1a	-3452	+8498	+5,046
1b	-3700	+11720	+8,020
2a	-2539	+4280	+1,741
2b	-16080	+28428	+12,348
2c	-8146	+20666	+12,520
2d	-2459	+24866	+22,407

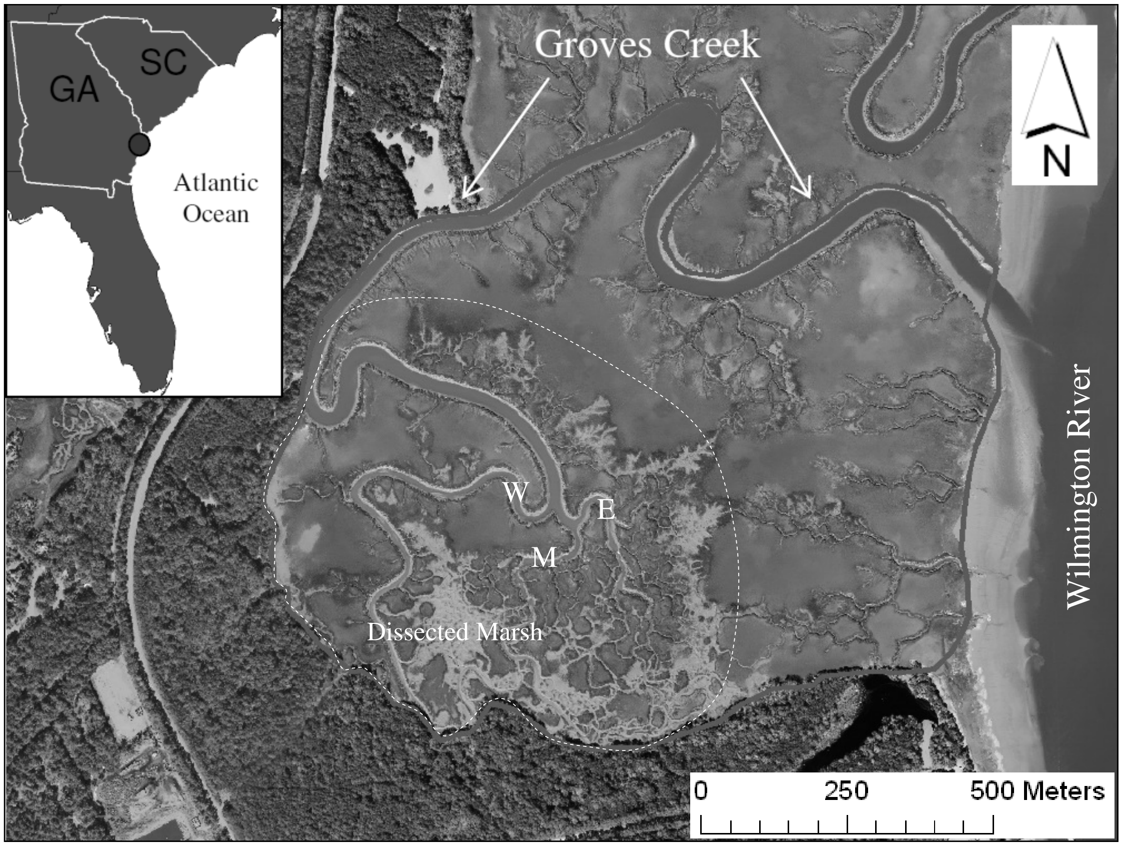

Figure 3.1 Groves Creek is a semi-enclosed creek-marsh system located approximately 20 km south of Savannah GA, USA. The shading of the imagery reflects variations in vegetation density. Specifically, lighter shades in the dissected marsh and along creek heads are associated with unvegetated mud. Darker shades along levees and creek banks reflect areas of dense vegetation. Medium shades are associated with the vegetated marsh platform. The lighter shading of the marsh platform in the northeast is associated with an area of sparsely vegetated high marsh. Groves Creek has three subtidal branches labeled E, W and M for East, West and Middle, respectively. The white dashed line outlines the "marsh interior". Within the marsh interior is the "dissected marsh" which is bounded by the West and East subtidal branches.

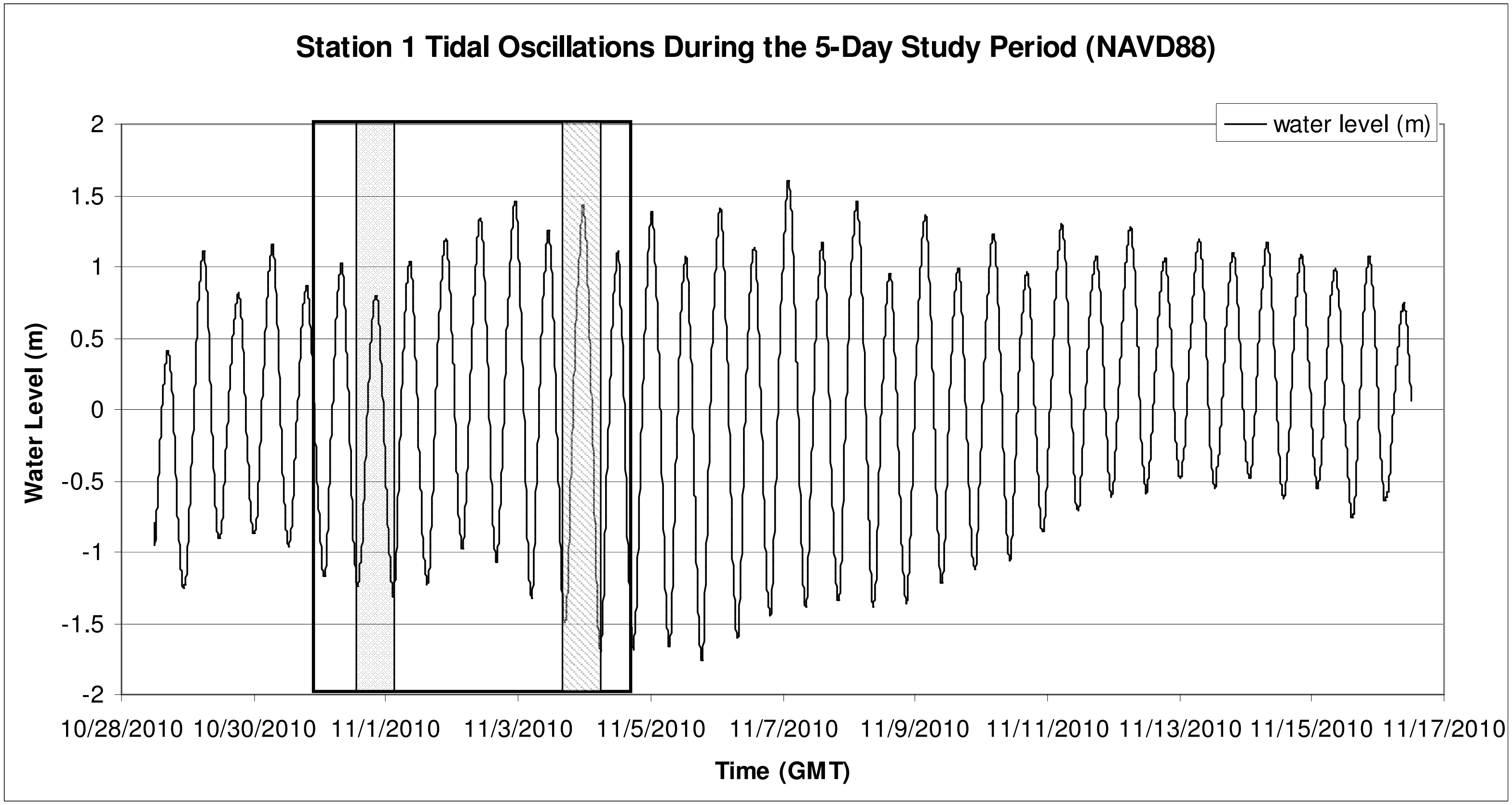

Figure 3.2 Tidal oscillations for a two week period showing the transition from neap to spring tide. The black box marks the 5-day study period. The smallest and largest tidal ranges during the study period are highlighted with gray and striped boxes, respectively, and are referred to as "neap" and "spring". All water levels are referenced to NAVD88.

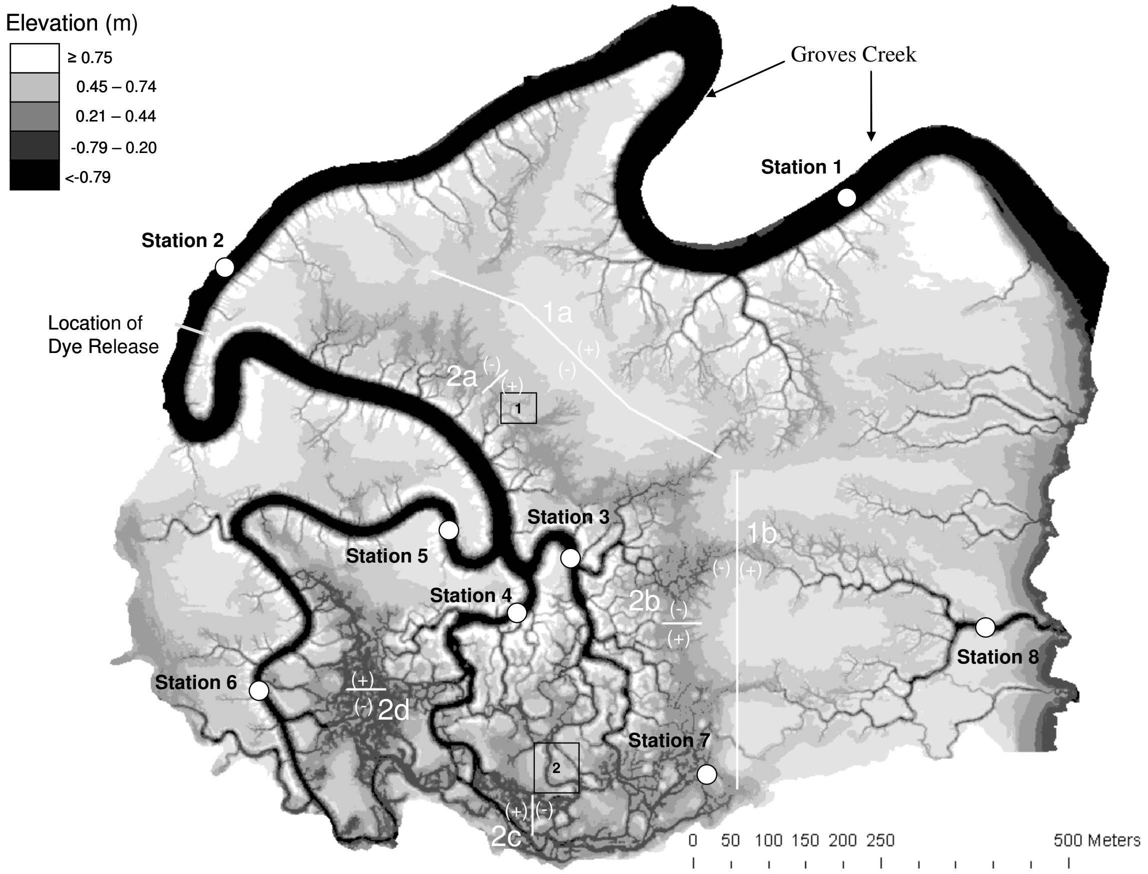

Figure 3.3 The high resolution GPS DEM is shown. White to black on the color bar represents the elevation range associated with levee, marsh platform, low marsh, intertidal creeks, and subtidal channel, respectively. White circles mark the locations of pressure sensors, ADCPs, fluorometers, and grab samples. The small gray line south of Station 2 marks the location of the dye release. The white lines throughout the marsh interior represent the six transects used to estimate meso scale flux. Transects lengths are 500m for 1a and 1b and 50m for 2a, 2b, 2c, and 2d. The + and - illustrate the flow convention for the meso scale analysis. For transects 1a and 1b, positive flows represent net transport away from the marsh interior. For transects 2a-2d, positive flows represent net counterclockwise flow within the marsh interior. Finally, the locations of dogleg creeks 1 and 2 selected for the micro scale assessment are highlighted with black boxes.

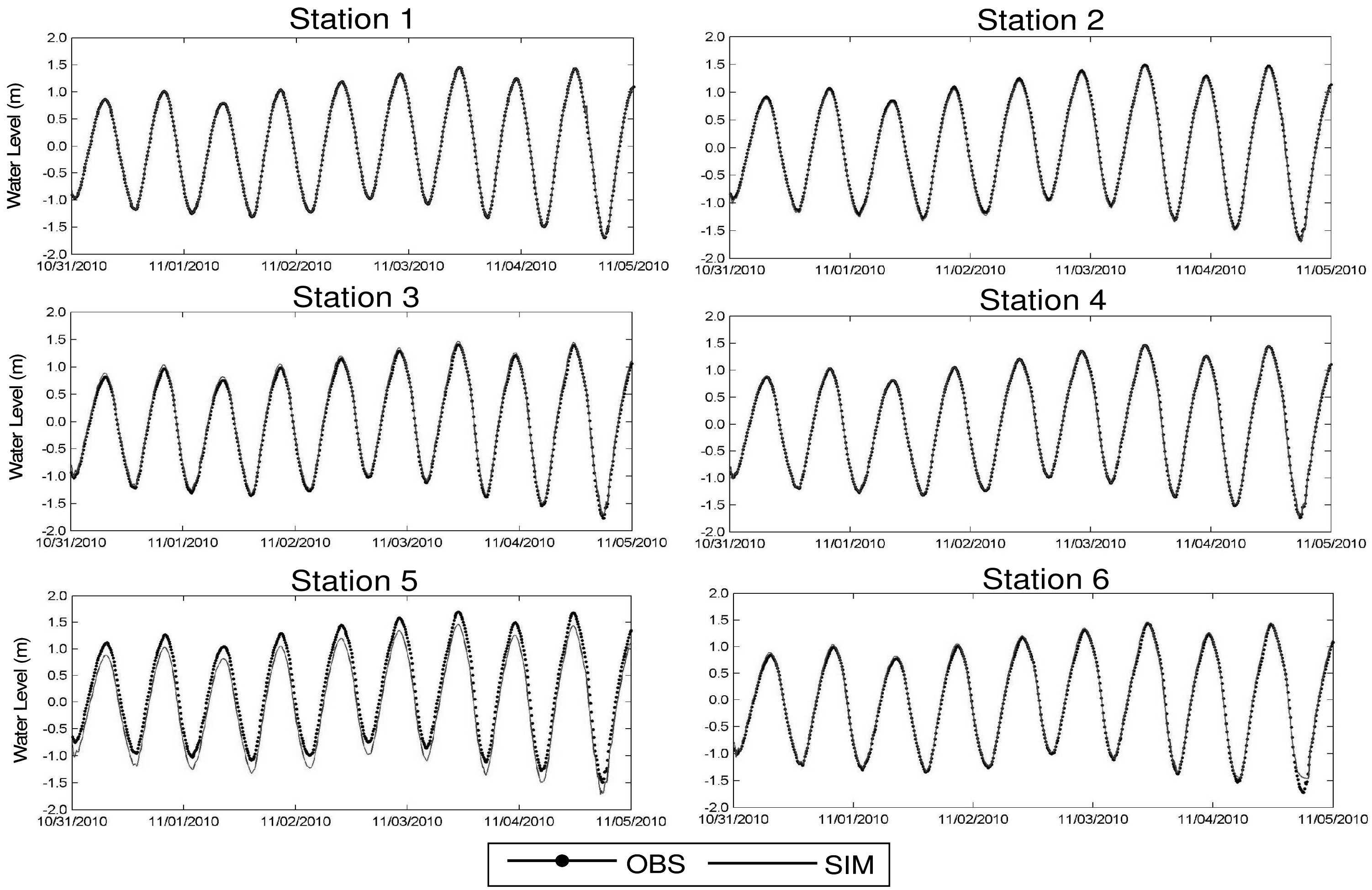

Figure 3.4 The calibrated water level timeseries at Stations 1, 2, 3, 4, 5, and 6. Lines with and without symbols represent observed and simulated water levels, respectively.

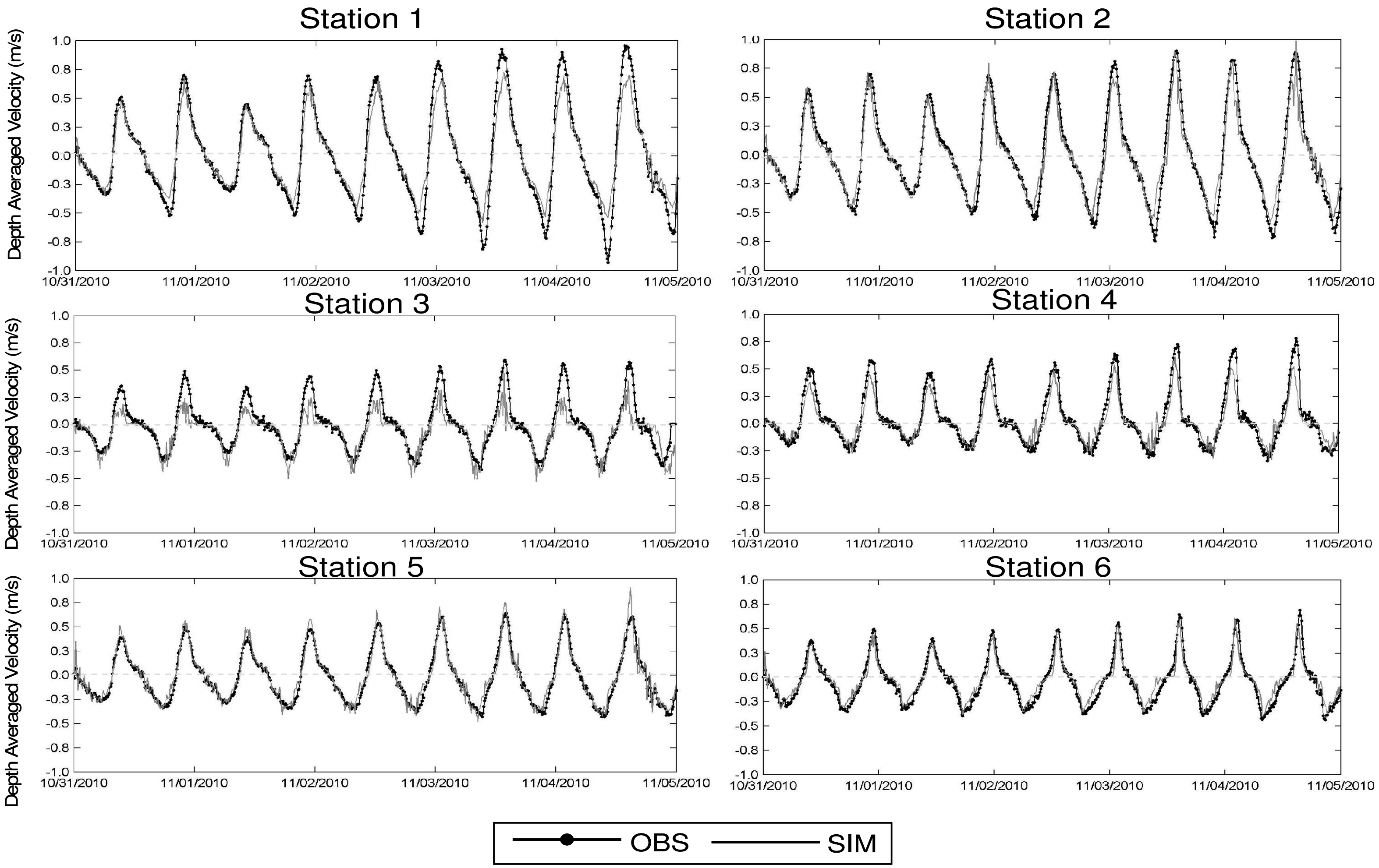

Figure 3.5 The calibrated depth averaged velocity time series at Stations 1, 2, 3, 4, 5 and 6. Lines with and without symbols represent observed and simulated velocities, respectively. The dashed gray horizontal line marks zero velocity. Flood and ebb velocities are negative and positive, respectively.

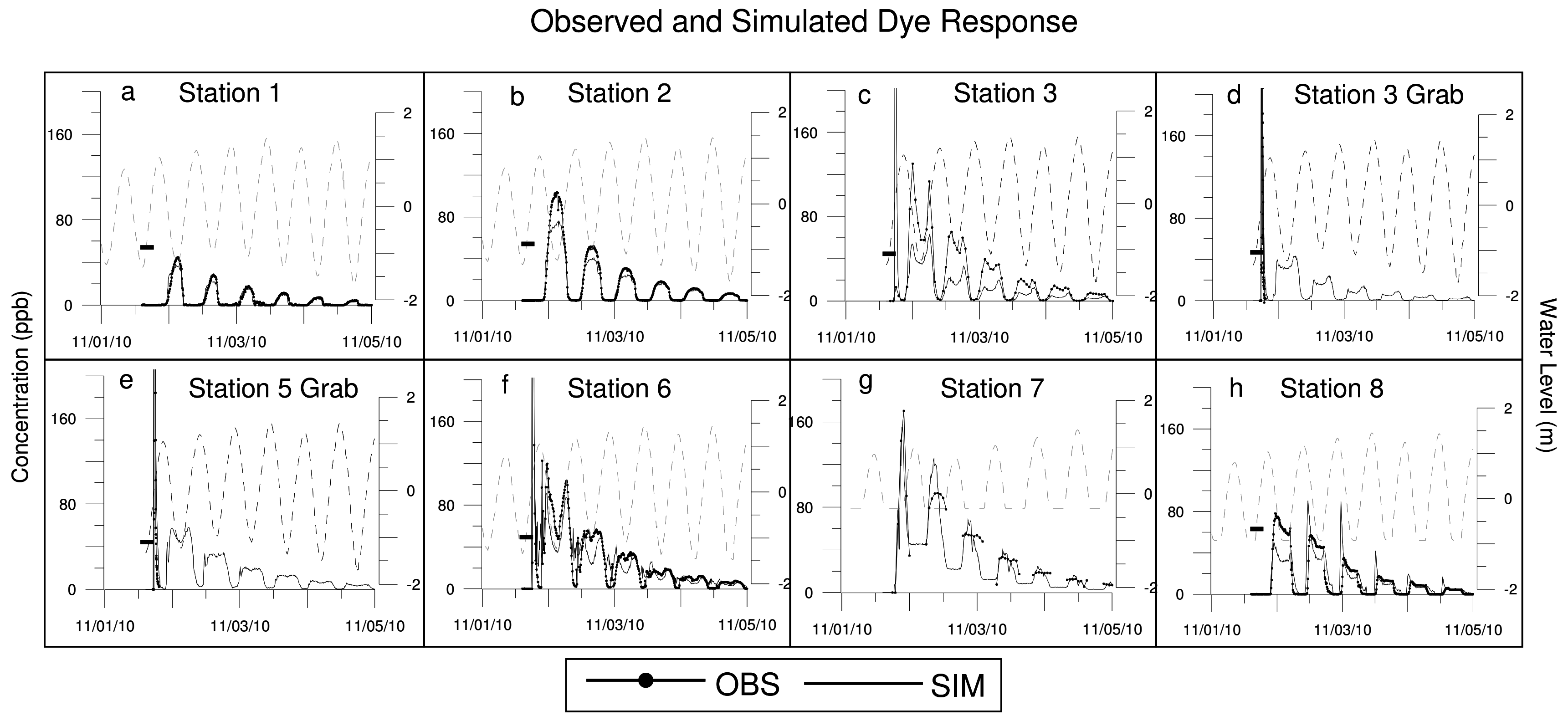

Figure 3.6 Time series showing the observed and simulated dye tracer response at Stations 1, 2, 3, 3 grab, 5 grab, 6, 7 and 8. Lines with and without symbols represent the observed and modeled data, respectively. The dashed gray line represents the water level time series for each station. A black tick mark highlights the timing of the dye release. All y-axis have a consistent scale and concentrations greater than 200 ppb are out of the plot boundary.

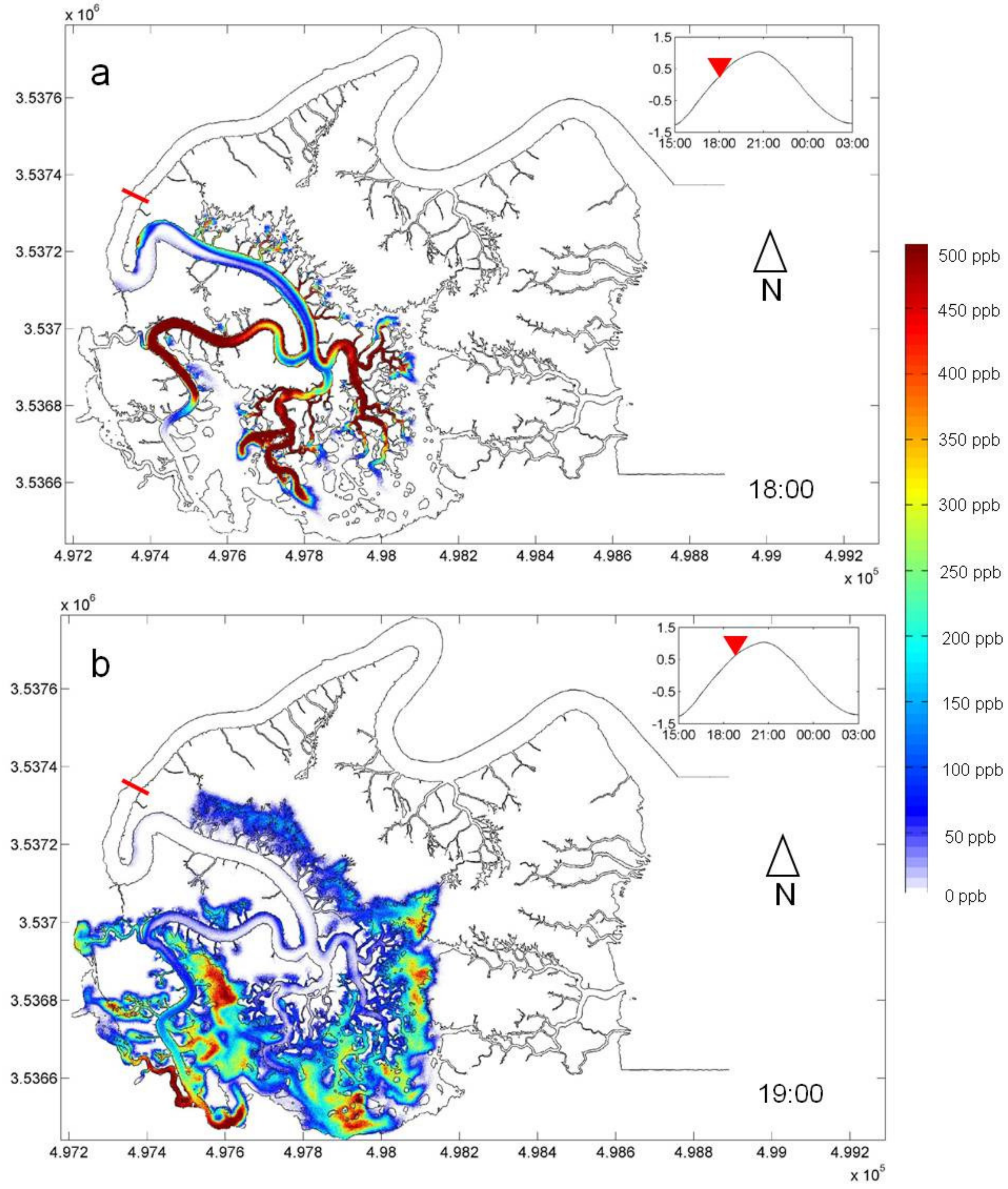

Figure 3.7 Images of the simulated dye tracer plume (a) at 18:00 GMT or three hours before high tide and (b) at 19:00 GMT or two hours before high tide. Warm and cool colors represent high and low dye concentrations, respectively. Concentrations are superimposed onto the -0.79m - 0.20m intertidal creek contour. The red line marks the location of the dye release. Water levels over the tidal cycle are shown in the upper right corner and the red arrow coincides with the time of the dye map.

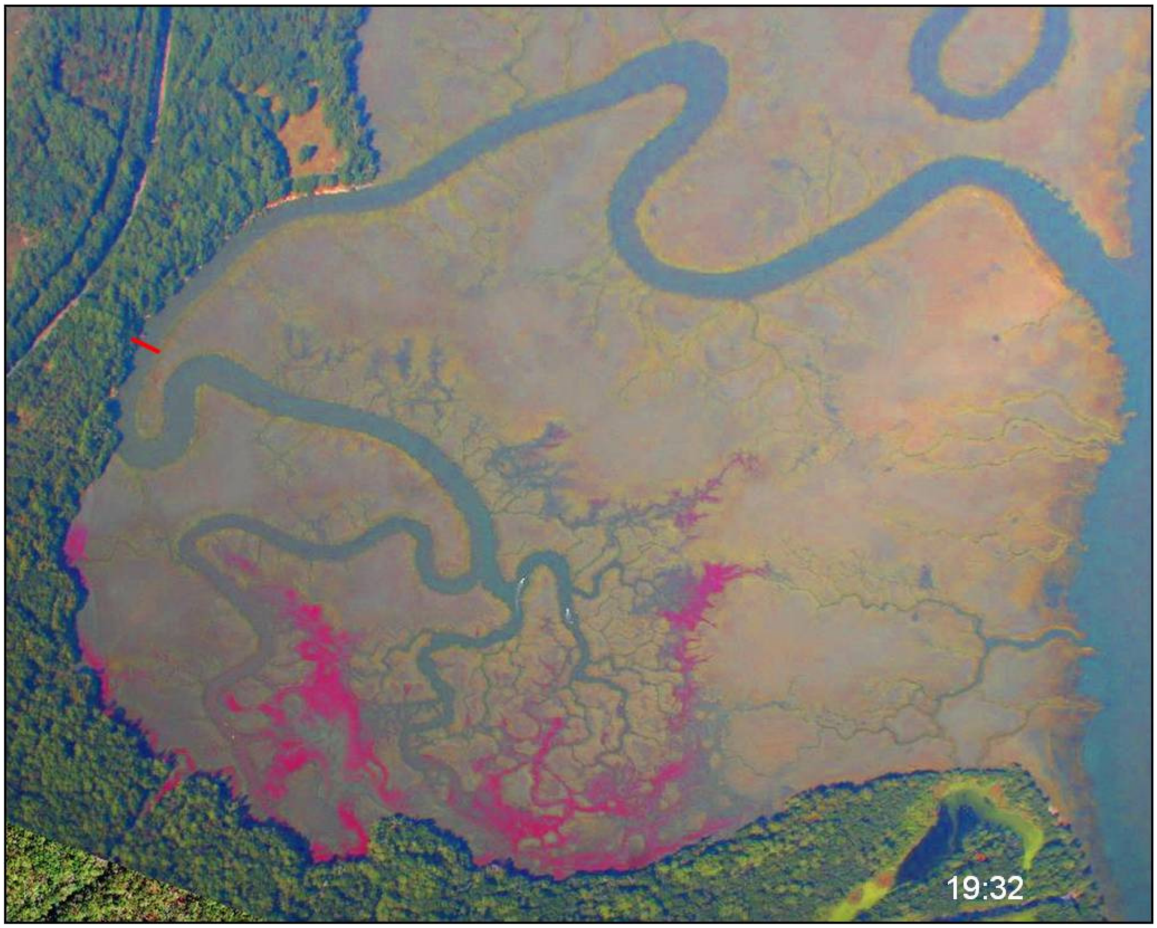

Figure 3.8 Ortho-rectified aerial photograph taken at 19:32 GMT during the field dye tracer experiment. Areas of bright and lighter shades of red represent high and low concentrations, respectively. The red line marks the location of the dye release.

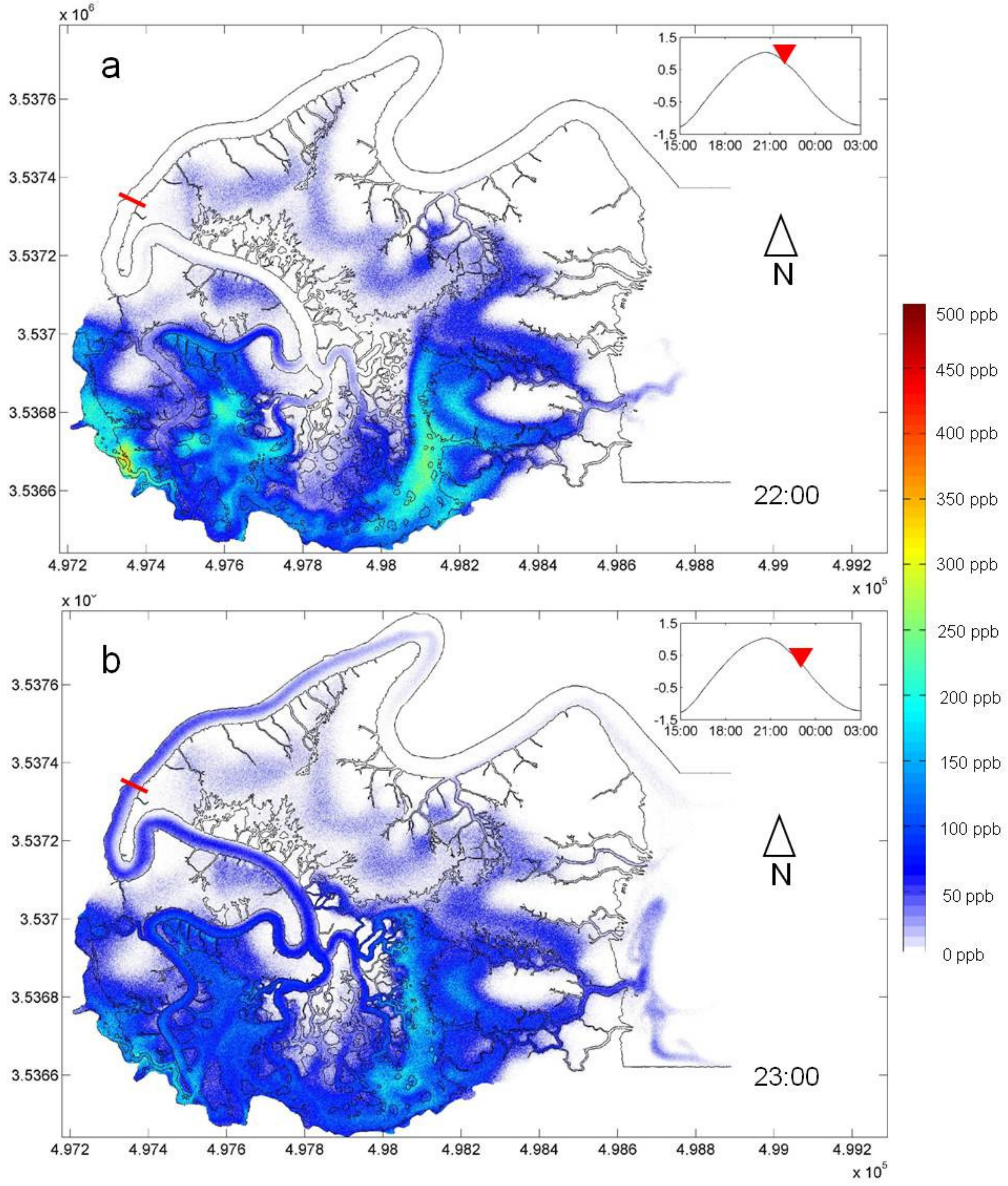

Figure 3.9 Images of the simulated dye tracer plume (a) at 22:00 GMT two hours after high tide and (b) at 23:00 GMT three hours after high tide. Warm and cool colors represent high and low dye concentrations, respectively. Concentrations are superimposed onto the -0.79m - 0.20m intertidal creek contour. The red line marks the location of the dye release. Water levels over the tidal cycle are shown in the upper right corner and the red arrow coincides with the time of the dye map.

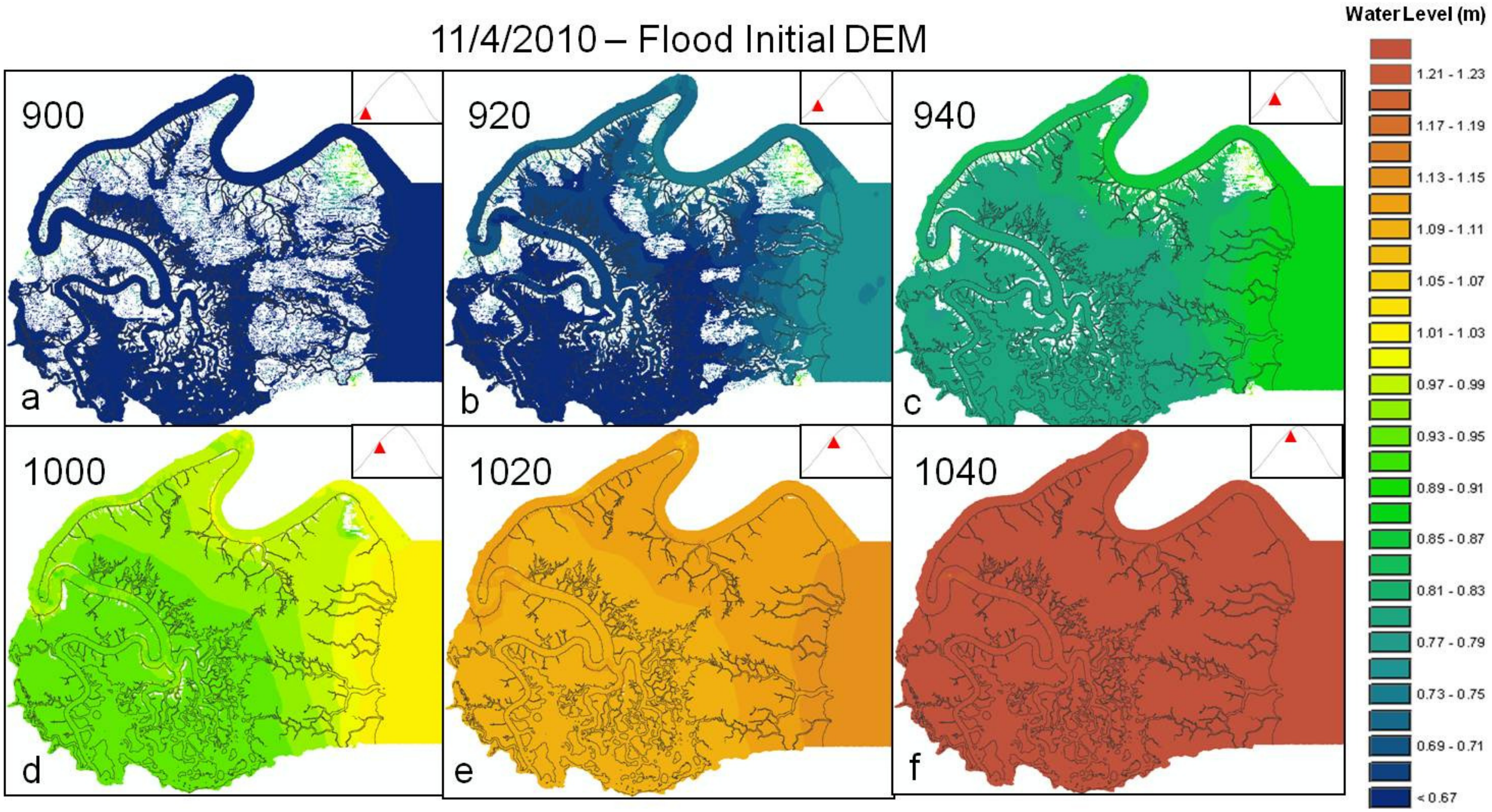

Figure 3.10 A series of maps showing the free surface elevation at 0.33hr intervals during the spring flood tide. Warm and cool colors represent high and low water surface elevation, respectively.

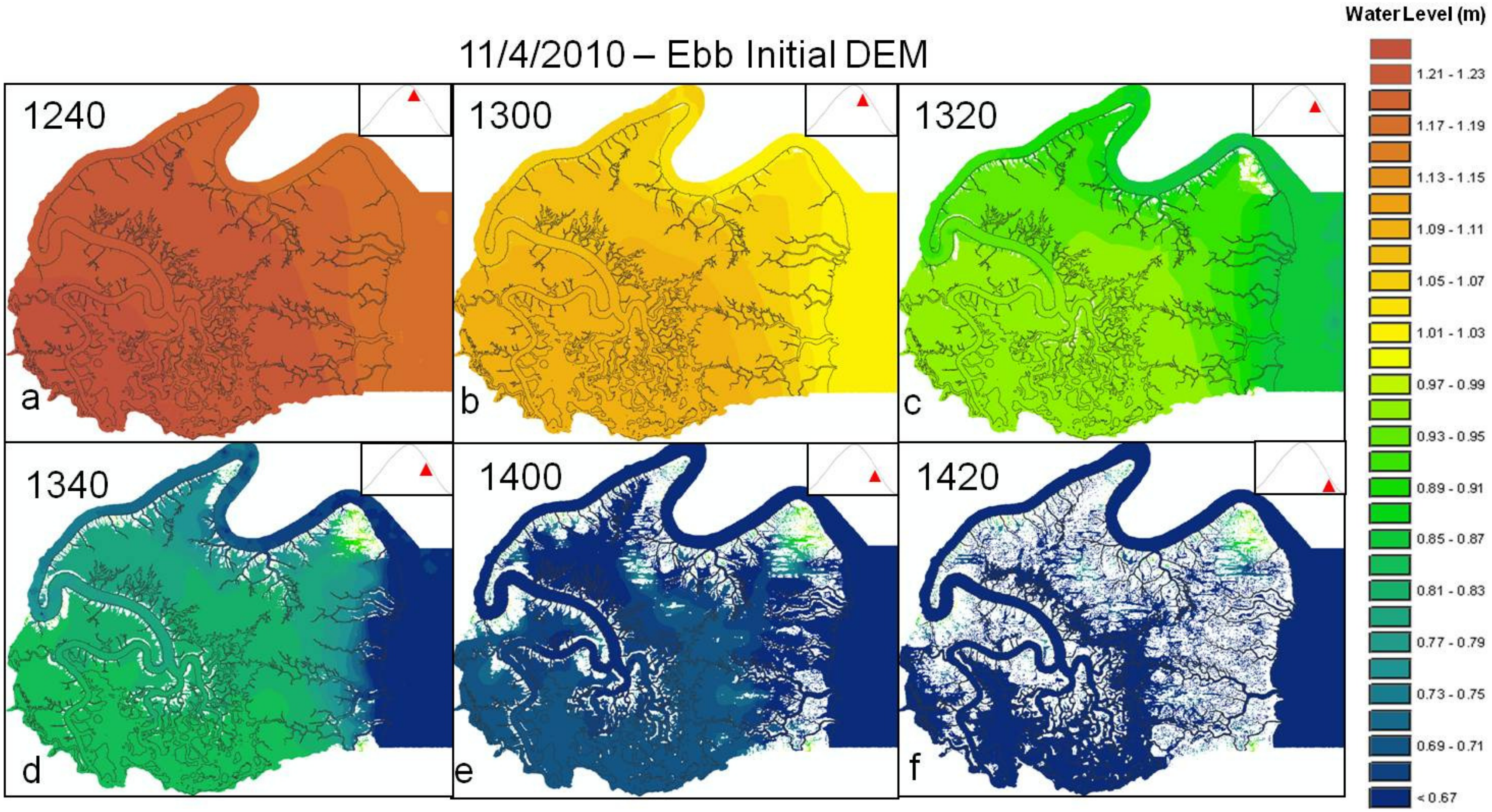

Figure 3.11 A series of maps showing the free surface elevation at 0.33hr intervals on the spring ebb tide. Warm and cool colors represent high and low water surface elevation, respectively.

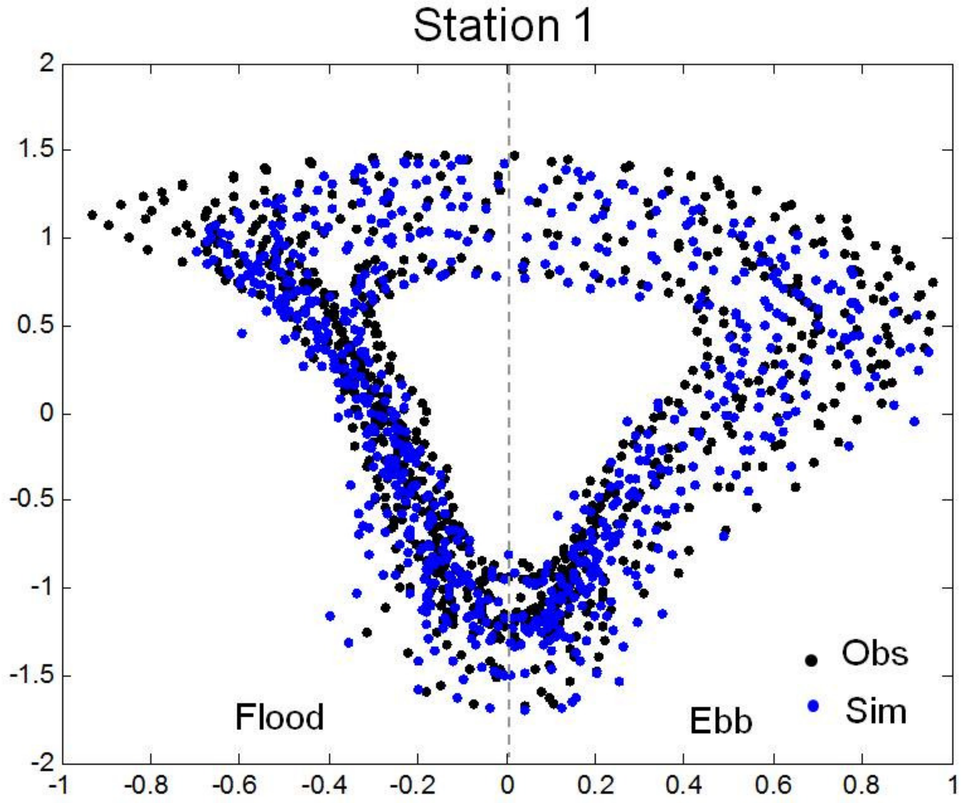

Figure 3.12 Station 1 velocity-stage relationship from observed and modeled data. The black and blue dots represent observed and simulated values, respectively. Flood values are negative.

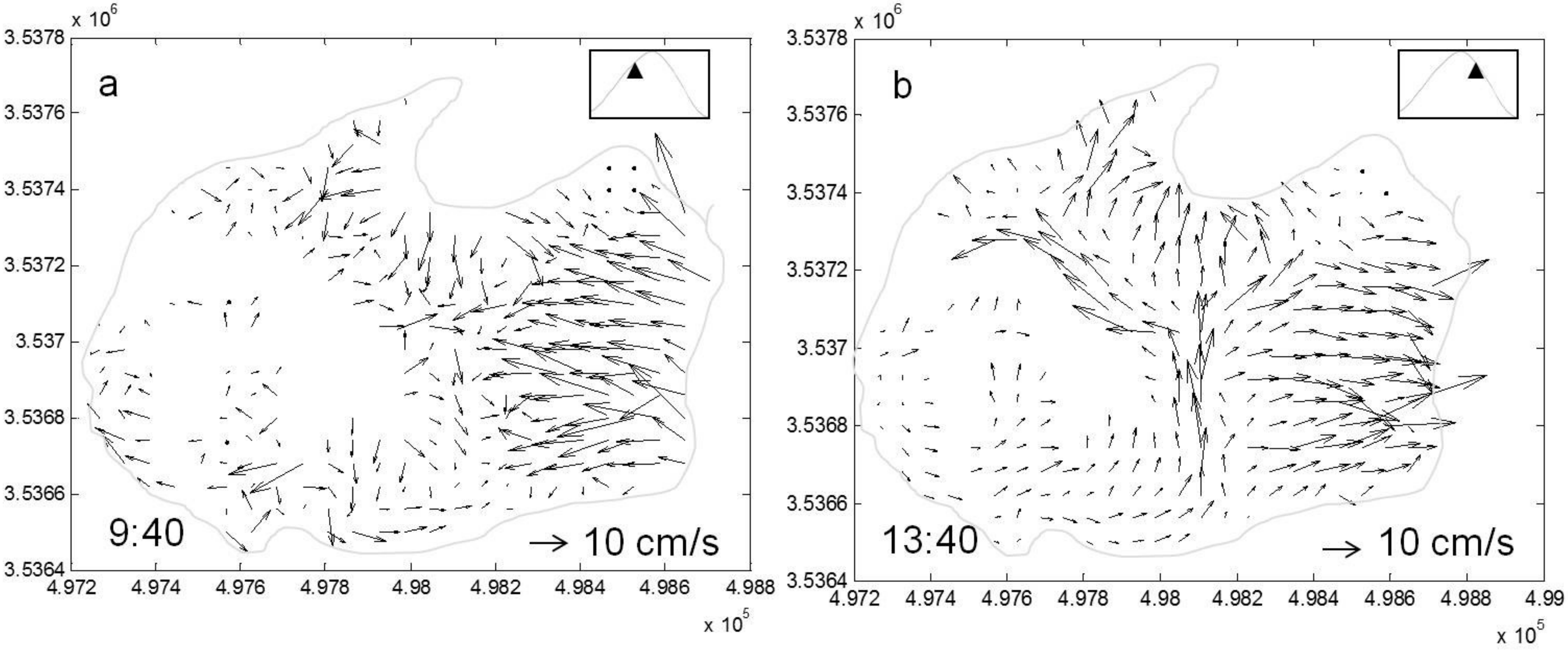

Figure 3.13 Flow vectors for the (a) flood and (b) ebb cycles of the spring tide. The vectors highlight clockwise and counterclockwise flow paths across the marsh interior during respective flood and ebb cycles.

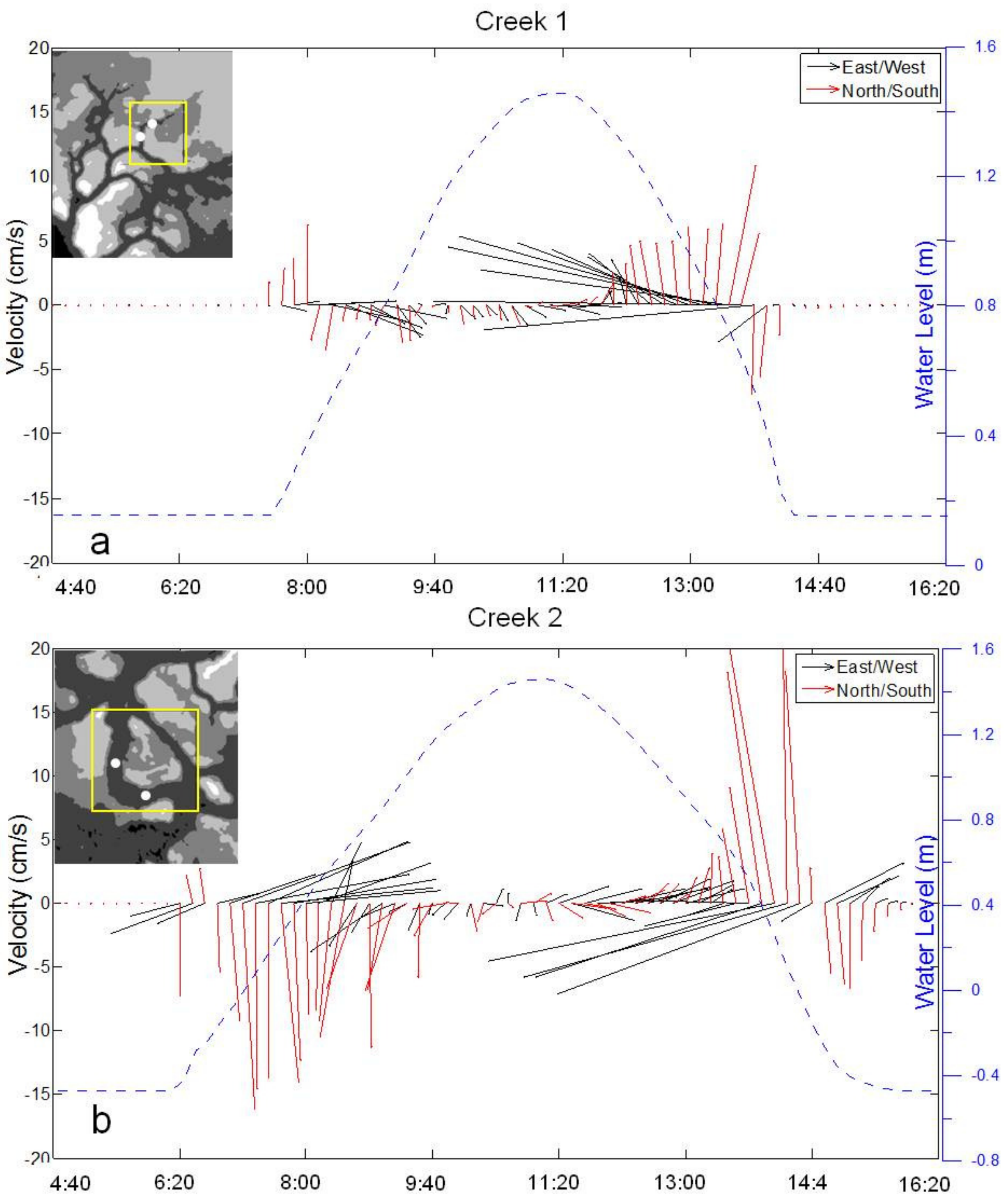

Figure 3.14 Velocity vector time series from dogleg creeks 1 and 2. Red and black vectors represent the north/south and east/west sections, respectively. An inset is provided to illustrate the topographic structure of each creek. White circles mark the east/west and north/south points in the doglegs. Water levels are superimposed as a dashed blue line.

CHAPTER 4

ON TOPOGRAPHY AND OVERMARSH CIRCULATION

4.1 ABSTRACT

We progressively smooth a high resolution, high precision salt marsh DEM to assess the effect of variable topography/bathymetry on simulations of overmarsh circulation. Field measurements of current velocity, water level and dye tracer concentrations at various stations provide information for model validation. Topographic smoothing progressively reduced the basin drainage density by 97%, and in the course of averaging removed small scale intertidal creeks and creek networks. Nevertheless, simulation results show nominal effects up to a 50m x 50m grid smoothing whereupon a system-wide change from ebb to flood dominance occurs. Assessments of dye tracer response indicate successively greater dispersal in the marsh interior during flood and higher concentration water exiting the system via a short-circuiting intertidal creek network, e.g., water parcels enter and exit the system along different flow paths. However, with a 50m x 50m smoothing the dye dispersal is less expansive, more dye retention occurs in the interior and lower concentration dye exits the short-circuiting creek. Dye retention times progressively decrease for the small scale smoothings and then increase for the 50m x 50m and greater smoothings. Consequently, tracer retention times appear to be set by the subtle geomorphic structure of the landscape, and the presence of short-circuiting conduits. Overall, DEM smoothing with a less than a 50m x 50m grid

average had a nominal effect on overmarsh circulation. Hence, smoothing out small scale intertidal creeks and creek networks reveals their minor role in overmarsh circulation, while excessive smoothing caused the system to change from ebb to flood dominance.

4.2 INTRODUCTION

New and improved technologies have allowed for the rapid acquisition of large swaths of topographic – bathymetric data to facilitate a range of studies. The variable quality and density of resulting DEMs has led to questions about how DEM differences might affect the representation of flow processes at the ocean bed (Malekia, 2014), as well as in terrestrial channels (McKean et al., 2014). Similar issues have also arisen for estuarine landscapes. For example, Cea and French (2012) investigated the sensitivity of estuarine shallow water flow models to uncertainties in bathymetry and bed friction. They found a strong response in current velocity to bathymetry, while water level fluctuations were influenced more by bed friction. In another study, Camacho et al., (2013) performed uncertainty analysis for 3D hydrodynamic simulations to determine the impact of bathymetric error. They documented strong influence of bathymetry on current velocity and water salinity for locations where DEM depths were shallower than field observations.

These findings contrast with the results of Temmerman et al. (2005). They used a 3D hydrodynamic–sediment transport model on a 0.05km^2 tidal creek catchment to assess the interactions of topography, vegetation, and water level fluctuations on spatial variations in flow and sedimentation. Their flow domain was a lidar DEM reduced to 3m point spacing with a vertical accuracy of 0.13m. Hence, depressions and creek systems that were less than 3m wide were filled in and their effects excluded. Despite this apparent limitation the model validation was successful and the adjusted DEM did not significantly influence simulation results. More recently, Falcao et al., (2013) investigated the influence of grid size and bathymetric interpolation errors in simulating the flooding of intertidal areas. They found that a 5m grid with vertical offsets of up to 0.25m had a very limited impact on the computation of high water levels and aerial extent of inundation, but found discordance in model results for the low spring tide.

In a salt marsh tracer and modeling study Blanton et al. (2010) successfully replicated hydrodynamics of subtidal channels; however, the modeled dye plume distribution and concentrations were less successful. These results led the authors to propose that marsh circulation is highly sensitive to small-scale variations in topography, and in particular to first order intertidal creeks. Recently, the Blanton et al. salt marsh basin was surveyed in high detail using RTK GPS that produced a 1m DEM with 0.02m vertical accuracy. This high resolution DEM was used in simulations of overmarsh flow to highlight complexity in salt marsh circulation (Sullivan et al., 2015) and model results were robust; they accurately replicated observations of dye concentration, pressure, velocity, and local currents. Moreover, the model revealed highly complex flow patterns in space and time that arise from the submergence-emergence of topography.

In this study, we progressively smooth a high precision and high accuracy DEM to gradually reduce topographic detail. The smoothed DEMs were used in hydrodynamic simulations to ascertain the quality of DEM data needed for representative salt marsh flow simulations. Consequently, the progressive smoothing will provide deeper insight into the role of microtopography and intertidal creeks in overmarsh circulation. Here we highlight the effect of smoothing on free surface elevation, velocity and flux, and with dye circulation and residence time.

4.3 STUDY SITE

The study site is a 2km^2 semi-enclosed salt marsh centered at 31.970°, -81.021°, ~20 km south of Savannah, Georgia, USA (Figure 4.1). The local tidal regime is mixed, semi-diurnal, ebb dominant with a mean tidal range of 2.5m and a tidal period of 12.4hrs (NOAA Station TEC3411). The local tidal range varies from 1.54m and 3.20m for neap and spring conditions, respectively (Station 1, Figure 4.2). The basin is bounded by forested land to the west and south where the forest-marsh edge is defined by a 1-3m cliff. Groves Creek is the main channel and it is 3.8km long from the mouth, but at 3.2km it splits into three ~30m wide subtidal branches; the West, Middle and East. The West and East branches surround an area of marsh that is highly dissected by complex networks of intertidal creeks (Figure 4.1). From the mouth of Groves Creek it is 11km to the coastal ocean, along the Wilmington River.

The vegetation is a monoculture of the smooth cordgrass *Spartina alterniflora* (*S. alterniflora*) with spatially variable density and height that depend on surface elevation. In a related study we found that channel banks and levees typically have the tall form of *S. alterniflora* with stem heights that exceed 2m and a density of 112stems/m^2. The short form has an average stem height of 0.28m ±0.25m, a stem density of 446stems/m^2, and it typically occurs on the marsh platform. The intertidal creeks are unvegetated with a relatively smooth mud cover, and with oyster beds at some creek mouths.

During a typical neap high tide the marsh platform and levees remain subaerial, but during spring conditions they are submerged. For this study we conduct simulations corresponding to conditions from October 31st to November 5th, 2010 as the tides transition from neap to spring with tidal ranges going from 2.1m to 3.2m. Hereafter, for brevity we refer to these stages as "neap" and "spring", with peak free surface elevations of 0.78m and 1.45m, respectively. At neap high tide the depth of water over the marsh platform is 0.33m and levees remain subaerial. During the spring high tide the depth of water over the marsh platform is 1.0m and the entire basin is submerged.

4.4 METHODS

4.4.1 MODEL DESCRIPTION AND SETUP

Here we use the validated Delft3D model reported by *Sullivan et al.* (2015). The simulation package consists of integrated modules to compute water currents, water quality, and particle transport. The standard hydrodynamic module is Delft3D FLOW and it accurately simulates flows where horizontal length scales are significantly larger than the vertical (*Lesser et al.*, 2000). It relies on a finite-difference approach to compute water level and depth averaged velocity at each node. The output is subsequently coupled to the PART module to simulate the advection and diffusion of particles. Delft3D PART accounts for the random spreading of particles through the horizontal dispersion coefficient H_D defined by Equation 1 (Csanady, 1973)

$$H_D = at^b \tag{4.1}$$

where t is the length of time that a particle of water stays in the system, and a and b are coefficients that emerge from the model calibration. For these 2D flow simulations a roughness length parameter is specified through model calibration, and this in turn helps determine the logarithmic velocity profile.

Flow is simulated on a grid with uniform 1m horizontal spacing with $5x10^6$ computational nodes. The domain is closed to the west and south along the terrestrial border, and closed to the north along the outer bank of Groves Creek. The domain is open to flow along the eastern boundary defined by the observed water level time series from Station 1. Positive and negative values of flow are in the direction of increasing or decreasing X or Y, respectively. The origin of the computational domain is west of the open flow boundary, and therefore flood velocities are negative and ebb velocities are positive.

The horizontal eddy viscosity is set to $0.0005m^2/s$ (Temmerman, et al., 2005) and bottom roughness is applied as two spatially variable Manning's n values that follow from model calibration. The Manning's n for vegetated and unvegetated marsh are set to 0.10 and 0.017, respectively, comparable to the range of published salt marsh values reported in the literature (see summary in Sullivan et al., 2015). In order to establish experimental control, it is necessary to hold the bottom roughness constant while altering the salt marsh landscape. This means that we assume the area corresponding to channel bed roughness is held constant for each smoothing interval although the channel may experience widening in the smoothing process. This widening however has a negligible effect on simulation results, as explained below.

The modeled dye tracer consists of $7x10^6$ particles, the maximum number required to achieve the highest level of accuracy while maintaining computational efficiency. The accuracy of the tracer simulation is set as the lowest concentration that can be represented by a single particle in a computational cell; in this case it is 4ppb. Horizontal dispersion parameters are set to $a = 0.20m^2/s$ and $b = 0.02$, and a roughness length of 0.001m follow from model calibration. A computational time step of 0.025 minutes is used to establish numerically stable simulations, and results are output at 10 minute intervals.

4.4.2 MARSH STRUCTURE AND DRAINAGE DENSITY

The high resolution DEM is used to generate an elevation contour map to highlight the 2D structure of the marsh landscape, calculate the area of land features, and the help estimate the drainage density, (Dd) of intertidal creeks. Conventionally, Dd of a network is the ratio of total creek length divided by the watershed area. Here, we use the total creek length and total basin area. Creek length is estimated by taking the length of the 0.20m contour that outlines individual creeks. The 0.20m contour was selected because field observations indicate that this elevation represents the "break line" between creek edge and platform. We then halve each creek contour length and define that value as creek length. The basin area is held constant at 1.4km^2, the total area with intertidal creeks.

4.4.3 DEM SMOOTHING

The high resolution DEM is systematically smoothed to remove topographic detail using the "mean focal window" approach in ArcGIS where the mean elevation of an n x n non-overlapping window is computed. Window sizes used are 10x10m, 17x17m, 50x50m, and 100x100m hereafter referred to as *10*, *17*, *50*, *and 100*. The resulting smoothed DEMs are characterized as described above. We then evaluate intertidal flow conditions at three spatial scales 10m, 100m, and 1,000m, and we assess the corresponding dye tracer distributions at-a-station and spatially.

4.4.4 DEM SMOOTHING AND DYE CIRCULATION

We assume the dye is conservative (Blanton et al., 2010) and for each simulation with smoothed topography the dye circulation is compared to the initial or unsmoothed results. To assess the role of topography we first evaluate the dye distribution at two hours before and after high tide using ArcGIS. We then subtract the concentrations of the smoothed DEMs from the initial values (smoothed – initial) at each node and present the result as "difference maps". Further, we quantify changes in tracer residence time at various stations, and for each simulation. Residence time, *Rt* helps characterize topographic control on the time required for a parcel of water to enter and exit the system. Assuming concentration of the tracer decreases exponentially with time (after *Miller and McPherson, 1991*) residence time is computed as:

$$C(t) = C_o e^{-kt} \tag{4.2}$$

$$Rt = \frac{1}{k} \tag{4.3}$$

where at each station $C(t)$ is the concentration at time t, C_o is the initial concentration, and k is a decay constant taken as a first order removal rate. Residence time (Rt) is the inverse of the removal rate.

4.4.5 DEM SMOOTHING AND OVERMARSH CURRENTS

The scales of overmarsh flow analyses are basin (1,000m), macro (100m) and meso (10m). These length scales are not necessarily the lengths of associated measurements but instead they are taken to represent the length scale of underlying flow processes. The basin scale metrics represent spatial patterns of bulk average flows entering and exiting the salt marsh system. The elevation of the free surface during spring tide is mapped over the entire domain at 20 minute intervals during the two hours before and after high tide. Water elevation contour maps are used to compute the free surface slope over a 500m distance between the marsh interior and the Wilmington River (Figure 4.2). The slope is monitored at each smoothing interval, but with particular focus on two hours before and after high tide coinciding with the onset and end of overmarsh flow, respectively.

At the macro scale we investigate changes in the magnitude and direction of velocity vectors averaged over a 60m x 60m grid. This grid size was selected through an iterative grid averaging process for the representation of flows through the marsh interior. Evaluating smoothing effects at this scale is useful in highlighting the topographic controls on circulation complexities at intermediate tidal stages and within the marsh interior. Rose diagrams of initial and smoothed vectors at 2hrs before and after high tide are compared at each smoothing.

The meso scale approach relies on a water balance approach between flood and ebb across six transects (Figure 4.2). Transect 1 encloses the marsh interior but is separated into two parts to account for flows between distinct subtidal systems. Hence, Transect 1a is between the marsh interior and Groves Creek, and 1b is between the marsh interior and the Wilmington River (Figures 4.1 and 4.2). These transects are 500m long and each consists of ten 50m long segments (Figure 4.2) to allow for transect flexibility with respect to topographic structure. Another set of four 50m long transects (2a, 2b, 2c, and 2d) are placed to determine flow characteristics within the marsh interior.

For all transects the magnitude and direction of net flux for the smoothing intervals are computed at ten minute intervals and net fluxes are summed over the full spring tide (780min). The convention for describing flux direction across Transects 1 and 2 is expressed as positive (+) for outflow or ebb, and negative (-) for inflow or flood

(Figure 4.2). Thus, flood and ebb volumes that do not sum to zero indicate a net difference interpreted as a preferential flow direction over the tidal cycle. Specifically, a positive value at Transect 1 indicates net flow away from the marsh interior. Likewise, consistent positive (or negative) values for Transect 2 collectively indicate net rotational flow.

Overall, the different scales of analyses provide detailed insight on how systematic variations in topography affect overmarsh circulation. Also, a net result of smoothing is the gradual removal of the intertidal creek networks for the entire system. Therefore, an ancillary product of this work is an assessment of the role of intertidal creeks on overmarsh circulation. In other words, an added feature of this effort is an evaluation of the role of intertidal creeks in water cycling.

4.5 RESULTS

4.5.1 DEM SMOOTHING

Figure 4.3a shows the structure of the landscape prior to smoothing. The subtidal system has a mean elevation of -2.74m, and a total length of 3,210m. The corresponding subtidal area is 0.16km^2, or about 11% of the basin area (Table 4.1). The main channel narrows from 128m at the mouth to about 30m at the three branches. Each of the branches also becomes narrower in the "upstream" direction, down to less than 1m at the terrestrial edge (Figure 4.3a). The West branch is the longest at 1,360m, followed by the Middle at 717m, and the East at 485m.

There are 88 intertidal creeks with a total area of 0.27km^2 and a mean bed elevation of -0.16m ± 0.26m (Figure 4.3a). The creek lengths and widths vary from 10m – 500m and 1m – 20m, respectively. Many creeks cut through well-defined levees along the main stem of Groves Creek and some incise the marsh platform, extending hundreds of meters (Figure 4.3a). The smaller and shorter creeks typically occur along the first 2,300m of Grove's Creek and are relatively straight with nominal branching. Between the East and Middle branches creeks tend to form closed loops that produce small intertidal islands less than 500m^2. However, between the West and Middle branches most intertidal creeks are sinuous and branching, and have creek heads originating in a single elongate depression. The area between the East and West branches is referred to as the "dissected marsh" (Figure 4.1 and 4.3a). To the east, along the Wilmington River the largest and deepest intertidal creeks occur. In particular, Hannah’s Creek, the site of Station 8 (Figure 4.1 and 4.3a), is 500m long, becoming narrower and shallower in the upstream direction from 14m – 4m, and $^{-}$1.2m - 0.09m, respectively.

Above the intertidal creeks is the low marsh; it has a mean elevation of 0.34m ± 0.07m and an area of 0.18km^2 (Table 4.1). The most contiguous part of the low marsh is an arc-shaped depression that extends between Stations 2 and 7 (Figure 4.3a), paralleling Grove's Creek part way. Another large area of low marsh is at the heads of the intertidal creek networks in the marsh interior between the West and Middle branches, and smaller creek heads throughout. Also, discrete sections of low marsh are commonly associated with creek heads (Figure 4.3a). The position and orientation of some low lying areas facilitate early and far-reaching inundation and late and prolonged drainage as the tide rises and falls, respectively.

The marsh platform is the most extensive feature with a total area of 0.64km^2, or 46% of the domain (Table 4.1) and a mean elevation of 0.60m ± 0.07m (Figure 4.3a). The expanse of platform is cut by low marsh troughs that divide the landscape into smaller, isolated subplatform areas particularly to the north and east of the marsh interior (Figure 4.3a) and is incised by various intertidal creek systems. In particular, there are three locations where the troughs dividing the platform may allow hydraulic short circuiting of the flow system in that they can serve as important conduits for transport during flood and ebb conditions. These troughs are located east of the marsh interior and form a direct link with the larger subtidal system. The first is located approximately 600m north of the southern terrestrial border (Figure 4.3a) and connects the marsh interior to Grove's Creek. Two others are located at the heads of Hannah's Creek and connect the marsh interior to the Wilmington River (Figure 4.3a).

Levees occupy 0.15km^2 or 10% of the total area (Table 1), and they have a mean elevation of 0.85m ± 0.07m (Figure 4.3a). The continuity and shape of levees vary, with the longest and most continuous occurring along the northeast-southwest reach of Grove's Creek. Most levees along the first 2km of channel vary in height and width and are typically cross-cut by intertidal creeks (Figure 4.3a). Smaller, isolated levees tend to form along the banks of the subtidal branches, and along the banks of intertidal creeks (Figure 4.3a).

In summary, the salt marsh landscape is characterized by highly variable microtopography that define subtidal channels, intertidal creek networks, low marsh, marsh platform and levees. The smallest and shortest intertidal creeks typically occur along the first 2,300m of Grove's Creek, while creek networks in the marsh interior and along the eastern marsh edge are larger and longer. In particular, there are three locations where intertidal creek networks and low marsh troughs link the marsh interior to (1) Grove's Creek and (2 and 3) to the Wilmington River. Below, we report how topographic smoothing affects the system overall and in particular the hydraulic connectivity of the marsh with the subtidal areas.

With the *10* smoothing there is no change in subtidal channel area (Table 4.1) or mean elevation and nominal change in the structure of the three branches (Figure 4.3b). The mean elevation of intertidal creeks increases to -0.14m ± 0.25m, and the smallest creeks along the first 2km of Grove's Creek are now classified as low marsh (Figure 4.3b), and this results in an 11% increase in low marsh area (Table 4.1). Moreover, the connection between the marsh interior and Grove's Creek at about 600m north of the southern boundary is lost, and the associated low marsh trough becomes discontinuous (Figure 4.3b). However, the two troughs at the head of Hannah's Creek persist and the connection between the marsh interior and the Wilmington River remains intact (Figure 4.3b). The mean marsh platform elevation decreases to 0.59m ± 0.07m, and its area increases by 2% (Table 4.1). The mean levee elevation also decreases to 0.83m ± 0.07m, and the smallest levees are now classified as marsh platform (Figure 4.3b), resulting in a 20% decrease in levee area (Table 4.1).

With the *17* smoothing the subtidal channel shallows as the mean elevation increases to -2.65m ± (Figure 4.3c). The narrower reaches of the three subtidal branches become intertidal creeks, resulting in a 4% increase in intertidal creek area (Table 4.1). However, the spatial arrangement of intertidal creek elevations reveals that most of the intertidal creek structures are removed from the basin (Figure 4.3c). For instance, the smaller intertidal creeks along the first 2km of Groves Creek, and most of the creek networks in the marsh are replaced by low marsh and marsh platform (Figure 4.3c). The area of low marsh is 28% greater and the two troughs at the heads of Hannah's Creek persist (Figure 4.3c). The mean elevation of the marsh platform is slightly lower at 0.58m ± 0.07m. The mean levee elevation is the same as with the 10 smoothing, but 40% of levees are now classified as marsh platform (Figure 4.3c).

The *50* smoothing increases the mean elevation of the subtidal channel to -2.4m ± 1.25m, and the three subtidal branches become intertidal creeks (Figure 4.3d), resulting in a 6% decrease in subtidal channel area (Table 4.1). The three branches now connect the main stem of Groves Creek to a large intertidal depression in the marsh interior (Figure 4.3d). Together, these changes produce a 26% increase in intertidal creek area, despite the removal of most intertidal creek structures (Figure 4.3d). The low marsh increases by 33% and is mostly associated with the area surrounding the large depression (Figure 4.3d). However, the low marsh trough between the marsh interior and the Wilmington River is now discontinuous, and there are no direct links between the marsh interior and the larger subtidal system (Figure 4.3d). The mean elevation of the marsh platform decreases to 0.57m ±0.07m, and 5% of the platform area is now classified as low marsh. The mean levee elevation is 0.82m ± 0.06m, and 60% have are replaced by marsh platform with four large levees remaining along the main stem of Groves Creek (Figure 4.3d).

The *100* smoothing results in the mean elevation of the subtidal zone as being -1.8m ± 0.80m, and 12% of the subtidal area is now intertidal (Figure 4.3e). The main channel stem extends to the western terrestrial border where it connects to a trough that is linked to a large depression in the marsh interior (Figure 4.3e). Both the trough and the depression fall within the range of intertidal creek elevations, resulting in a 48% increase in intertidal creek area (Table 4.1). However, intertidal creeks have been completely removed and are now classified as low marsh and marsh platform (Figure 4.3e). The marsh platform is lower, with a mean elevation of 0.56m ± 0.06m, and 12% of the area is reclassified as low marsh.

In summary, the *10* and *17* smoothings result in a shallower subtidal environment, removal of most intertidal creek networks, and a discontinuous link between the marsh interior and Grove's Creek. After *50* and *100* the subtidal channel is shorter and feeds a large depression in the marsh interior. Moreover, intertidal creek networks are completely removed and there are no low marsh troughs connecting the marsh interior and the larger subtidal system. Also, 74% of levee area is removed.

4.5.2 DRAINAGE DENSITY

Initially, the total length of intertidal creeks in the 1.4km^2 basin area was 25.8km, giving an average drainage density of 18.5km/km^2 (Table 4.2). For comparison, Marani et al., (2003) evaluated the drainage density of 136 watersheds within 20 salt marshes from the northern lagoon of Venice. They found a fairly constant drainage density of about 20km/km^2. Meanwhile, Novakowski et al., (2004) found a drainage density of 13.8km/km^2 for a salt marsh island located near North Inlet, SC. Hence, the drainage density estimated for Groves Creek is comparable to other salt marshes in various geographic regions.

The *10* smoothing reduces the total creek length to 11.1km, giving a drainage density of 7.9km/km^2 (Table 4.2). The *17* smoothing results in a total creek length of 6.3km, yielding a drainage density of 4.5 km/km^2; a 75% decrease from the initial value. Hence, after *17* most intertidal creek networks are removed. After *50*, the total creek length is 1.6km and the drainage density is reduced further to 1.1km/km^2 (Table 4.2). The final smoothing of *100* results in a total creek length of 0.75km and a drainage density of 0.53 km/km^2; which is 3% of the original value.

In summary, *10* and *17* substantially reduce the total length of intertidal creeks and they reduce the drainage density by 75%. Hence, the majority of intertidal creeks have been removed in the first two smoothings. The *50* and *100* smoothings result in a complete removal of intertidal creeks. An ancillary benefit of conducting simulations on a sequentially smoothed DEM is that we gradually remove the intertidal creek system and consequently the simulation results from those conditions help highlight the role of intertidal creeks in overmarsh circulation.

4.5.3 DEM SMOOTHING AND BASIN SCALE CIRCULATION

At 9:00 46% of the total area is inundated and the water surface elevation is < 0.67m (Figure 4.4a). During this time water is confined to the subtidal system, lower intertidal creek networks, and low marsh. At 9:40, or two hours before high tide, 91% of the marsh is inundated with most levees subaerial (Figure 4.4c). The maximum water surface elevation is 0.87m to the east and 0.75m in the marsh interior. At this time the marsh floods from the east to the southwest as a type of sheetflow rather than from Groves Creek, and persists until high tide.

At 12:40 the water surface is 1.25m in the marsh interior and decreases outward to 1.19m (Figure 4.5a). At 13:40, or two hours after high tide, the elevation decreases from 0.85m in the marsh interior to 0.67m in the subtidal channel and some intertidal creeks (Figure 4.5d). At 14:00 24% of the marsh is subaerial with a water surface of 0.72m across the western low marsh and in the marsh interior (Figure 4.5e), and < 0.67m outward. At this time flow is toward the west and east through intertidal creeks and Groves Creek.

In summary, with inundation the free surface relief is 0.05m – 0.12m, and on ebb it is 0.06m – 0.18m. Patterns of free surface slope dynamics indicate that the directions of inundation vary directly with inundated area. Flooding occurs from the interior by flow through the subtidal to intertidal creeks to the marsh platform, but at 9:40 there is southwesterly overmarsh flow. Likewise, the reverse is apparent during ebb. With the onset of drainage there is radial flow outward from the southwest and it persists for three hours, to Groves Creek and the Wilmington River Later as the marsh topography becomes subaerial flows develop toward the marsh edge, giving rise to flow separation toward the east and west of the marsh interior.

Table 4.3 highlights the free surface slope over the eastern marsh edge during flood and ebb, at two hours before and after high tide, respectively. Initially, the free surface slope on flood is westward at $1.4\text{x}10^{-4}$ (Table 4.3). On ebb the slope is $3.0\text{x}10^{-4}$ toward the east, 53% greater than flood. Here, we take the greater slope and likely stronger flow over the marsh edge during ebb than during flood as an indication of ebb dominance (*Bayliss-Smith et al.*, 1979; *Myrick and Leopold* 1963; *Healey et al.*, 1981).

Each smoothing gives rise to an increase in the free surface slope during flood, indicating more robust flows to the west. Slopes increase from $1.14\text{x}10^{-4}$ initially to $4.0\text{x}10^{-4}$ for the *100* smoothing (Table 4.3). During ebb the eastward sloping free surface responds differently. First, the *10* and 17 smoothings produce a slope that remains unchanged relative to the initial. At *50* and *100* the slope increases slightly, but much less than was detected during flood. Hence, smoothing has a greater effect on flood than on ebb. In particular, with the *50* and *100* the westward flow during flood is likely stronger than during ebb indicating that the higher quality DEM shows ebb dominance while the lower quality DEMs show flood dominance.

Overall, the basin scale analysis shows that the directions of inundation and drainage vary with the area of submerged marsh. In particular, at two hours before and after high tide, water moves as southwesterly and easterly overmarsh flows. Moreover, the high quality DEM produced an eastward free surface slope that is greater than the southwesterly slope during flood, and we take this to represent ebb dominance. Topographic smoothing results in a progressive increase in free surface slope and to a greater extent during flood. In fact, the *50* and *100* smoothings produces a southwesterly flood slope that exceeds the eastward ebb slope. Reducing topographic detail resulted in the overall system switching from ebb to flood dominance.

4.5.4 DEM SMOOTHING AND MACRO SCALE CIRCULATION

The effects of DEM smoothing on macro scale circulation were evaluated by monitoring changes in average velocity vectors in a 60m x 60m window and comparison with the initial unsmoothed results. For brevity, rose plots of velocity magnitude and direction at 2hrs before and after high tide are compared for each smoothing (Figure 4.6). In general, the results at 9:40 for the original DEM show westerly flows that exceed 0.20m/s, and < 0.05m/s flows in all directions (Figure 4.6a). Also, high velocities occur toward the northwest and southwest. Intermediate to these are southwesterly flows that reach up to 0.15m/s.

In all cases flood conditions for the smoothed DEMs have most of the higher velocities and in more directions (Figure 4.6). Also, the occurrence of the higher velocity increases with successive smoothings but westerly flows remain most common. The *10* had negligible effect on current direction, with 30% to the west and 15% southward (Figure 4.6b). Also, the maximum and mean velocity increases slightly to 0.35m/s and 0.06m/s, respectively. The *17* produced similar results but gave rise to northwesterly flow (Figure 4.6c). With *50* the flows toward the northwest are reduced while flow speeds to the west, southwest and east increase (Figure 4.6d). In to *100*, the majority of flood vectors are toward the west, southwest and south (Figure 6e). Flow is also stronger in all directions and the maximum velocity increases to 0.57m/s (Figure 4.6e).

For the ebb conditions the initial and smoothed DEM results consistently demonstrate that flows were predominantly toward the northwest quadrant, with a wide range of current velocities in all directions (Figure 4.6a – 4.6j). However, in most instances the current velocities of the lower quality DEMs are mostly comparable to the initial values (Figure 4.6a – 4.6j). Also, the increase in occurrence of higher velocities with successive smoothings is less pronounced; opposite of flow conditions.

In summary, with *10* and *17* there is a nominal effect on flood and ebb velocities, while *50* and *100* produced stronger corresponding flow toward the southwest and northeast. This effect is more pronounced during flood than during ebb. For example, the peak flood velocity after *100* is 0.54m/s or 32% stronger than the peak ebb velocity of 0.36m/s.

4.5.5 DEM SMOOTHING AND MESO SCALE CIRCULATION

The effect of smoothing on meso scale fluxes was evaluated by monitoring changes in net water volume transport over one spring tidal cycle across a set of transects. We focus on the spring tide response because of the fuller inundation of the landscape.

The results are reported in Table 4 as percentages of the initial simulations, with positive and negative values indicating net outward and inward flow, respectively (Table 4.4 and Figure 4.2).

The net transport over Transect 1a increases by 4% after *10* and 6% after the *17* (Table 4.4). However, for *50* and *100* net flow decreased by 28% and by 35%, respectively. The response was similar for Transect 1b, with an initial increase of 5% after *10* and a decrease of 3% after *17* (Table 4.4) followed by a 16% after *50* and 66% after *100*. Despite these slight to moderate differences, in all cases the net direction of flow was positive and away from the marsh interior (Table 4.4 and Figure 4.2)

The initial net transport at Transects 2a – d is positive (Table 4.4). In this case, the positive values collectively indicate counter-clockwise rotational flow (see *Sullivan et al.*, 2015 and Figure 4.2). With each smoothing the response is highly variable with some overall increasing or decreasing fluxes. In particular, for *10* and *17* the changes are all positive and this indicates that, as with the unsmoothed data, flows are characteristically rotational in the counter clockwise direction. However, for *50* and *100* the net fluxes are negative and this indicates clockwise rotational flow.

Typically, topographic smoothing results in a slight increase in net water flux across Transect 1 with *10* and *17*, and a decrease in flux with *50* and *100* (Table 4.4). However, the net flow direction is consistently outward for all smoothings. The Transect 2 response is more variable. Net flux declines after the first two intervals, but is 5 – 7 times greater with *50* and *100*. These differences indicate counter clockwise rotational flow for *10* and *17*, and clockwise rotation with *50* and *100*.

4.5.6 DEM SMOOTHING AND DYE CIRCULATION OVER THE BASIN

Figure 4.7 shows the dye distribution resulting from the initial DEM. At two hours before high tide the dye remains in the inner marsh with the front forming a half "oval" shape of higher concentrations open to the northwest, centered on Groves Creek (Figure 4.7a). Also, very little dye remains in the main subtidal channel, and most is on the dissected marsh. However, this general view is interrupted by two features; one is a high concentration area in the dissected marsh, and another is a low concentration front along the marsh platform north of and parallel to Groves Creek. Also, pockets of high and low concentration are distributed throughout (Figure 4.7a).

At two hours after high tide the dye is much more dilute; less than half the flood values (Figure 4.7b). Most of the higher concentrations are within ~300m of the southern terrestrial border, and much lower concentrations occur to the north. The resulting dye distribution nearly encircles the inner part of Groves Creek, and the outward non-uniform dye front develops several "points" that indicate focused flow away from the interior (Figure 4.7b). In this case the dye entered the marsh via Grove's Creek but exited through Hannah's Creek. Hence, a short-circuiting of the flow system occurred.

Difference maps between the smoothed and unsmoothed dye concentrations at two hours before high tide are shown in Figure 4.8. The difference values range from -800ppb to +1500ppb, but 99% are within 200ppb of the initial concentrations. Overall, the extent of dye in the initial simulations and that inferred from the difference maps are comparable. Moreover, with each smoothing there are comparable areal extents of surplus and deficit values, but their spatial arrangements are highly variable. Hence, the system has patches of high and low difference throughout.

The series of difference maps show that the extent of surplus values becomes progressively confined closer to the subtidal system, and the patchiness substantially decreases (Figure 4.8). This means that each smoothing gives rise to the presence of more concentrated dye in the subtidal system, and the dye distribution becomes more uniform.

The maximum extent of dye is also noteworthy. For example, the initial results show dye reaching the heads of many adjoining creek systems that are oriented away from the marsh interior. In particular, for the initial, *10* and *17* smoothings highly concentrated dye reaches the "headwater" areas of Hannah's Creek and adjoining systems, whereas the subsequent smoothings lead to lower concentrations reaching the same area (Figure 4.8). Hence, the smoothings of *50* and *100* essentially shut down the delivery of highly concentrated dye to the intertidal creeks that during ebb can be expected to "short-circuit" the flow system and return marsh water directly to the Wilmington River, thus bypassing Groves Creek.

Moreover, during ebb, the range and magnitude of differences are much lower than during flood (Figure 4.9). As with flood conditions, the areal extents of dye in the initial simulation and that inferred from the difference maps are comparable. Patches of high and low differences are distributed throughout, but with dissimilar spatial arrangement. In particular, we focus on the differences determined at the upper reaches of the Hannah's Creek network.

In all cases of topographic smoothing Hannah's Creek serves as a conduit for flow between the marsh interior and the Wilmington River. However, the supply of concentrated water reaching and flowing through the creek system is highly variable. For the *10* and *17* smoothings water in the south fork and that flowing out of the system is progressively more concentrated (Figure 4.9). On the other hand, with the 50 and 100 smoothings the concentrations at the same locations are substantially reduced. Also, for the 100 there is a high concentration patch to the west of the creek system, along the terrestrial border and another noteworthy patch northward, where concentrated water reaches the headwaters of creeks that empty directly into Groves Creek.

In summary, on the flood *10* and *17* resulted in more expansive areas of higher dye concentrations in the marsh interior, along the southern terrestrial border, and near the head of Hannah's Creek. Meanwhile, more dilute dye occurs in the subtidal channel and intertidal networks. With *50* and *100* there is much more dye confined to the subtidal system and lower dye delivery to the surrounding marsh interior. Therefore, the *10* and *17* smoothings produced slightly enhanced dye dispersal relative to *50* and *100*. During ebb, the differences are smaller during flood, but their magnitudes increase with smoothing. At *10* and *17* more concentrated dye exits the basin through Hannah's Creek. At *50* and *100* the dye is confined to the marsh interior, less dye passes through Hannah's Creek, and thus Groves Creek assumes a larger role with respect to dye removal from the marsh. Together, these results reveal that the effects of diminished DEM quality on dye circulation are: 1) limited dye dispersal to the marsh interior during flood, 2) enhanced dye retention during ebb, and 3) differences between flood and ebb flowpaths.

4.5.7 TRACER RESIDENCE TIME

Simulations of residence times (*Rt*) at various locations range from 1.02 day – 1.20 day (Table 4.5). At Stations 1 and 2 the *Rt* values of 1.18 day and 1.20 day, respectively, are longer than other stations because these sites are "upstream" of the release point (Table 4.5). However, these high values are artifacts of the experimental design, e.g. introduction of dye on rising tide causes dye to move away from these stations, toward others. Consequently, excluding these stations gives a maximum of 1.14 day. Station 7 is located in the low marsh and has the lowest *Rt* of 1.02 day. All other stations that, by their location, represent the average marsh interior conditions have a *Rt* of 1.07 day - 1.14 day.

Overall, the smoothings give a consistent *Rt* response. In going from the initial to the *10* and then to the *17* the values systematically decline at all stations (Table 4.5). But from *17* to *50* to *100 Rt* increases. Therefore, the first two smoothings appear to promote dye transfer. On the other hand, for *50* and *100* the dye dispersal is inhibited and retained in the system over a longer time. In addition, the range of *Rt* values between the eight stations increases with smoothing (Table 4.5), indicating that variations in *Rt* are in part related to the topographic expression of the marsh surface.

In summary, the tracer residence time at all stations decreases with *10* and *17*, but increases for *50* and *100*. Hence, the first two smoothings indicate more efficient flushing while the *50* and *100* results indicate greater dye retention. Moreover, the range of *Rt* values increases with each smoothing, and this reveals that *Rt* values can differ considerably as a function of topographic structure. Together, these results show that diminished DEM quality can give rise to substantially different residence times of natural or introduced constituents.

4.6. DISCUSSION

The Groves Creek salt marsh is characteristic of a complex intertidal landscape. In particular, the high resolution DEM shows small intertidal creeks that cross cut levees, and complex creek networks throughout the marsh interior, and in many cases creek systems are connected at their heads by low marsh. Moreover, the detailed DEM reveals three locations where creek networks and low marsh troughs facilitate a direct exchange of water between the marsh interior and Groves Creek and with the Wilmington River. This hydraulic connectivity is important because it gives rise to the potential for "short-circuiting" of the flow system. In other words, Wilmington River water that enters the marsh system through Groves Creek during flood may return to the Wilmington River through these hydraulic connections, and consequently bypass Groves Creek on ebb.

The gradual approach to topographic smoothing progressively reduces the drainage density by approximately 50% with each iteration, and it decreases the number and extent of intertidal creeks. In particular, after the *10* and *17* smoothings the drainage density is significantly reduced and the surface is nearly devoid of intertidal creeks. Moreover, at *50* and *100* the hydraulic connections that are higher in the tidal framework and between the marsh interior and the Wilmington River are broken; hence, connectivity is lost. Together, these structural changes in the marsh landscape allow us to infer from our results the role of intertidal creeks and hydraulic connectivity in simulating overmarsh circulation. Overall, the *10* and *17* smoothings did not noticeably impact overmarsh circulation despite the removal of most intertidal creeks. Further, simulations signifigantly diverge from the initial high quality DEM results once the connectivity is lost with the *50* and *100* smoothing. Hence, the hydraulic connectivity of the basin greatly influences overmarsh circulation much more than the intertidal creek networks.

The loss of connectivity from the *50* and *100* smoothings also produced a system wide switch from ebb to flood dominance. For instance, at the basin scale the initial DEM has a free surface slope over the eastern marsh edge that is greater during ebb than flood, and we take this to represent ebb dominant conditions. At *10* and *17*, the ebb dominant conditions persist, while *50* and *100* produces a westward flood slope that exceeds the slope during ebb, indicating flood dominance (Table 4.3). At the macro scale peak ebb currents at 2hours after high tide are initially greater than peak flood currents, and this is also true after *10* and *17*. However, peak flood velocity exceeds peak ebb flow by 32% with the greater smoothing. Moreover, the meso scale assessment counterclockwise rotational flow for initial, *10* and *17* simulations, while the *50* and *100* smoothings give rise to clockwise rotational flow. Taken together these findings suggest that the flood-ebb dominance of a basin is in part related to geomorphic structure and in particular the hydraulic connectivity of the landscape, or opportunities for short circuiting. This is important because spurious simulation results arising from variable DEM quality will likely impact studies of system morphodynamics. For example, sediment flux is intrinsically related to tidal asymmetry through flood or ebb transport, and the development of flood or ebb dominant bedforms (Aubrey, 1986; Van de Kreeke and Robaczewska, 1993; Freidrichs et al., 1998). Also, flood dominant flows tend to have higher suspended sediment concentration near the creek/marsh boundary, and thereby increase the sediment supply to the marsh; and marsh accretion (Stevenson et al., 1988; Leonard et al., 1995b). Hence, flood dominance at this salt marsh would likely result in higher levels of marsh accretion and increased organic matter preservation (Stevenson *et al.*, 1988).

Much more information on the smoothing effects on overmarsh circulation can be gleaned by assessing dye dispersal. Maps of concentration difference at 2hrs before high tide indicate that interval *10* and *17* slightly enhanced the dye dispersal to the marsh interior during flood, and higher concentrations exiting the system via Hannah's Creek during ebb. However, at *50* and *100* there is much less dispersal during flood, and higher concentrations exiting through Groves Creek rather than Hannah's Creek. Together, these observations suggest that dye distribution, and ultimately the fate of suspended particlate matter is largely influenced by larger scale hydraulic connectivity higher up in the tidal framework, and to a lesser extent the small intertidal creek networks. This finding contradicts Blanton et al., (2010) who speculated that salt marsh circulation is highly sensitive to the effect of smaller "capillary" creeks or intertidal creeks less than about 1m in width and depth. They attributed their limited tracer dispersal during flood and dye retention in the marsh interior during ebb to the exclusion of small scale intertidal creeks from their DEM.

Another main finding of this work is that the residence time of water, and hence nutrients, larvae, and other suspended material vary as a function of the basin geomorphic structure. Initially, the *Rt* of the Groves Creek basin is about 1 day. After *10* and *17*, there is a systematic decrease in *Rt* throughout the basin, while at *50* and *100* the *Rt* increases at all sites and is highly variable. From a geomorphic perspective, these results indicate that the flushing processes of a salt marsh with fewer intertidal creeks and lower drainage density are faster, whereas the flushing efficiency of a basin closed off and disconnected from the larger subtidal system is much lower. Therefore, we propose that the range of *Rt* values for any given salt marsh basin is set by the geomorphic structure of the landscape.

Ultimately, we have shown that the small intertidal creek networks are not necessarily the most important feature for accurate simulation of overmarsh flow. Rather, it is the hydraulic connectivity that facilitates direct links between the marsh interior and the larger subtidal system. Hence, we propose that the DEM quality be sufficient of capturing the hydraulic connectivity across the marsh, but not necessarily the smallest creeks. At this study site a DEM resolution of 17m is sufficient for accurate representation of flows.

4.7 CONCLUSIONS

Here we ask the question: How much DEM detail is need to accurately represent overmarsh circulation in a Georgia, USA salt marsh? Smoothing a highly accurate DEM with a window of 17m x 17m effectively removes small scale intertidal creek systems and the corresponding overmarsh flow simulations are not affected. However, smoothing with a 50m x 50m window reveals a threshold in hydrodynamic response that is coincident with the removal of short-circuiting pathways between the marsh interior and the larger subtidal system. Hence, for accurate simulations of overmarsh circulation the DEM must account for the hydraulic connectivity of the basin, but not necessarily the smaller intertidal creeks and creek networks.

Table 4.1: 2D assessment of geomorphic areas and drainage density (Dd) before and after smoothing. The percent change from the initial value is shown in parenthesis.

	Subtidal (km^2)	Intertidal (km^2)	Low Marsh (km^2)	Marsh Platform (km^2)	Levee (km^2)
Initial	0.16	0.27	0.18	0.64	0.15
10	0.16	0.27	0.20 (11%)	0.65 (2%)	0.12 (20%)
17	0.15 (6%)	0.28 (4%)	0.23 (28%)	0.65 (2%)	0.09 (40%)
50	0.15 (6%)	0.34 (26%)	0.24 (33%)	0.61 (5%)	0.06 (60%)
100	0.14 (12%)	0.40 (48%)	0.26 (44%)	0.56 (12%)	0.04 (73%)

Table 4.2 Creek length and drainage density (Dd) before and after smoothing. The percent change from the initial value is shown in parenthesis.

	Intertidal Creek Length (km)	Dd (km/km^2)
Intertidal	25.8	18.4
10	11.1	7.9 (57%)
17	6.3	4.5 (75%)
50	1.6	1.1 (94%)
100	0.75	0.53 (97%)

Table 4.3 Table 3: Free surface slope over the eastern marsh edge at 940 GMT and 1340 GMT, or two hours before and after high tide.

	940	1340
Initial	$1.4\text{x}10^{-4}$	$3.0\text{x}10^{-4}$
10	$1.8\text{x}10^{-4}$	$3.0\text{x}10^{-4}$
17	$2.2\text{x}10^{-4}$	$3.0\text{x}10^{-4}$
50	$3.4\text{x}10^{-4}$	$3.2\text{x}10^{-4}$
100	$4.0\text{x}10^{-4}$	$3.8\text{x}10^{-4}$

Table 4.4: Net flux over Transects 1a and 1b, and 2a, 2b, 2c, and 2d before and after topographic smoothing. Positive values over 1a and 1b reflect net flow toward the basin exterior, and net counterclockwise rotation over the marsh interior. Negative values reflect the opposite.

	1a	1b	2a	2b	2c	2d
Initial	+1	+1	+1	+1	+1	+1
10	+1.04	+1.05	+0.55	+1.30	+1.10	+0.85
17	+1.06	+1.05	+0.12	+1.10	+0.66	+0.26
50	+0.72	+0.84	-5.61	-1.23	-0.37	-0.02
100	+0.65	+0.34	-6.98	-0.58	-0.96	-0.21

Table 4.5: Tracer residence time (Rt) for Stations 1, 2, 3, 3g, 5g, 6, 7 and 8 before and after topographic smoothing.

	St. 1	St. 2	St. 3	St. 3g	St. 5g	St. 6	St. 7	St. 8
Initial	1.18	1.2	1.07	1.14	1.14	1.08	1.02	1.12
10	1.05	0.98	0.85	1.13	1.13	1.01	0.83	0.91
17	0.99	0.92	0.80	1.11	1.06	0.94	0.83	0.86
50	1.23	1.04	1.10	1.39	1.31	1.43	1.15	1.09
100	1.21	1.79	2.12	3.44	3.23	2.77	1.32	1.32

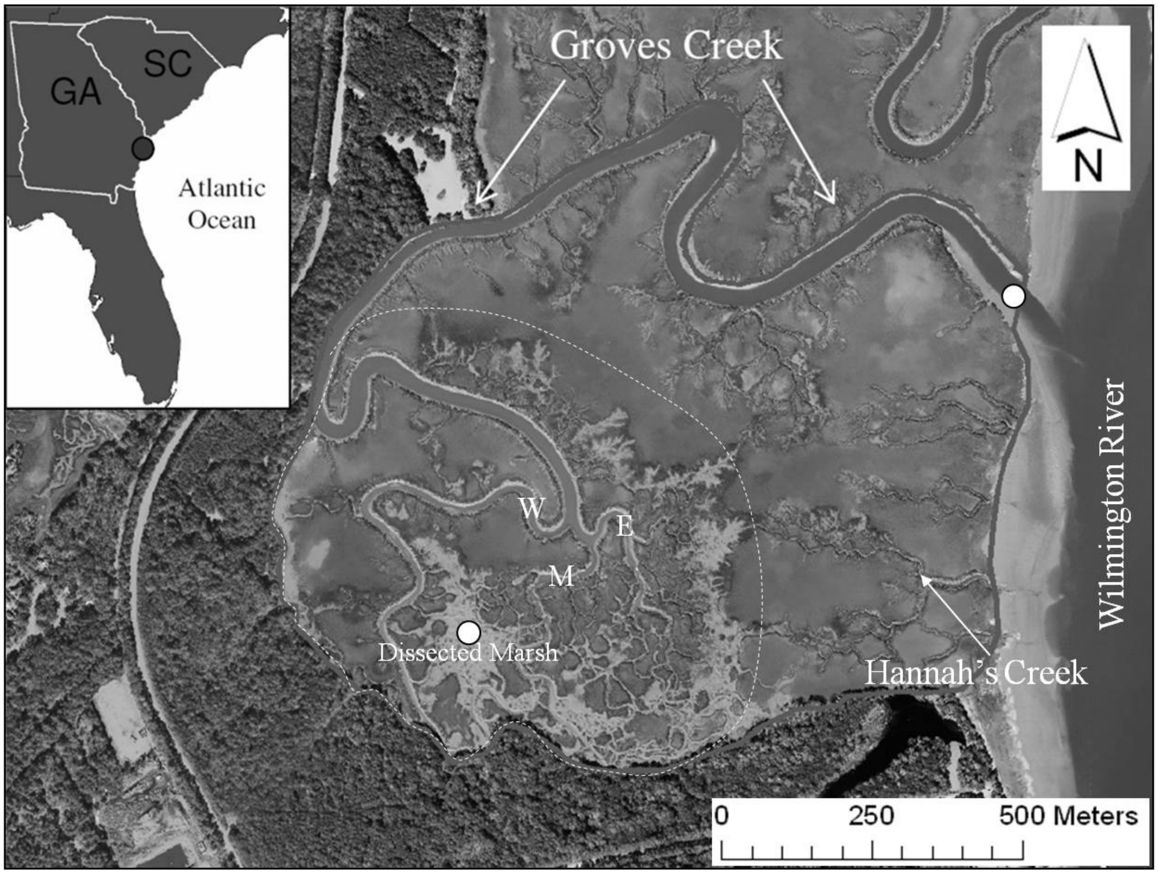

Figure 4.1 Groves Creek is a semi-enclosed creek-marsh system located approximately 20 km south of Savannah GA, USA. The shading of the imagery reflects variations in vegetation density. Specifically, lighter shades in the dissected marsh and along creek heads are associated with unvegetated mud. Darker shades along levees and creek banks reflect areas of dense vegetation. Medium shades are associated with the vegetated marsh platform. The lighter shading of the marsh platform in the northeast is associated with an area of sparsely vegetated high marsh. Groves Creek has three subtidal branches labeled E, W and M for East, West and Middle, respectively. The largest intertidal creek is located along the eastern marsh edge and is referred to as “Hannah’s Creek”. The white dashed line outlines the “marsh interior”. Within the marsh interior is the “dissected marsh” which is bounded by the West and East subtidal branches.

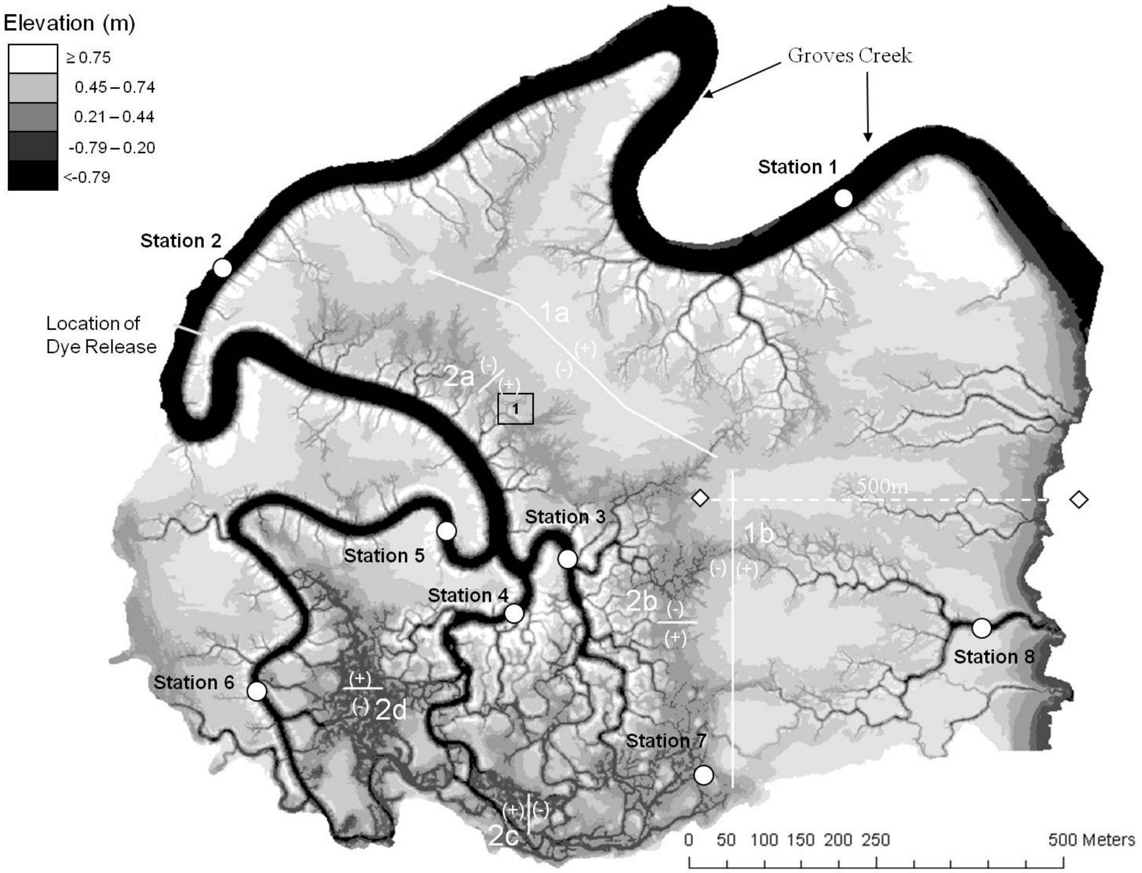

Figure 4.2 The initial high resolution GPS DEM is shown. White to black on the color bar represents the elevation range associated with levee, marsh platform, low marsh, intertidal creeks, and subtidal channel, respectively. White circles mark the locations of pressure sensors, ADCPs, fluorometers, and grab samples. The small gray line south of Station 2 marks the location of the dye release. The white diamonds mark the locations where the free surface slope is monitored for the basin scale assessment. The white lines throughout the marsh interior represent the six transects used to estimate meso scale flux. Transects lengths are 500m for 1a and 1b and 50m for 2a, 2b, 2c, and 2d. The + and - illustrate the flow convention for the meso scale analysis. For transects 1a and 1b, positive flows represent net transport away from the marsh interior. For transects 2a-2d, positive flows represent net counterclockwise flow within the marsh interior. Finally, the black box labeled "1" marks the location of the dogleg creek selected for the micro scale assessment.

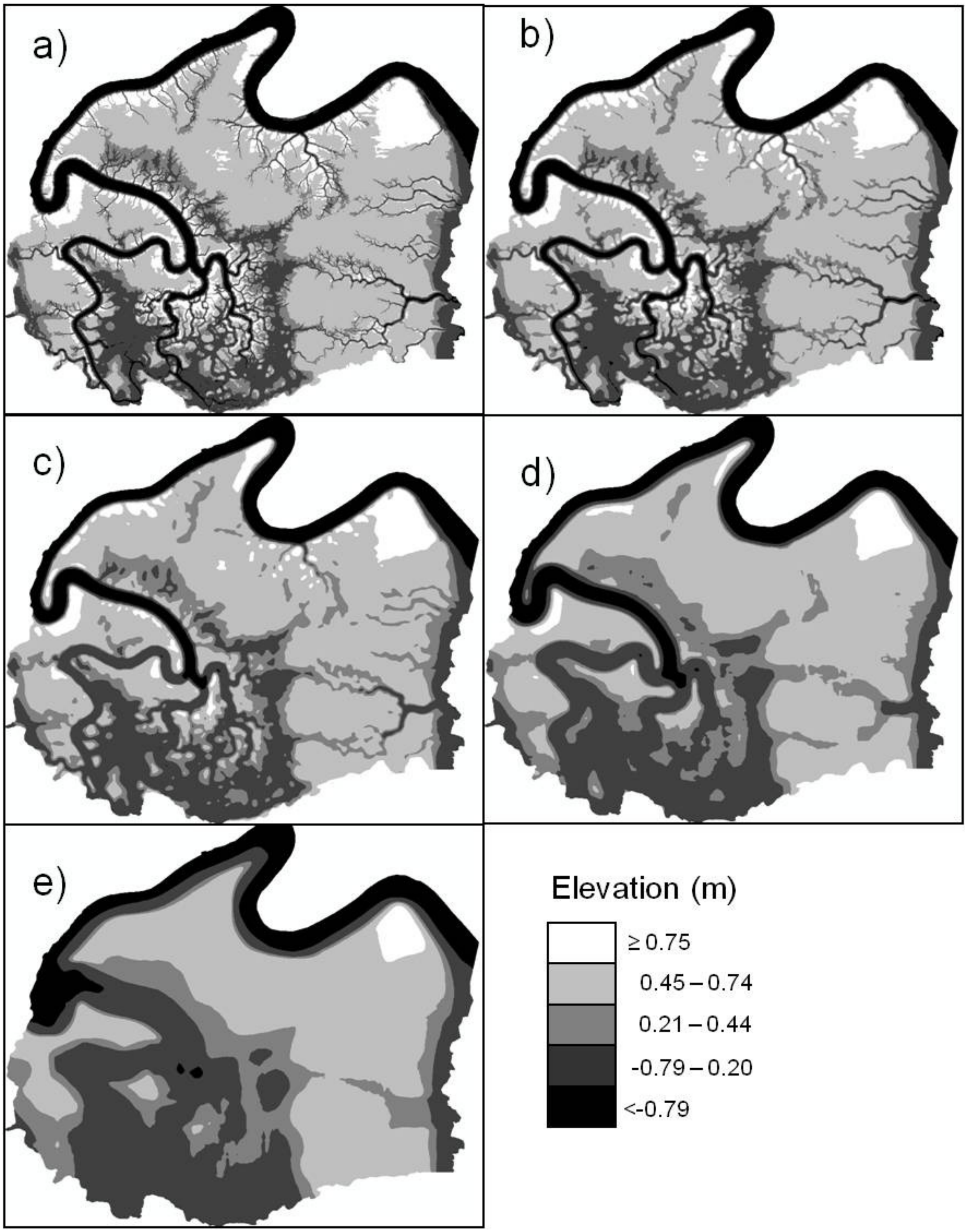

Figure 4.3 The series of maps showing (a) the initial DEM, (b) the 10x10, (c) 17x17, (d), 50x50, and (e) 100x100. The series of maps illustrates the 2D alteration of the landscape. From high to low elevation, the contour intervals reflect the elevation range of the levees (white), marsh platform (light gray), low marsh (light gray), intertidal creeks (medium gray) and subtidal channel (black).

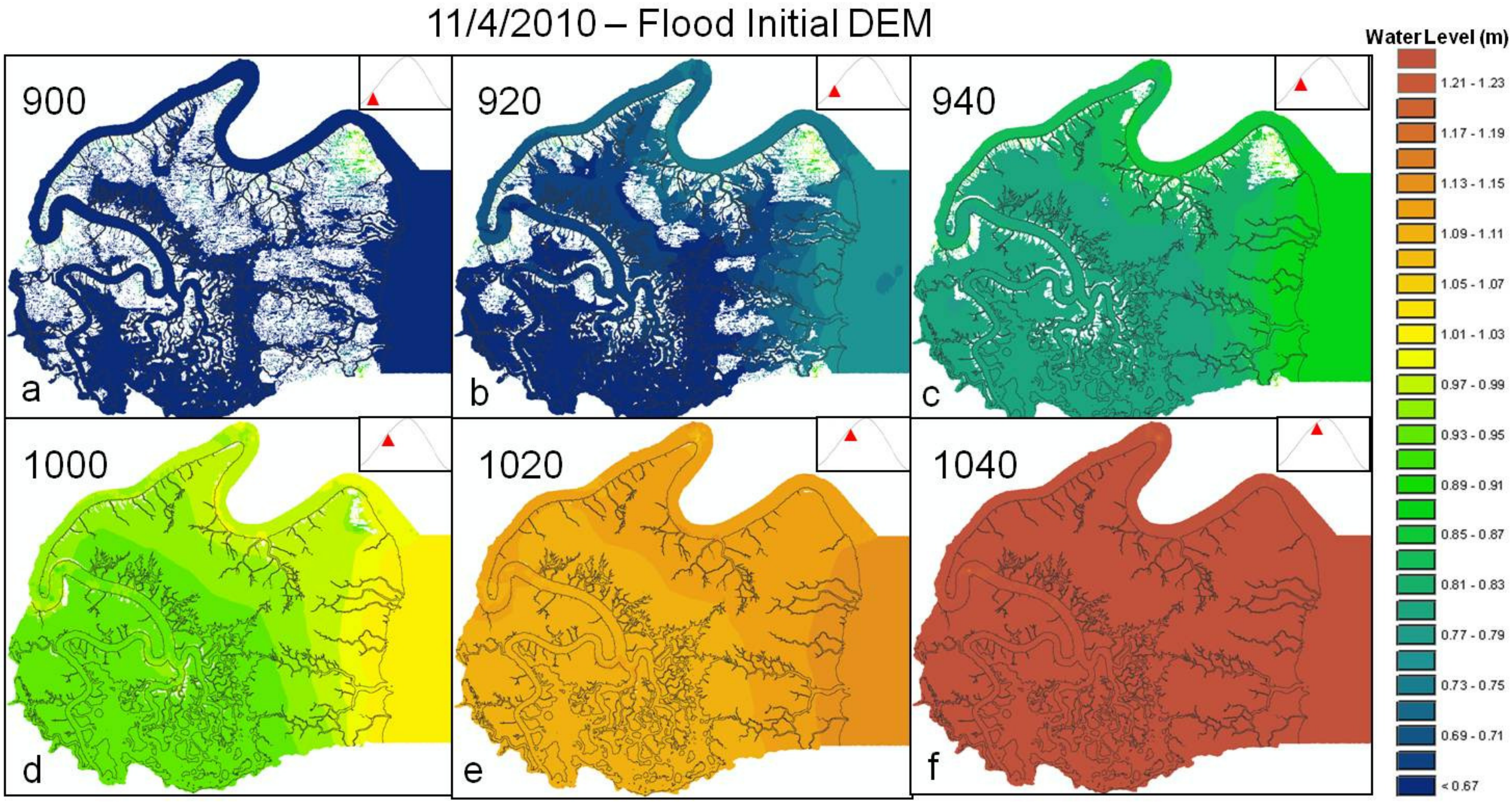

Figure 4.4 A series of maps showing the free surface elevation at 0.33hr intervals during the spring flood tide. This is the free surface prior to DEM smoothing. Warm and cool colors represent high and low water surface elevation, respectively.

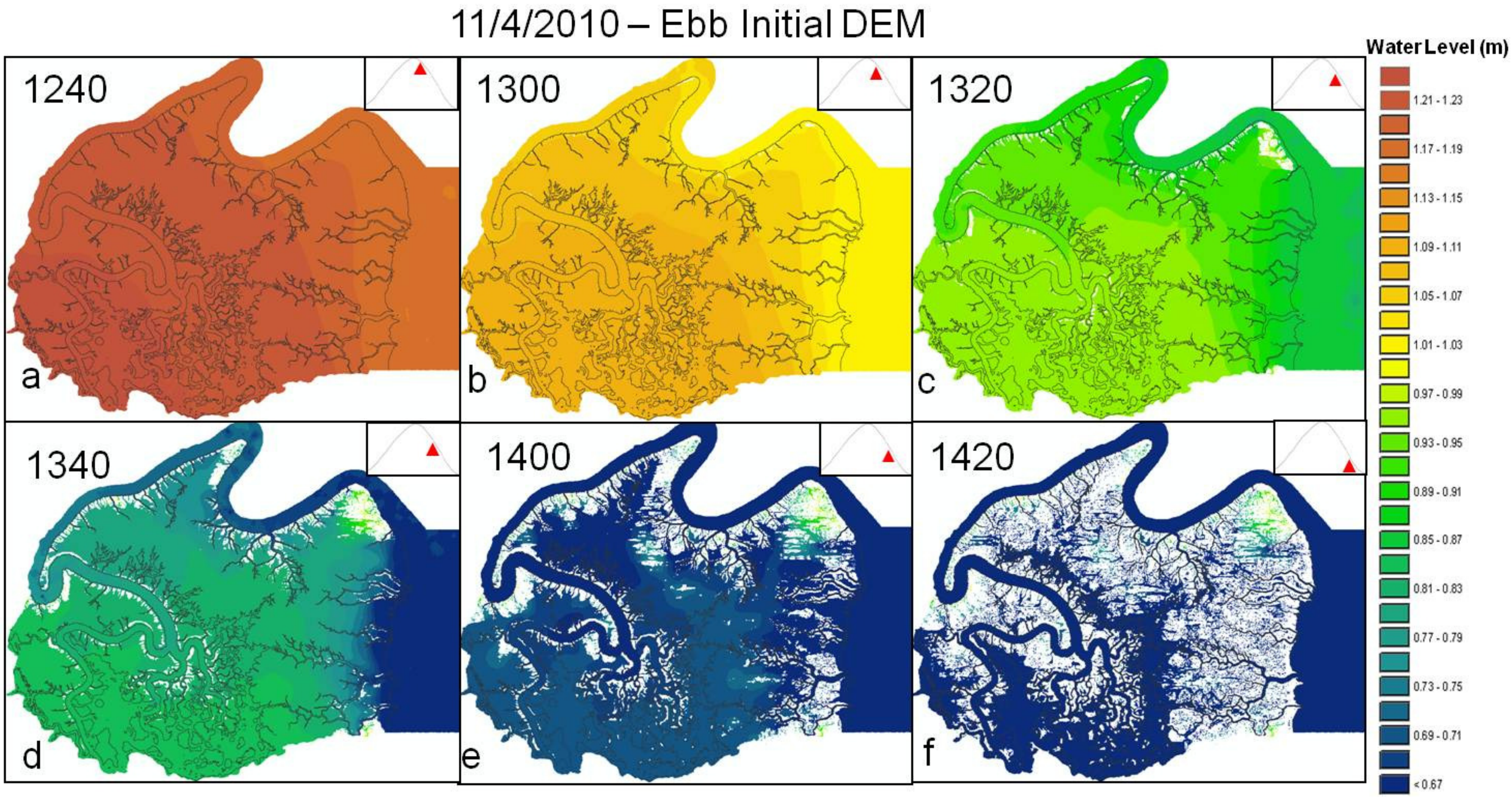

Figure 4.5 A series of maps showing the free surface elevation at 0.33hr intervals during the spring ebb tide. This is the free surface prior to DEM smoothing. Warm and cool colors represent high and low water surface elevation, respectively

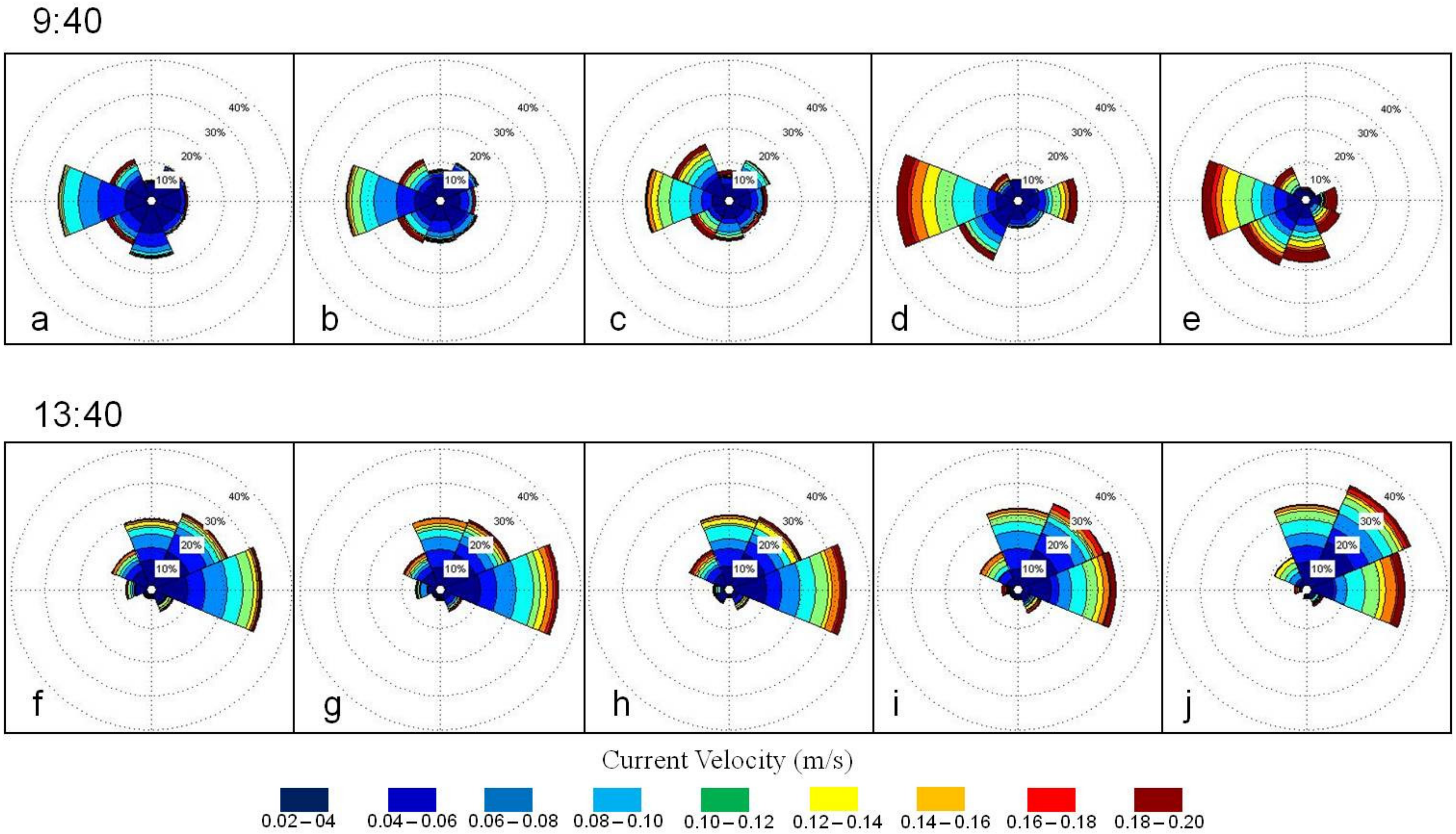

Figure 4.6 Rose diagrams of macro scale velocity before and after smoothing, and at 9:40 and 10:40 GMT. The dashed circles represent the percentage of vector differences for a given direction. The color ramps associated with each bar represent the magnitude of velocity where warm and cool colors represent large and small values, respectively

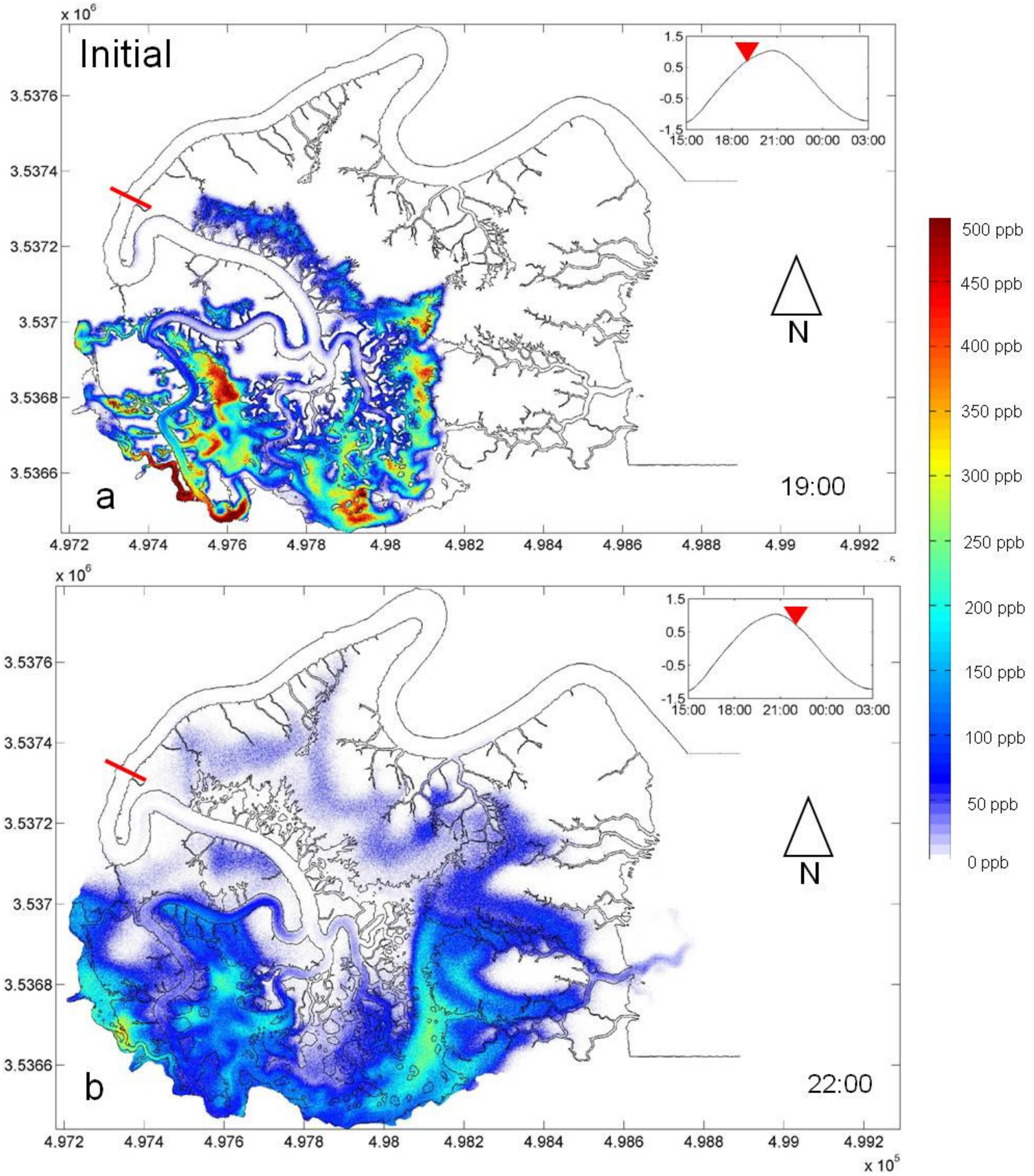

Figure 4.7 Maps of dye transport at (a) 1900 GMT and (b) 2200 GMT, or two hours after high tide on November 1st, 2010. The red line marks the location of the dye release. The subplot shows the tidal stage at each timestep. Warm and cool colors show areas of high and low concentration, respectively.

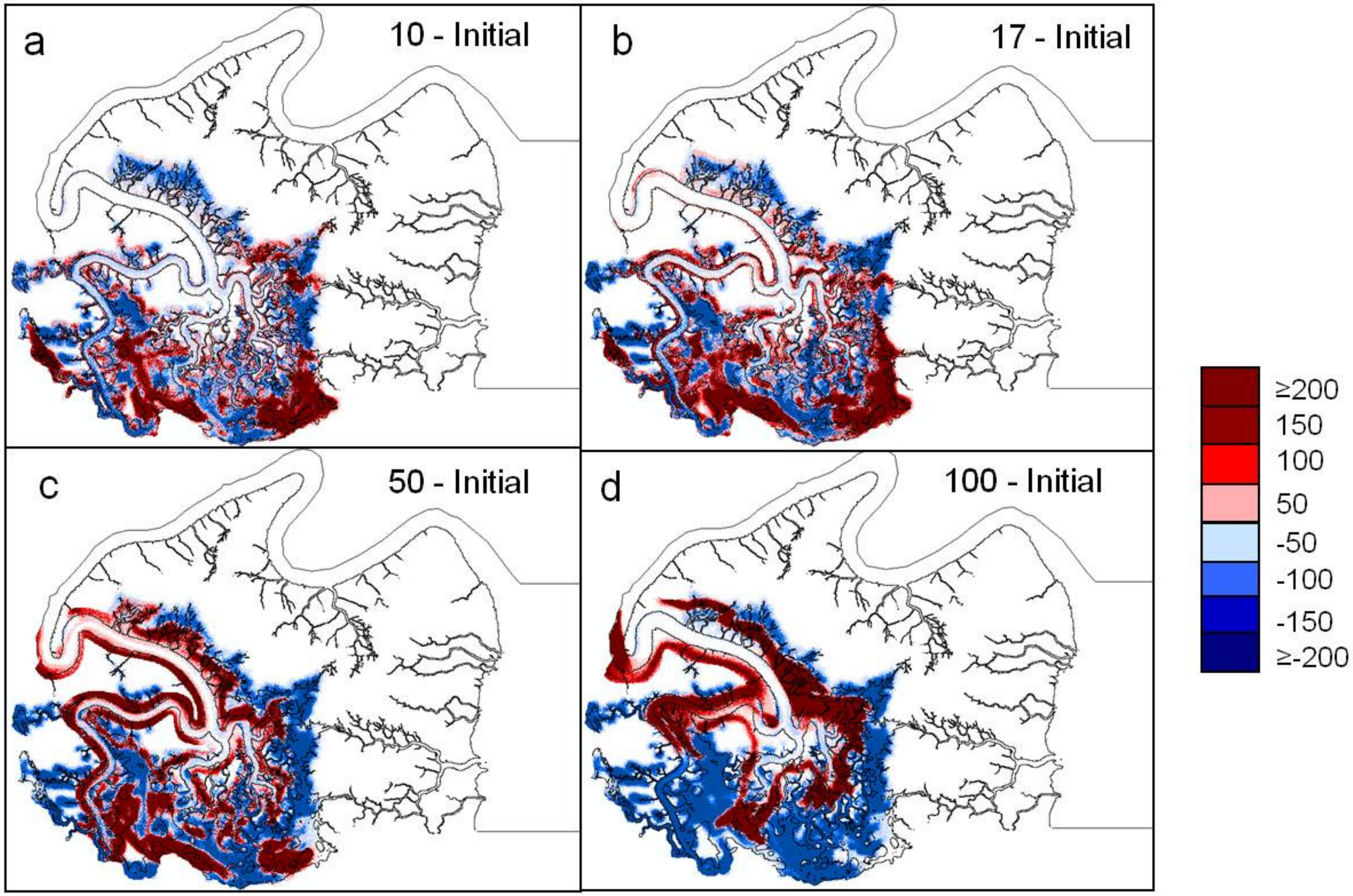

Figure 4.8 Maps of concentration differences at 1900 GMT for (a) 10 - initial, (b) 17 - initial, (c) 50 - initial, and (d) 100 - initial. Red shades represent areas where smoothing resulted in higher concentrations, and blue shades represent areas where smoothing produced lower concentrations.

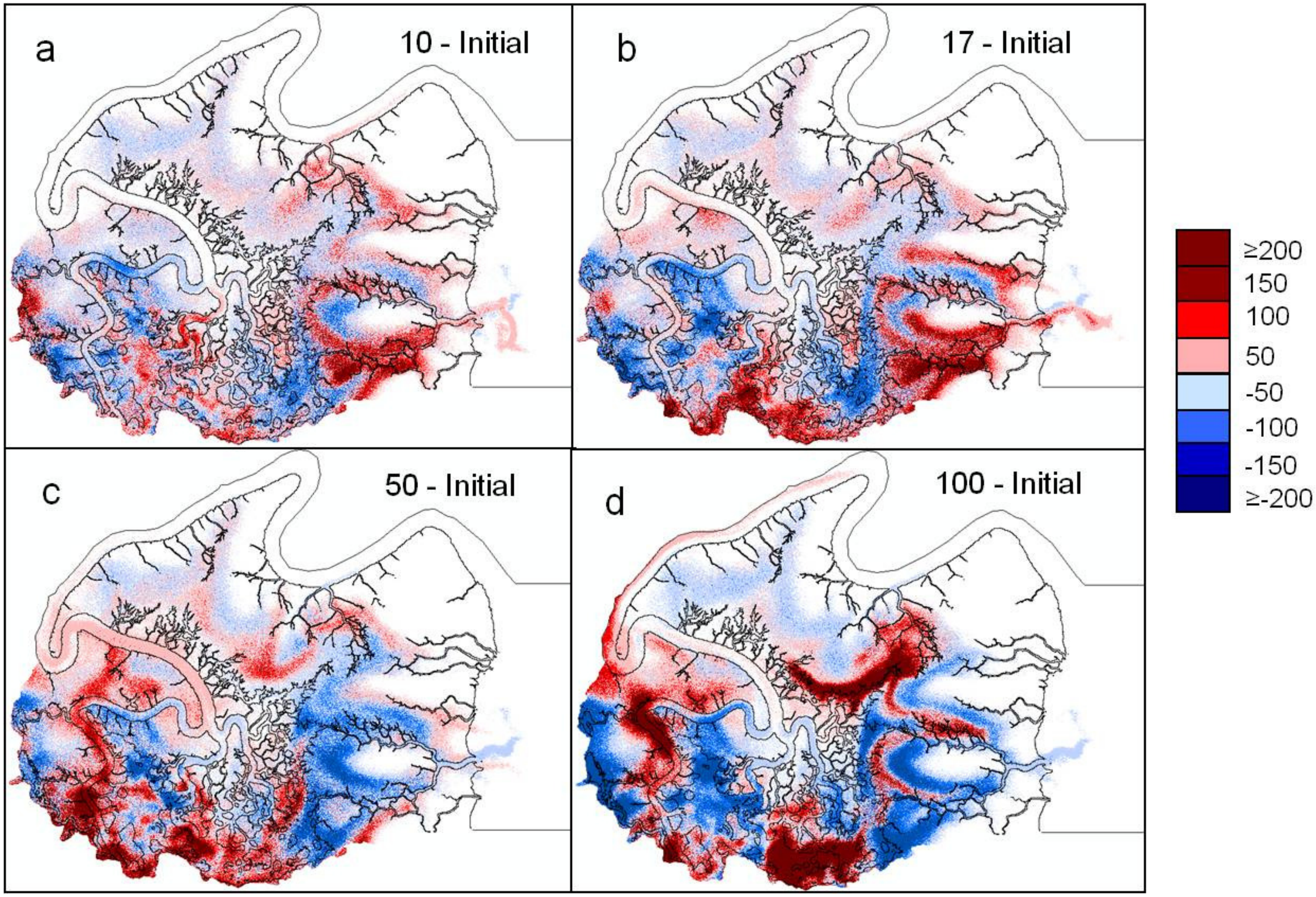

Figure 4.9 Maps of concentration differences at 2200 GMT for (a) 10 - initial, (b) 17 - initial, (c) 50 - initial, and (d) 100 - initial. Red shades represent areas where smoothing resulted in higher concentrations, and blue shades represent areas where smoothing produced lower concentrations.

CHAPTER 5

SUMMARY

This dissertation highlights the complexity in overmarsh circulation across various spatial and temporal scales that arise from the submergence/emergence of subtle salt marsh topography. It also provides a deeper insight into the geomorphic controls on flow processes in intertidal landscapes. In the first part of this work GPS and lidar salt marsh DEMs were compared to evaluate how well the remote sensing technology captures the salt marsh topography. Results show that 78% of the lidar elevations were within the accepted range of accuracy and, therefore, lidar appears to be a robust tool for measuring salt marsh topography. However, the spatial arrangement of elevation differences reveals that the lidar DEM poorly represents the subtle geomorphic structure of the marsh landscape. Therefore, for studies of flow processes in salt marshes lidar surveys should be supplemented with additional elevation data.

In the second part of this work, a high precision, high resolution GPS DEM is used for hydrodynamic simulations of overmarsh flow and dye circulation using Delft3D. The simulation results are robust and in most cases produced a model efficiency greater than 0.90. This is primarily due to the high quality salt marsh DEM and the range and quality of field data for calibration and validation. Dye transport and circulation reveal strong complexity with the temporal evolution of inundation, and drainage at water levels within 0.2m of the mean platform elevation. Moreover, over the full five-day simulation interval we found that 53% of the dye mass exited the system at the eastern marsh edge while 32% exited via the mouth of Groves Creek. At the basin scale (1,000m) the marsh platform is initially inundated from the marsh interior but as the tide continues to rise flooding occurs from the basin edges, and the onset of overmarsh flow. At the macro scale (100m) flow paths are highly variable with concomitant convergence and divergence, and strong flow over the marsh edge. At the meso scale (10m) I detected rotational flow over the marsh interior, and across channel heads. At the micro scale (1m) I show that flood and ebb flow are controlled by the channel banks but at higher tide stages the larger scale barotropic pressure gradient causes the currents to flow across tidal creek networks. Together, these results reveal that overmarsh flow complexities arise from the temporal variations in submergent/emergent topography.

Finally, I progressively smooth the high resolution DEM to investigate the effect of DEM quality on achieving accurate simulations of overmarsh circulation. Topographic smoothing with a window size of 17m x 17m effectively removes small scale intertidal creek systems and the corresponding overmarsh flow simulations are not affected. However, smoothing with a 50m x 50m window reveals a threshold response that is coincident with the removal of short-circuiting pathways between the marsh interior and the larger subtidal system. These findings reveal that small intertidal creeks have a minor role in overmarsh circulation, while the presence of short-circuiting flowpaths dictates circulation for 53% of the water entering the basin. Hence, for accurate simulations of overmarsh flow the DEM must account for the hydraulic connectivity of the basin to the surrounding subtidal system, but not necessarily the smaller intertidal creeks and creek networks. For the Groves Creek salt marsh, a topographic resolution of 17m or less is sufficient.

REFERENCES

Abdelrhman M.A. 2005. Simplified modeling of flushing and residence times in 42 embayments in New England, USA, with special attention to Greenwich Bay, Rhode Island, *Estuarine and Coastal Shelf Science.* 62. 339-351. doi:10.1016/j.ecss.2004.09.021.

Allen J.R.L. 2000. Morphodynamics of holocene salt marshes: a review sketch from the Atlantic and southern North Sea coasts of Europe. *Quarternary Science Review.* 19. 1155-1231.

Aubrey D.G. 1986. Hydrodynamic controls on sediment transport in well-mixed bays and estuaries, *Physics of Shallow Estuaries and Bays*. New York: Springer-Verlag. 245-258.

Baltsavias E.P. 1999. Airborne laser scanning: existing systems and firms and other resources, *ISPRS Journal of Photogrammetry and Remote Sensing* 54: 164-198.

Barwis J.H. (1978), Sedimentology of some South Carolina tidal-creek point bars, and a comparison with their fluvial counterparts, *Fluvial Sedimentology, Miall AD (ed.), Canadian Society of Petroleum Geologists*, 129-160.

Bayless-Smith T.P., R. Healey, R. Lailey, T. Spencer and D.R. Stoddart (1979), Tidal flows in salt-marsh creeks, *Estuarine and Coastal Marine Science*, 9, 235-255.

Bell J. 2009. The 3D structures of a salt marsh island, *M.S. thesis*. Department of Geology. University of South Carolina, USA.

Blanton J.O., A.J. Garrett, J.S. Bollinger, D.W. Hayes, L.D. Koffman, and J. Amft. 2010. Transport and dispersion of a conservative tracer in coastal waters with large intertidal areas. *Estuaries and Coasts* 32: 573-592.

Blanton J.O., A.J. Garrett, J.S. Bollinger, D.W. Hayes, L.D. Koffman, J. Amft, and T. Morre. 2010. Transport and retention of a conservative tracer in an isolated creek-marsh system, *Estuarine and Coastal Shelf Science.* 87. 333-345. doi:10.1016/j.ecss.2010.01.010.

Boon J.D.1975. Tidal discharge asymmetry in a salt marsh drainage system. *Limnology and Oceanography.* 20(1): 71-80. doi:10.4319/lo.1975.20.1.0071.

Boon J.D. and R.J. Byrne. 1981. On basin hypsometry and the morphodynamic response of coastal inlet systems. *Marine Geology*. 40: 27.

Bouma T.J., L.A. van Duren, S. Temmerman, T. Claverie, A. Balanco-Garcia, T. Ysebaert, and P.M.J. Herman. 2007. Spatial flow and sedimentation patterns within patches of epibenthic structures: Combining field, flume and modeling experiments, *Continental Shelf Research*. 27(8): 1020-1045. doi:10.1016/1.csr.2005.12.019.

Cain W.J., L.R. Pomeroy, M.A. Moran, and Y.C. Wang. 1999. Oxygen and carbon dioxide mass balance for the estuarine-intertidal marsh complex of five rivers in the southeastern US. *Limnology and Oceanography*. 44(3): 639-649.

Camacho R.A., J.L. Martin, J.D. Ramirez, W. McAnally, H. Rodriguez, P. Suscy and S. Zhang. 2013. Uncertainty analysis of estuarine hydrodynamic models: an evolution of input data uncertainty in the weeks bay estuary, Alabama, *Applied Ocean Research*, 47, 138-153.

Carter W. R. Shrestha, G. Tuell, D. Bloomquist, and M. Sartori. 2001. Airborne laser swath mapping shines new light on Earth's topography. *EOS, Transactions, American Geophysical Union* 82: 549, 550, 555.

Cea L. and J.R. French.2012. Bathymetric error estimation for the calibration and validation of estuarine hydrodynamic models, *Estuarine and Coastal Shelf Science*. 100:124-132, doi:10.1016/j.ecss.2012.01.004.

Chen S. and R. Torres.2012. Effects of geomorphology on the distribution of metal abundance in salt marsh sediment, *Estuaries and Coasts*. 35:1018-1027. doi:10.1007/s12237-012-9494-y.

Christiansen T., P.L. Wiberg and T.G. Milligan. 2000. Flow and sediment transport on a tidal salt marsh. *Estuarine and Coastal Shelf Sciencer*. 50: 315-331. doi:10.1006/ecss.2000.0548.

Csanady G.T. 1973. Turbulent diffusion in the environment (No. 3), Springer.

Dyer K.R. 1973. Estuaries: a physical introduction. *Wiley Interscience*. New York.

Eiser W.C. and B. Kjerve.1986. Marsh topography and hypsometric characterisics of a South Carolina salt marsh basin, *Estuaries Coasts and Marine Science*. 23: 331-345

Fagherazzi S., G. Mariotti, A.T. Banks, E.J. Morgan and R.W. Fulweiler. 2014. The relationships among hydrodynamics, sediment distribution, and chlorophyll in a mesotidal estuary. *Estuarine and Coastal Shelf Science*. 144(1). 54-64.

Fagherazzi S., M. Hannion, and P. D'Odorico (2008), Geomorphic structure of tidal hydrodynamics in salt marsh creeks, *Water Recourses Research.* 44(2). doi: 10.1029/2007WR006289.

Fagherazzi S., L. Carniello, L. D'Alpaos, and A. Defina. 2006. Critical bifurcation of shallow microtidal landforms in tidal flats and salt marshes, *Proceedings of the National Academy of Sciences of the United States of America* 103: 8337-8341. DOI:10.1073/pnas.0508379103.

Fagherazzi S., E.J. Gabet and D.J. Furbish. 2004. The effect of bidirectional flow on tidal channel planforms. *Earth Surface Processes and Landforms*. 29: 295-309.

Falcao A.P., M. Mazzolari, A.B. Gancalves, M.A.V.C. Araujo and A. Trigo-Teixeira. 2013. Influence of elevation modeling on hydrodynamic simulations of a tidally-dominated estuary. Journal of Hydrology. 497: 152-164.

Freidrichs C.T., B.A. Armbrust and H.E. De Swart. 1998. Hydrodynamics and equilibrium sediment dynamics of shallow, funnel-shaped tidal estuaries. *Physics of Estuaries and Coastal Seas, Rotterndam: Balkema Press, The Netherlands*, 315-545.

French J.R. 2003. Airborne lidar in support of geomorphological and hydraulic modeling, *Earth Surface Processes and Landforms.* 28: 321-335. doi:10.1002/esp.484.

French J.R. and D.R. Stoddart.1992. Hydrodynamics of salt marsh creek systems: implications for marsh morphological development and material exchange, *Earth Surface Processes and Landforms.* 17: 2335-252.

Georgas N. and A. F. Blumberg.2004. The influence of centrifugal and Coriolis forces on the circulation in a curving estuary, *Estuarine and Coastal Modeling, ASCE*, 541-558.

Healey R.G., K. Pye, D.R. Stoddart and T.P Bayliss-Smith. 1981. Velocity variations in salt marsh creeks, Norfolk, England, *Estuarine Coastal and Shelf Science*, 13, 5, 535-545.

Hicks D.M., M.J. Duncan, and J.M. Walsh. 2002. New views of the morphodynamics of large braided rivers from high-resolution topographic surveys and time-lapse video. *International Association of Hydrological Sciences*. 276.

Hodgson M. E. and P. Bresnahan. 2004. Accuracy of airborne lidar-derived elevation: empirical assessment and error budget. *Photogrammetry Engineering and Remote Sensing* 70: 331-339.

James T.D., S.L. Barr, and S.N. Lane. 2006. Automated correction of surface obstruction errors in digital surface models using off-the-shelf image processing. *The Photogrammetric Record* 21: 373-397. DOI: 10.1111/j.1477-9730.2006.00398.x.

Jenson J.R., L. Schmidt, S. Schill, and B. Davis. 1998. An evaluation of lidar and IFSAR-derived digital elevation models in leaf-on conditions with USGS level 1 and 2 DEMs. *Remote Sensing of Environment* 84: 295-308.

Kjerfve, B., L.B. Miranda and E. Wolanski. 1991. Modelling water circulation in an estuary and intertidal salt marsh system, *Netherlands Journal of Sea Research*. 28(3): 141-147.

Kneib R. T. 1984. Patterns of invertebrate distribution and abundance in the intertidal salt marsh: causes and questions. *Estuaries*. *7*(4): 392-412.

Knight J.M., P.E.R. Dale, J. Spencer, and L. Griffin. 2009. Exploring lidar data for mapping the micro-topography and tidal hydro-dynamics of mangrove systems: an example from southeast Queensland, Australia. *Estuarine Coastal and Shelf Science* 85: 593-600. DOI:10.1016/jecss.2009.10.002.

Kostka J.E., B. Gribsholt, E. Petrie, D. Dalton, H. Skelton and E. Kristensen. 2002. The rates and pathways of carbon oxidation in bioturbated saltmarsh sediments. *Limnolology and Oceanography.* 47(1): 230-240

Kraus K., and N. Pfeifer. 1998. Determination of terrain models in wooded areas with airborne laser scanner data. *Journal of Photogrammetry and Remote Sensing*. 53: 193-203.

Lane S.N. 2000. The measurement of river channel morphology using digital photogrammetry. *The Photogrammetric Record* 16: 937-361. DOI: 10.111/0031-86X.00159.

Lawrence D.S.L., J.R.L. Allen and G.M. Havelock. 2004. Salt marsh morphodynamics: an investigation of tidal flows and marsh channel equilibrium. *Journal of Coastal Research.* 20(1): 301-316, doi:10.2112/1551-5036.

Leonard L.A., A.C. Hine, R.P. Stumpf and E.E. Wright. 1995b. Sediment transport processes in a west-central Floridal open marine marsh tidal creek; the role of tides and extra-tropical storms. *Estuarine Coastal and Shelf Science*. 41(2): 225-248.

Leonard L.A. 1997. Controls of sediment transport and deposition in an incised mainland marsh basin, Southeastern North Carolina. *Wetlands*. 17(2): 263-274.

Leonard L.A. and D.J. Reed. 2002. Hydrodynamics and sediment transport through tidal marsh canopies, *Journal of Coastal Research.* 36: 459-469.

Leonard L.A. and M.E. Luther. 1995. Flow hydrodynamics in tidal marsh canopies. *Limnolology and Oceanography.* 40(8): 1474-1484.

Leopold L.B., J.N. Collins and L.M. Collins. 1993. Hydrology of some tidal channels in estuarine marshland near San Francisco. *Catena*, 20(5): 469-493.

Lessa G. and G. Masselink. 1995. Morphodynamic evolution of a macrotidal barrier estuary. *Marine Geolog.* 129(1). 2: 25-46.

Lesser G.R. 2000. Computation of three-dimensional suspended sediment transport within the Delft3D-FLOW module, *M.S. thesis*, UNESCO-IHE Institute for Water Education, Delft, The Netherlands.

Lesser G.R., J.A. Roelvink, J.A.T.M. Van Kester and G.S. Stelling. 2004. Development and validation of a three-dimensional morphological model, *Coastal Engineering.* 51(8): 883-915.

Lipcius R.N., R.D. Seitz, M.S. Seebo and D. Colon-Carrion. 2005. Density, abundance and survival of the blue crab seagrass and unstructured salt marsh nurseries of Chesapeake Bay. *Journal of Experimental Marine Biology and Ecology*. 319(1-2): 69-80.

Loder N.M., J.L. Irish, M.A. Cialone and T.V. Wamsley (2009), Sensitivity of hurricane surge to morphological parameters of coastal wetlands, *Estuarine and Coastal Shelf Science.* 84(4): 625-636.

Lohani B. and D.C. Mason. 2001. Application of airborne scanning laser altimetry to the study of tidal channel geomorphology. *Journal of Photogrammetry and Remote Sensing* 56: 100-120.

Marani M., E. Belluco, A. D'Alpaos, A. Defina, S. Lanzoni and A. Rinaldo. 2003. On the drainage density of tidal networks. *Water Resources Research*. 39. 2.

Maleika W. 2014. The influence of the grid resolution of the accuracy of the digital terrain model used in seabed modeling. *Marine Geophysical Research.* doi:10.1007/s11001-014-9236-6.

Marciano R., Z.B. Wang, A. Hibma and H.J. de Vriend. 2005. Modeling of channel patterns in short tidal basins, *Journal of Geophysical Research.* 110: F01001. doi:10.1029/2003JF0000092.

Mariotti G. and S. Fagherazzi. 2011. Asymmetric fluxes of water and sediments in a mesotidal mudflat channel, *Continental Shelf Research.* 31(1): 23-36.

McKean J., D. Tonia, C. Bohn and C.W. Wright. 2014. Effects of bathymetric lidar errors on flow properties predicted with a multi-dimensional hydraulic model. *Journal of Geophysical Research.* 119: 644-664. doi:10.1002/2013JF002897.

Miller R.L. and B. F. McPherson.1991. Estimating estuarine flushing and residence times in Charlotte Harbor, Florida via salt balance and a box model, *Limnology and Oceanography.* 36(3): 602-612. doi:10.4319/lo.1991.36.3.0602.

Moller I., T. Spencer, J.R. French, D.J. Leggett and M. Dixon. 1999. Wave transformation over salt marshes: a field and numerical modeling study from North Norfolk, England. *Estuarine, Coastal and Shelf Science*. 49(3): 411-426.

Monsen N.E., J.E. Cloern and L.V. Lucas. 2002. A comment on the use of flushing time, residence time, and age as transport time scales, *Limnology and Oceanography.* 47(5): 1545 – 1553.

Montane J M and R. Torres. 2006. Accuracy assessment of lidar saltmarsh topographic data using RTK GPS. *Photogrammetric Engineering and Remote Sensing* 72: 961-967.

Morris J.T. and R. Haskin. 1990. A 5-year record of aerial primary production and stand characteristics of *spartina alterniflora*, *Ecology* 71 : 2209-2217.

Morris J.T., D. Porter, M. Neet, P.A. Nobe, L. Schmidt, L.A. Lapine, and J.R. Jensen. 2005. Integrating lidar elevation data, multi-spectral imagery and neural network modeling for marsh characterization. *International Journal of Remote Sensing* 26: 5221-5234.

Myrick R. M. and L.B. Leopold. 1963. *Hydraulic geometry of a small tidal estuary*, 12-18, Washington, DC: US Government Printing Office.

Nash J. and J.V. Sutcliffe. 1970. River flow forecasting through conceptual models part I—A discussion of principles, *Journal of Hydrology.* 10(3): 282-290.

Nixon S.W. (1980). Between coastal marshes and coastal waters – a review of twenty years of speculation and research on the role of salt marshes in estuarine productivity and water chemistry, *Estuarine and Wetland Processes Marine Science*, 11, 437-525.

Novakowski K.I., R. Torres, L.R. Gardner, and G. Voulgaris. 2004. Geomorphic analysis of tidal creek networks. *Water Resources Research* 40: 1317-1320.

Odum E.P. and A.A. De la Cruz. 1967. Particulate organic detritus in a Georgia salt-marsh ecosystem. In *Estuaries*, edited by G.H. Lauff: Am. Ass. Advmt. Sci.

Pestrong R. 1965. The development of drainage patterns on tidal marshes. *Stanford University publications*. 10(2).

Pethick J.S.1980. Velocity surges and asymmetry in tidal channels, *Estuarine and Coastal Marine Science*. 11(3): 331-345.

Reusser L. and P. Bierman. 2007. Accuracy assessment of LiDAR-derived DEMs of bedrock river channels: Holtwood Gorge, Susquehanna River. *Geophysical Research Letters* 34: L23S06. DOI:10.1029/2007gl031329.

Sheng Y. 2008. Quantifying the size of a lidar footprint: a set of generalized equations. *Geoscience and Remote Sensing Letters* 5: 419-422. DOI:10.1109/lgrs.2008.916978.

Shih S.F. and G.S. Rahi. 1982. Seasonal variations of Manning's roughness coefficient in a subtropical marsh, *Transactions of the American Society of Agricultural Engineering*. 25(1). 116-119.

Sithole G and G. Vosselman. 2004. Experimental comparison of filter algorithms for bare-Earth extraction from airborne laser scanning point clouds. *Journal of Photogrammetry and Remote Sensing* 59: 85-101.

Stevenson J.C., L.G. Ward and M.S. Kearney. 1988. Sediment transport and trapping in marsh systems: implications of tidal flux studies. *Marine Geology*. 80(1). 2: 37-59.

Sullivan J.C., R. Torres, A. Garrett, J. Blanton, C. Alexander, M. Robinson, T. Moore, J. Amft and D. Hayes. 2014. Complexity in Salt Marsh Circulation for a Semi-enclosed Basin, *Journal of Geophysical Research – Earth Surface, submitted.*

Tamura Y., M. Matsui, and L. Carlotta. 2002. Measurement of wind-induced response of buildings using RTK-GPS, *Journal of Wind Engineering and Industrial Aerodynamics* 90: 1783-1793.

Teal J.M. 1962. Energy flow in the salt marsh ecosystem of Georgia. *Ecology*. 43(4): 614-624.

Temmerman S., T.J. Bouma, G. Govers, Z.B. Wang, M.B. de Vries and P.M.J Herman. 2005. Impact of vegetation on flow routing and sedimentation patterns: three dimensional modelling for a tidal marsh. *Journal of Geophysical Research.* 110.

Temmerman S., G. Govers, P. Meire, and S. Wartel. 2005. Modelling long-term tidal marsh growth under changing tidal conditions and suspended sediment concentrations, Scheldt estuary, Belgium, *Marine Geology* 193: 151–169.

Torres R. and R. Styles. 2007. Effects of topographic structure on salt marsh currents, *Journal of Geophysical Research.* 112. F02023. doi:10.1029/2006JF000508.

Tsihrintzis V. and E.E. Madiedo. 2000. Hydraulic resistance determination in marsh wetlands, *Water Resources Research.* 14(4): 285-309.

Valiela I., J.M., Teal, S. Volkmann, D. Shafer and E.J. Carpenter (1978), Nutrient and particulate fluxes in a salt marsh ecosystem: tidal. *Limnology and Oceanography.* 23(4): 798-812.

Van de Kreeke J. and K. Robaczewska. 1993. Tide-induced residual transport of coarse sediment: application to the Ems estuary. *Netherlands Journal of Sea Research*, 31)3): 209-220.

Vosselman G. 2000. Slope based filtering of laser altimetry data. *International Archives of the Photogrammetry Remote Sensing and Spatial Information Sciences* 33: 935-942.

Wang C., M. Menenti, M.P. Stoll, A. Feola, E. Belluco, and M. Marani. 2009. Separation of ground and low vegetation signatures in lidar measurements of salt-marsh environments, *Transactions on Geoscience and Remote Sensing* 47: 2014-2023. DOI:10.1109/tgrs.2008.2010490.

Warner J.C., D.H. Schoellhamer, J.R. Barau and S.G. Scholadow. 2006. Flow convergence caused by a salinity minimum in a tidal channel, *San Francisco Estuary Watershed Science.* 4(3), 91-102.

Weinstein M.P. 1979. Shallow marsh habitats as primary nurseries for fishes and shellfish, Cape Fear River, North Carolina. *Fish Bull*. 77:339-357.

Wenner E.L. and H.R. Beatty. 1993. Utilization of shallow estuarine habitats in South Carolina, USA, by postlarval and juvenile stages of Penaeus spp. (Decapoda: Penaeidae). *Journal of Crustacean Biology*. 13:280-295.

Williams R.B. and M.B. Murdock. 1966. Annual production of Spartina alterniflora and Juncus roemerianus in salt marshes near Beaufort, North Carolina. *Assoc. Southeastern Biologist Bull*. 49(13).

Wilson C.A.M.E. and M.S. Horritt. 2002. Measuring the flow resistance of submerged grass, *Hydrologica. Processes.* 16(13): 2589-2598.

Yang X. 2005. Remote sensing and GIS applications for estuarine ecosystem analysis: and overview, *International Journal of Remote Sensing* 26 : 5347-5356.

Appendix A – Grab Sample Concentration Timeseries

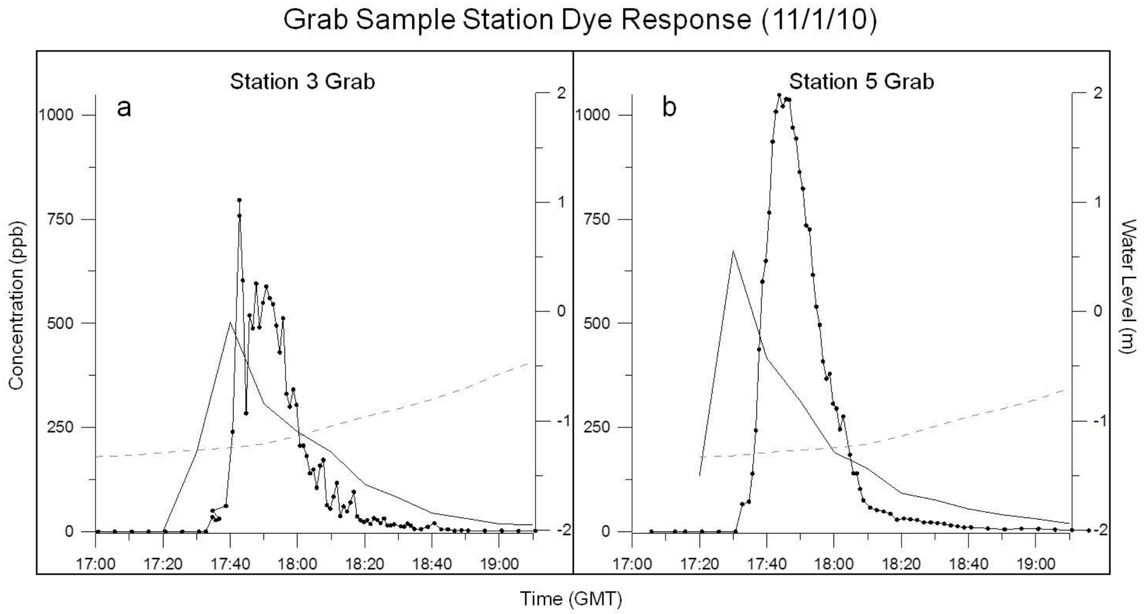

APPENDIX B – COPYRIGHT PERMISSION

JOHN WILEY AND SONS LICENSE TERMS AND CONDITIONS

Feb 24, 2015

This Agreement between Jessica C Sullivan ("You") and John Wiley and Sons ("John Wiley and Sons") consists of your order details and the terms and conditions provided by John Wiley and Sons and Copyright Clearance Center.

License Number	3512550504713
License date	Nov 19, 2014
Licensed Content Publisher	John Wiley and Sons
Licensed Content Publication	Earth Surface Processes and Landforms
Licensed Content Title	A comparison of GPS and lidar salt marsh DEMs
Licensed Content Author	Jessica E. Chassereau,Joseph M. Bell,Raymond Torres
Licensed Content Date	Aug 7, 2011
Pages	6
Type of use	Dissertation/Thesis
Requestor type	Author of this Wiley article
Format	Electronic
Portion	Full article
Will you be translating?	No
Title of your thesis / dissertation	The Effects of Microtopography on Overmarsh Circulation
Expected completion date	May 2015
Expected size (number of pages)	200
Billing Type	Invoice
Billing Address	None 183 Jamestowne Court None None LEXINGTON, SC 29072 United States Attn: None
Total	**0.00 USD**

Total

Terms and Conditions

TERMS AND CONDITIONS

This copyrighted material is owned by or exclusively licensed to John Wiley & Sons, Inc. or one of its group companies (each a"Wiley Company") or handled on behalf of a society with which a Wiley Company has exclusive publishing rights in relation to a particular work (collectively "WILEY"). By clicking �accept� in connection with completing this licensing transaction, you agree that the following terms and conditions apply to this transaction (along with the billing and payment terms and conditions established by the Copyright Clearance Center Inc., ("CCC's Billing and Payment terms and conditions"), at the time that you opened your Rightslink account (these are available at any time at http://myaccount.copyright.com).

Terms and Conditions

- The materials you have requested permission to reproduce or reuse (the "Wiley Materials") are protected by copyright.
- You are hereby granted a personal, non-exclusive, non-sub licensable (on a stand-alone basis), non-transferable,

worldwide, limited license to reproduce the Wiley Materials for the purpose specified in the licensing process. This license is for a one-time use only and limited to any maximum distribution number specified in the license. The first instance of republication or reuse granted by this licence must be completed within two years of the date of the grant of this licence (although copies prepared before the end date may be distributed thereafter). The Wiley Materials shall not be used in any other manner or for any other purpose, beyond what is granted in the license. Permission is granted subject to an appropriate acknowledgement given to the author, title of the material/book/journal and the publisher. You shall also duplicate the copyright notice that appears in the Wiley publication in your use of the Wiley Material. Permission is also granted on the understanding that nowhere in the text is a previously published source acknowledged for all or part of this Wiley Material. Any third party content is expressly excluded from this permission.

- With respect to the Wiley Materials, all rights are reserved. Except as expressly granted by the terms of the license, no part of the Wiley Materials may be copied, modified, adapted (except for minor reformatting required by the new Publication), translated, reproduced, transferred or distributed, in any form or by any means, and no derivative works may be made based on the Wiley Materials without the prior permission of the respective copyright owner. You may not alter, remove or suppress in any manner any copyright, trademark or other notices displayed by the Wiley Materials. You may not license, rent, sell, loan, lease, pledge, offer as security, transfer or assign the Wiley Materials on a stand-alone basis, or any of the rights granted to you hereunder to any other person.

- The Wiley Materials and all of the intellectual property rights therein shall at all times remain the exclusive property of John Wiley & Sons Inc, the Wiley Companies, or their respective licensors, and your interest therein is only that of having possession of and the right to reproduce the Wiley Materials pursuant to Section 2 herein during the continuance of this Agreement. You agree that you own no right, title or interest in or to the Wiley Materials or any of the intellectual property rights therein. You shall have no rights hereunder other than the license as provided for above in Section 2. No right, license or interest to any trademark, trade name, service mark or other branding ("Marks") of WILEY or its licensors is granted hereunder, and you agree that you shall not assert any such right, license or interest with respect thereto.

- NEITHER WILEY NOR ITS LICENSORS MAKES ANY WARRANTY OR REPRESENTATION OF ANY KIND TO YOU OR ANY THIRD PARTY, EXPRESS, IMPLIED OR STATUTORY, WITH RESPECT TO THE MATERIALS OR THE ACCURACY OF ANY INFORMATION CONTAINED IN THE MATERIALS, INCLUDING, WITHOUT LIMITATION, ANY IMPLIED WARRANTY OF MERCHANTABILITY, ACCURACY, SATISFACTORY QUALITY, FITNESS FOR A PARTICULAR PURPOSE, USABILITY, INTEGRATION OR NON-INFRINGEMENT AND ALL SUCH WARRANTIES ARE HEREBY EXCLUDED BY WILEY AND ITS LICENSORS AND WAIVED BY YOU

- WILEY shall have the right to terminate this Agreement immediately upon breach of this Agreement by you.
- You shall indemnify, defend and hold harmless WILEY, its Licensors and their respective directors, officers, agents and employees, from and against any actual or threatened claims, demands, causes of action or proceedings arising from any breach of this Agreement by you.

- IN NO EVENT SHALL WILEY OR ITS LICENSORS BE LIABLE TO YOU OR ANY OTHER PARTY OR ANY OTHER PERSON OR ENTITY FOR ANY SPECIAL, CONSEQUENTIAL, INCIDENTAL, INDIRECT, EXEMPLARY OR PUNITIVE DAMAGES, HOWEVER CAUSED, ARISING OUT OF OR IN CONNECTION WITH THE DOWNLOADING, PROVISIONING, VIEWING OR USE OF THE MATERIALS REGARDLESS OF THE FORM OF ACTION, WHETHER FOR BREACH OF CONTRACT, BREACH OF WARRANTY, TORT, NEGLIGENCE, INFRINGEMENT OR OTHERWISE (INCLUDING, WITHOUT LIMITATION, DAMAGES BASED ON LOSS OF PROFITS, DATA, FILES, USE, BUSINESS OPPORTUNITY OR CLAIMS OF THIRD PARTIES), AND WHETHER OR NOT THE PARTY HAS BEEN ADVISED OF THE POSSIBILITY OF SUCH DAMAGES. THIS LIMITATION SHALL APPLY NOTWITHSTANDING ANY FAILURE OF ESSENTIAL PURPOSE OF ANY LIMITED REMEDY PROVIDED HEREIN.

- Should any provision of this Agreement be held by a court of competent jurisdiction to be illegal, invalid, or unenforceable, that provision shall be deemed amended to achieve as nearly as possible the same economic effect as the original provision, and the legality, validity and enforceability of the remaining provisions of this Agreement shall not be affected or impaired thereby.

- The failure of either party to enforce any term or condition of this Agreement shall not constitute a waiver of either party's right to enforce each and every term and condition of this Agreement. No breach under this agreement shall be deemed waived or excused by either party unless such waiver or consent is in writing signed by the party granting such waiver or consent. The waiver by or consent of a party to a breach of any provision of this Agreement shall not operate or be construed as a waiver of or consent to any other or subsequent breach by such other party.

- This Agreement may not be assigned (including by operation of law or otherwise) by you without WILEY's prior written consent.
- Any fee required for this permission shall be non-refundable after thirty (30) days from receipt by the CCC.
- These terms and conditions together with CCC�s Billing and Payment terms and conditions (which are incorporated herein) form the entire agreement between you and WILEY concerning this licensing transaction and (in the absence of fraud) supersedes all prior agreements and representations of the parties, oral or written. This Agreement may not be amended except in writing signed by both parties. This Agreement shall be binding upon and inure to the benefit of the parties' successors, legal representatives, and authorized assigns.
- In the event of any conflict between your obligations established by these terms and conditions and those established by CCC�s Billing and Payment terms and conditions, these terms and conditions shall prevail.
- WILEY expressly reserves all rights not specifically granted in the combination of (i) the license details provided by you and accepted in the course of this licensing transaction, (ii) these terms and conditions and (iii) CCC�s Billing and Payment terms and conditions.
- This Agreement will be void if the Type of Use, Format, Circulation, or Requestor Type was misrepresented during the licensing process.
- This Agreement shall be governed by and construed in accordance with the laws of the State of New York, USA, without regards to such state�s conflict of law rules. Any legal action, suit or proceeding arising out of or relating to these Terms and Conditions or the breach thereof shall be instituted in a court of competent jurisdiction in New York County in the State of New York in the United States of America and each party hereby consents and submits to the personal jurisdiction of such court, waives any objection to venue in such court and consents to service of process by registered or certified mail, return receipt requested, at the last known address of such party.

WILEY OPEN ACCESS TERMS AND CONDITIONS

Wiley Publishes Open Access Articles in fully Open Access Journals and in Subscription journals offering Online Open. Although most of the fully Open Access journals publish open access articles under the terms of the Creative Commons Attribution (CC BY) License only, the subscription journals and a few of the Open Access Journals offer a choice of Creative Commons Licenses:: Creative Commons Attribution (CC-BY) license Creative Commons Attribution Non-Commercial (CC-BY-NC) license and Creative Commons Attribution Non-Commercial-NoDerivs (CC-BY-NC-ND) License. The license type is clearly identified on the article.

Copyright in any research article in a journal published as Open Access under a Creative Commons License is retained by the author(s). Authors grant Wiley a license to publish the article and identify itself as the original publisher. Authors also grant any third party the right to use the article freely as long as its integrity is maintained and its original authors, citation details and publisher are identified as follows: [Title of Article/Author/Journal Title and Volume/Issue. Copyright (c) [year] [copyright owner as specified in the Journal]. Links to the final article on Wiley�s website are encouraged where applicable.

The Creative Commons Attribution License

The Creative Commons Attribution License (CC-BY) allows users to copy, distribute and transmit an article, adapt the article and make commercial use of the article. The CC-BY license permits commercial and non-commercial re-use of an open access article, as long as the author is properly attributed.

The Creative Commons Attribution License does not affect the moral rights of authors, including without limitation the right not to have their work subjected to derogatory treatment. It also does not affect any other rights held by authors or third parties in the article, including without limitation the rights of privacy and publicity. Use of the article must not assert or imply, whether implicitly or explicitly, any connection with, endorsement or sponsorship of such use by the author, publisher or any other party associated with the article.

For any reuse or distribution, users must include the copyright notice and make clear to others that the article is made available under a Creative Commons Attribution license, linking to the relevant Creative Commons web page.

To the fullest extent permitted by applicable law, the article is made available as is and without representation or warranties of any kind whether express, implied, statutory or otherwise and including, without limitation, warranties of title, merchantability, fitness for a particular purpose, non-infringement, absence of defects, accuracy, or the presence or absence of errors.

Creative Commons Attribution Non-Commercial License

The Creative Commons Attribution Non-Commercial (CC-BY-NC) License permits use, distribution and reproduction in any medium, provided the original work is properly cited and is not used for commercial purposes.(see below)

Creative Commons Attribution-Non-Commercial-NoDerivs License

The Creative Commons Attribution Non-Commercial-NoDerivs License (CC-BY-NC-ND) permits use, distribution and reproduction in any medium, provided the original work is properly cited, is not used for commercial purposes and no modifications or adaptations are made. (see below)

Use by non-commercial users

For non-commercial and non-promotional purposes, individual users may access, download, copy, display and redistribute to colleagues Wiley Open Access articles, as well as adapt, translate, text- and data-mine the content subject to the following conditions:

- The authors' moral rights are not compromised. These rights include the right of "paternity" (also known as "attribution" - the right for the author to be identified as such) and "integrity" (the right for the author not to have the work altered in such a way that the author's reputation or integrity may be impugned).
- Where content in the article is identified as belonging to a third party, it is the obligation of the user to ensure that any reuse complies with the copyright policies of the owner of that content.
- If article content is copied, downloaded or otherwise reused for non-commercial research and education purposes, a link to the appropriate bibliographic citation (authors, journal, article title, volume, issue, page numbers, DOI and the link to the definitive published version on **Wiley Online Library**) should be maintained. Copyright notices and disclaimers must not be deleted.
- Any translations, for which a prior translation agreement with Wiley has not been agreed, must prominently display the statement: "This is an unofficial translation of an article that appeared in a Wiley publication. The publisher has not endorsed this translation."

Use by commercial "for-profit" organisations

Use of Wiley Open Access articles for commercial, promotional, or marketing purposes requires further explicit permission from Wiley and will be subject to a fee. Commercial purposes include:

- Copying or downloading of articles, or linking to such articles for further redistribution, sale or licensing;
- Copying, downloading or posting by a site or service that incorporates advertising with such content;
- The inclusion or incorporation of article content in other works or services (other than normal quotations with an appropriate citation) that is then available for sale or licensing, for a fee (for example, a compilation produced for marketing purposes, inclusion in a sales pack)
- Use of article content (other than normal quotations with appropriate citation) by for-profit organisations for promotional purposes
- Linking to article content in e-mails redistributed for promotional, marketing or educational purposes;
- Use for the purposes of monetary reward by means of sale, resale, licence, loan, transfer or other form of commercial exploitation such as marketing products
- Print reprints of Wiley Open Access articles can be purchased from: corporatesales@wiley.com

Further details can be found on Wiley Online Library http://olabout.wiley.com/WileyCDA/Section/id-410895.html

Other Terms and Conditions:

v1.9

Questions? customercare@copyright.com or +1-855-239-3415 (toll free in the US) or +1-978-646-2777.

Gratis licenses (referencing $0 in the Total field) are free. Please retain this printable license for your reference. No payment is required.